

Dissertation

submitted to the
Combined Faculties for the Natural Sciences and for Mathematics
of the Ruperto-Carola University of Heidelberg, Germany

for the degree of
Doctor of Natural Sciences

Put forward by
M.Sc. Angelika Klein
born in St. Wendel

Oral examination: June 05, 2019

**The fetch dependency of small-scale air-sea interaction
processes at low to moderate wind speeds**

Referees:

Prof. Dr. Bernd Jähne
Prof. Dr. Norbert Frank

Abstract

The water sided mass boundary layer at the air-sea interface is a sublayer of the viscous boundary layer and acts as the bottle neck for air-sea gas transport. The dominant transport mechanism of the mass boundary layer is molecular diffusion. For low to moderate wind speeds, the main mechanisms occurring in the mass boundary layer are the upwelling of horseshoe vortices, the development of along wind streaks, and the so called microscale breaking, a breaking of the wave crests without bubble entrainment.

This thesis investigates the development of these mechanisms in dependence of fetch and wind speed at the Aeolotron wind wave facility, Heidelberg. The collocated and synchronized visualization techniques boundary layer imaging, active thermography, and wave slope imaging enable a unique set of data by providing insight into the turbulent processes taking place in the mass boundary layer and their interaction with wind waves.

Three different fetch dependent regimes could be identified that each contribute differently to air-sea heat exchange: a laminar regime with no wind waves, an overshoot regime for dominant gravity wavelengths smaller than 13 cm, and a declining regime for larger wavelengths. Additionally, a further step has been taken in understanding the cause of the microscale breaking mechanism. The initial disturbance is an accumulation of the mass boundary layer thickness in the trough of the parasitic capillary waves with its spontaneous release initiating the microscale breaking.

Zusammenfassung

Die wasserseitige Massengrenzschicht an der Phasengrenze zwischen Luft und Wasser ist ein Teil der viskosen Grenzschicht und agiert als Flaschenhals für den Transport von Gasen. Der vorherrschende Transportmechanismus in der Massengrenzschicht ist molekulare Diffusion. Für geringe bis mittlere Windgeschwindigkeiten sind die Hauptmechanismen in dieser Grenzschicht hufeisenförmige Wirbel, die Ausbildung von parallel zum Wind verlaufenden Streifen, und mikroskaliges Wellenbrechen, also ein Wellenbrechen ohne Blaseneinschlag.

Diese Arbeit untersucht die Entwicklung dieser Mechanismen in Abhängigkeit von Windwirklänge und Windgeschwindigkeit am Aeolotron Wind-Wellenkanal in Heidelberg. Die Kombination der Visualisierungstechniken Boundary Layer Imaging, aktive Thermographie, und Wave Slope Imaging ermöglichen so ein einzigartiges Set an Daten um die turbulenten Prozesse in der Massengrenzschicht und ihre Interaktion mit Wellen zu untersuchen.

Es konnten drei verschiedene Regime identifiziert werden, die jeweils unterschiedlich zum Wärmeaustausch zwischen Luft und Wasser beitragen: ein laminares Regime ohne Wellen, ein Überschussregime für Wellenlängen der dominanten Schwerewellen kleiner als 13 cm, und ein abnehmendes Regime für Wellenlängen größer als 13 cm. Zusätzlich konnte ein Fortschritt im Verständnis der Ursache von mikroskaligem Wellenbrechen erzielt werden, das begleitet wird von einem Anstauen der Massengrenzschichtdicke in den Wellentälern der parasitären Kapillarwellen, die sich spontan lösen kann.

Contents

| | | |
|----------|---|-----------|
| 1 | Introduction | 1 |
| 2 | Theory | 5 |
| 2.1 | Gas transfer across the air-water interface | 5 |
| 2.1.1 | Transport equations | 5 |
| 2.1.2 | Transport across the interface | 7 |
| 2.1.3 | Schmidt number | 9 |
| 2.2 | Wind Waves | 10 |
| 2.2.1 | Dispersion relation | 10 |
| 2.2.2 | Friction velocity | 11 |
| 2.2.3 | Non-Dimensional Parameters | 12 |
| 2.2.4 | Stokes waves | 13 |
| 2.2.5 | Crapper waves | 13 |
| 2.2.6 | Parasitic capillary waves | 14 |
| 2.2.7 | Wave height | 15 |
| 2.2.8 | Wave breaking | 15 |
| 2.2.9 | Wave growth | 16 |
| 2.3 | Mechanisms in the mass boundary layer | 16 |
| 2.3.1 | Microscale wave breaking | 16 |
| 2.3.2 | Boundary layer streaks | 18 |
| 2.3.3 | Horseshoe vortices | 19 |
| 3 | Measurement techniques, facility, and measurement campaign | 21 |
| 3.1 | The Aeolotron | 21 |
| 3.2 | Imaging slope gauge (ISG) | 21 |
| 3.2.1 | Preprocessing | 24 |
| 3.3 | Boundary layer imaging (BLI) | 24 |
| 3.3.1 | Preprocessing | 25 |
| 3.4 | Active Thermography (AT) | 27 |
| 3.5 | Fetch experiment (FE) | 28 |
| 3.5.1 | Data merging | 30 |
| 3.6 | Overview of the measurement conditions | 31 |
| 4 | Evaluation Methods | 35 |
| 4.1 | Wave properties | 35 |
| 4.1.1 | Significant wave height | 35 |

| | | |
|----------|--|-----------|
| 4.1.2 | Wave phase velocity | 36 |
| 4.1.3 | Wave period and wavelength | 38 |
| 4.1.4 | Parasitic capillary waves | 39 |
| 4.2 | Microscale wave breaking | 39 |
| 4.2.1 | Detection threshold of microscale breaking | 41 |
| 4.2.2 | Wave phase dependent MB | 41 |
| 4.3 | Heat transfer velocity | 43 |
| 4.4 | Boundary Layer Imaging | 43 |
| 5 | Results | 45 |
| 5.1 | Regimes | 45 |
| 5.2 | Heat and gas transfer | 48 |
| 5.2.1 | Heat transfer velocities | 48 |
| 5.2.2 | Gas transfer, Schmidt number exponent, and scaling factor β | 48 |
| 5.3 | Waves | 50 |
| 5.3.1 | Significant wave height and steepness | 50 |
| 5.3.2 | Wave period and phase speed | 52 |
| 5.3.3 | Mean square slope | 53 |
| 5.3.4 | Friction velocity | 57 |
| 5.3.5 | Dimensionless transfer velocity utilizing the friction velocity | 58 |
| 5.3.6 | Reynolds number | 59 |
| | Parasitic capillaries | 62 |
| 5.4 | Microscale wave breaking | 64 |
| 5.4.1 | Dynamics of an MB event | 64 |
| 5.4.2 | Wind and fetch dependent occurrence of microscale breaking | 68 |
| 5.4.3 | Wave phase dependent occurrence of Microscale Breaking | 68 |
| 5.4.4 | Microscale wave breaking in dependence of the wave steepness | 70 |
| 5.4.5 | Microscale breaking and the surf similarity parameter | 70 |
| 5.4.6 | Microscale breaking and heat transfer velocity | 72 |
| 5.4.7 | Occurrence of MB events over time | 74 |
| 5.5 | Streak structures in the boundary layer | 74 |
| 5.5.1 | Regime A: Laminar and fish scale regime - streaks | 77 |
| 5.5.2 | Regime B: Finite fetch with increasing microscale breaking - streaks | 77 |
| 5.5.3 | Regime C: Finite fetch with declining microscale breaking - streaks | 77 |
| 5.5.4 | Regime 1: Infinite fetch with sporadic microscale breaking - streaks | 85 |
| 5.5.5 | Regime 2: Infinite fetch with broad and many microscale breaking - streaks | 85 |
| 6 | Conclusions and Outlook | 89 |

| | |
|---|-----------|
| A Results as tables | 93 |
| B Additional image material | 99 |
| B.1 Visualization | 99 |
| B.1.1 ISG visualization | 99 |
| B.1.2 BLI visualization | 99 |
| B.1.3 AT visualization | 102 |
| B.2 Development of MB along the fetch | 102 |

List of Abbreviations

| | |
|------------|------------------------------------|
| FE | Fetch Experiment |
| BLI | Boundary Layer Imaging |
| ISG | Imaging Slope Gauge |
| MB | Microscale Breaking |
| MBS | Microscale Breaking Seeding |
| AT | Active Thermography |

Chapter 1

Introduction

About two thirds of Earth's surface is covered with water. The exchange of heat, momentum, and gas between the atmosphere and the ocean influences the dynamics and the evolution of Earth's climate. The ocean acts as a major sink for anthropogenic carbon dioxide and other greenhouse gas emissions (Sabine, 2004). The rate of exchange of these quantities is influenced by a multitude of factors such as wind, rain, temperature, and surfactants which themselves may trigger and influence secondary mechanisms like streak formation in the boundary layers and microscale breaking.

The gas exchange between air and water is often parameterized as a function of the wind speed u , the Schmidt number Sc and the Schmidt number exponent n ($k(u, Sc, n)$) (e.g., Bender et al., 2011, Wanninkhof and Triñanes, 2017). Typical mean wind speeds on the ocean in ten meters height are on the order of 7.3 m s^{-1} (Hoffman et al., 2013). For these wind speeds, the most occurring mechanisms in the water sided mass boundary layer, a thin interfacial layer dominated by molecular diffusion, are boundary layer streak formation and microscale wave breaking (MB) (Tsai and Hung, 2007). Of these two mechanisms, MB is thought to be the main driving mechanism of local heat and gas transfer rates (Siddiqui et al., 2004; Siddiqui and Loewen, 2007; Jessup et al., 1997).

Mechanisms in the boundary layer

A common technique to observe the mass boundary layer structures at the water surface is thermography (Jessup et al., 1997), an imaging technique that captures the temperature distribution at the water surface utilizing an infrared camera. Passive thermography detects the cooling of the surface due to evaporative cooling, while active thermography heats the surface by using e.g. an infrared laser and then captures the surface temperatures.

The streaks in the boundary layer (see figure 1.1) are commonly thought to be caused by Langmuir circulation (Tsai et al., 2005). Langmuir circulation has first been observed as a streaky alignment of sea foam, surfactant films, and algae. The

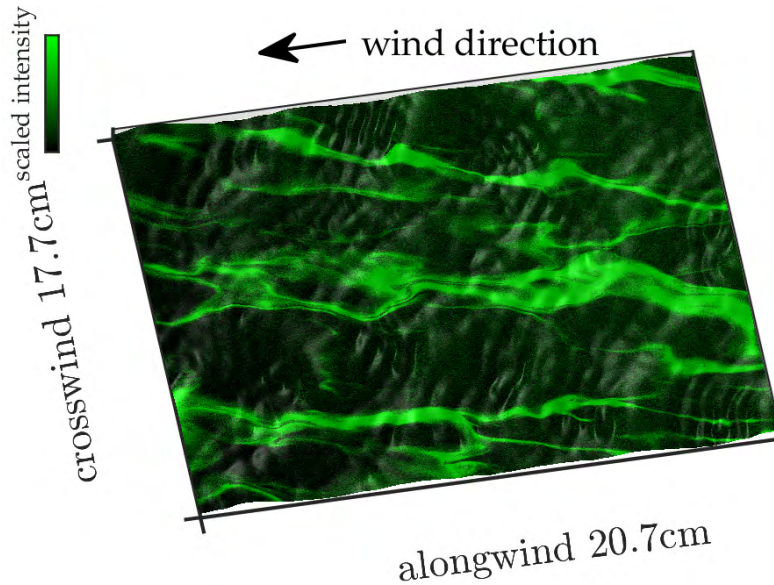


FIGURE 1.1: Streaks, often referred to as micro Langmuir circulation, in the mass boundary layer of a wind driven wavy water surface. The image shows the fluorescence intensity of the streaks, captured using the BLI measurement technique.

streaks usually have a spacing on the order of meters. The streaks in the mass boundary layer of laboratory studies often exhibit a much smaller spacing on the order of centimeters (Schnieders et al., 2013). Besides active thermography, also a recently developed technique, the so called boundary layer imaging (BLI) (Kräuter et al., 2014; Kräuter, 2015), will be used in the scope of this work to analyze the streaky structures in the water sided mass boundary layer.

Microscale wave breaking (see figure 1.2) is a type of wave breaking without bubble entrapment (Banner and Phillips, 1974). It causes a local renewal of the water surface with the bulk water and it is believed to be the main driving mechanism to enhance the air-water gas and heat transfer for low to moderate wind speeds (e.g. Zappa et al., 2004, Zappa et al., 2001). It can be detected by a rough structure of the slopes of the water surface in the wake of the waves as seen by an imaging slope gauge (ISG). It can also be seen in the turbulence of boundary layer particle image velocimetry (PIV) (e.g. Siddiqui et al., 2004, Peirson and Banner, 2003) or in the sudden change of surface temperature in the thermography images. However, the thermography images are only able to observe the close surface with a penetration depth of about $70\ \mu\text{m}$ (Kunz, 2017). The available PIV techniques can only capture the turbulence of the water sided viscous boundary layer, which is approximately a hundred times larger than the mass boundary layer (Siddiqui et al., 2001). In this thesis, besides ISG and thermography, a recently developed measurement technique, the so called boundary layer imaging (BLI) (Kräuter et al., 2014) will be used to investigate the structures and cause of microscale breaking.

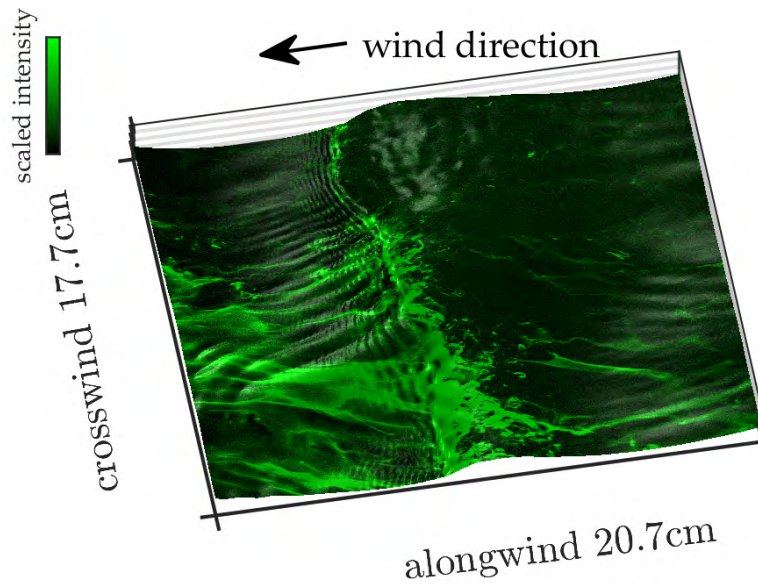


FIGURE 1.2: Microscale wave breaking causes a surface renewal in its wake, thus enhancing local gas and heat transfer velocities. The intensities are the fluorescence signal of the BLI measurement technique.

Thesis outline

In chapter 2 the underlying theory of gas transfer, the boundary layer mechanisms for low to moderate wind speed, and the wind waves are presented. Chapter 3 describes the measurement techniques and their preprocessing that leads to the combined data sets in a single reference frame used for further analysis. It also outlines the scope of the measurement campaign that will be evaluated in this thesis, the so called Fetch Experiment (FE). Chapter 4 lists the evaluation techniques and algorithms used and implemented to derive the wind and fetch dependent parameters of the waves, and of microscale breaking, that will then be presented in chapter 5, followed up by the conclusion of this thesis in chapter 6.

Chapter 2

Theory

This chapter governs the basic theory concerning gas exchange between air and water, mechanisms in the water sided mass boundary layer for low to moderate wind speeds, and wind-driven waves.

2.1 Gas transfer across the air-water interface

This section is about the basics of gas and heat transport across the air-water interface and characteristic parameters such as the transport velocity k . It also gives a brief outline of commonly used models for transport across the air-water interface.

2.1.1 Transport equations

The diffusion flux j of a given concentration c over a given distance z of a gas is given by Fick's 1st law

$$\vec{j} = -D\vec{\nabla}c \quad (2.1)$$

with the molecule and temperature dependent diffusion coefficient D (Roedel and Wagner, 2017). The continuity equation is given as

$$\frac{\partial c}{\partial t} + \vec{\nabla} \cdot \vec{j} = 0. \quad (2.2)$$

In the case of a constant diffusion coefficient D , this leads to Fick's 2nd law

$$\frac{\partial c}{\partial t} = D\Delta c. \quad (2.3)$$

For heat, the concentration is replaced by $c = c_p\rho T$ with the specific heat capacity c_p , the density ρ , and the temperature T . Replacing the diffusion constant with the thermal diffusivity χ yields

$$\frac{\partial T}{\partial t} = \chi\Delta T. \quad (2.4)$$

Adding the transport by advection with the velocity \vec{u} leads to the diffusion-advection equation with no chemical reactions

$$\frac{\partial c}{\partial t} + \vec{u}\vec{\nabla}c = D\Delta c. \quad (2.5)$$

Given the case of a transport in just one direction z with the velocity component w and using the Reynolds decomposition of the concentration $c = C + c'$ into a mean concentration C and into a fluctuation term c' we can rewrite the diffusion-advection equation to

$$\frac{\partial c}{\partial t} = D\Delta c - \nabla(c'w'). \quad (2.6)$$

The turbulent diffusion coefficient K is defined as

$$K := -\frac{c'w'}{\frac{\partial c}{\partial z}} \quad (2.7)$$

and is typically much larger than the molecular diffusion coefficient D ($K \gg D$). This changes, however, close to the boundary of the fluid (see section 2.1.2). Both coefficients contribute to the flux leading to

$$j = -(K + D)\nabla c. \quad (2.8)$$

Given the case of a flow in a singular direction z , the transfer resistance R is described as

$$R = \frac{c(z_1) - c(z_0)}{j} = -\int_{z_0}^{z_1} \frac{1}{D + K(z')} dz'. \quad (2.9)$$

Its inverse has the units m s^{-1} and is called transfer velocity k

$$k = \frac{j}{c(z_1) - c(z_0)}. \quad (2.10)$$

Respectively, the heat transfer velocity k_h is given as

$$k_h = \frac{j}{c_p \rho_w \Delta T} \quad (2.11)$$

with c_p , the density of water ρ_w , and the temperature difference ΔT .

The definition of the dimensionless transfer velocity k_+ is given as the transfer velocity k divided by the water sided friction velocity $u_{*,w}$ (see section 2.2.2)

$$k_+ = \frac{k}{u_{*,w}}. \quad (2.12)$$

The boundary layer thickness z_k , a fictional sublayer of the viscous boundary layer with only molecular transport (Jähne, 1985; Jähne et al., 1989; Steele et al., 2009), is defined as

$$z_k = \frac{D}{k}. \quad (2.13)$$

The water sided mass boundary layer has a typical thickness on the order of $100 \mu\text{m}$ Jähne et al. (1987). The transport across the air-sea boundary layer can also be described by a time constant t_k

$$t_k = \frac{z_k}{k} = \frac{D}{k^2}. \quad (2.14)$$

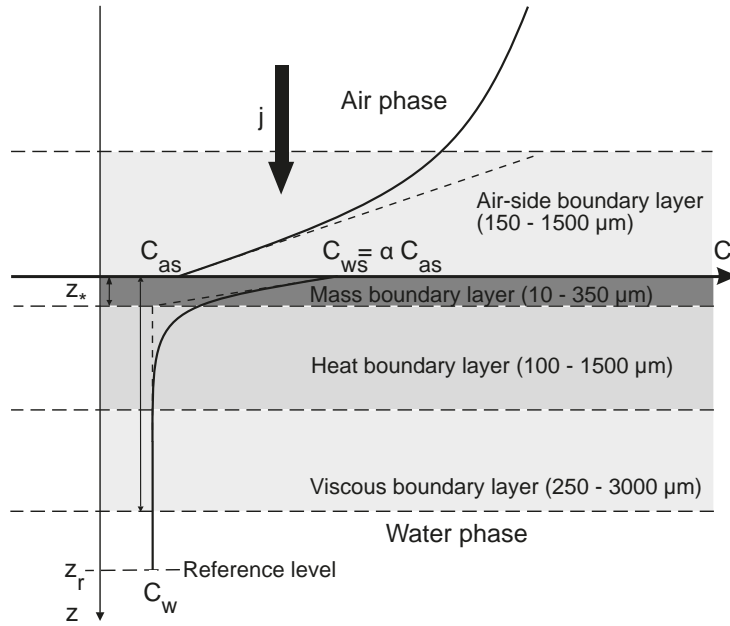


FIGURE 2.1: Sketch of the mass boundary at the air-water interface by Kunz and Jähne (2018).

2.1.2 Transport across the interface

The transport of a gas across an interface, e.g. the air-water interface is mainly controlled by a thin interfacial layer, the so called mass boundary layer (figure 2.1). It is a sublayer of the viscous boundary layer (where the wind profile changes from logarithmic to linear) and is often defined as the layer where the transport by molecular diffusion exceeds the transport by turbulent diffusion, caused by the decrease in the size of turbulent vortices close the the interface.

Given a certain concentration c of a gas in an air compartment, there exists an equilibrium concentration of the same gas in a connected water compartment given by the solubility α ,

$$c_{w,s} = \alpha c_{a,s}. \quad (2.15)$$

For $\alpha \neq 1$ there occurs a concentration jump at the water surface (Jähne, 1980), which leads to different total transfer velocities for air side $k_{a,\text{total}}$ and water side $k_{w,\text{total}}$

$$\frac{1}{k_{a,\text{total}}} = \frac{1}{k_a} + \frac{1}{\alpha k_w} \quad (2.16)$$

$$\frac{1}{k_{w,\text{total}}} = \frac{\alpha}{k_a} + \frac{1}{k_w} \quad (2.17)$$

with the air sided transfer velocity k_a and the water sided transfer velocity k_w . Therefore, the solubility α is the parameter that defines if the transport is water or air sided

dominated

$$k_{a,\text{total}} = \alpha k_{w,\text{total}}. \quad (2.18)$$

Thin film model

The thin film model assumes a thin layer of solely molecular diffusion in the mass boundary layer (Whitman, 1962). The boundary layer thickness is given as

$$z_* = \frac{11\nu}{u_{*,w}} \quad (2.19)$$

with ν the kinematic viscosity of water, and u_* the water sided friction velocity (see section 2.2.2). Hereby, 11 represents the intercept between the logarithmic representation of the wind profile and the linear representation (Roedel and Wagner, 2017). This yields for the concentration difference between the water surface and the boundary layer thickness z_*

$$\Delta c = j \int_0^{z_*} \frac{1}{D} dz' = \frac{j}{D} \frac{11\nu}{u_{*,w}} \quad (2.20)$$

and leads to the transfer velocity

$$k = \frac{j}{\Delta c} = \frac{1}{11} \frac{D}{\nu} u_{*,w}. \quad (2.21)$$

Surface renewal model

In contrast to the thin film model, the surface renewal model represents a renewal of the water surface by turbulent eddies as a statistical process. It was first proposed by Higbie (1935) and Danckwerts (1951). An extension that also applies to a rigid surface was added by Jähne et al. (1989). In the surface renewal model, a new parameter, the so called renewal time τ was introduced as proportional to the depth z to the power of p ($p \geq 0$).

$$\tau \propto \frac{1}{z^p}. \quad (2.22)$$

The averaged transport equation solved by Higbie (1935) and Danckwerts (1951), equivalent to the case of $p = 0$ and a free surface, yields

$$D \frac{\partial^2 c}{\partial z^2} - \frac{c}{\tau} = \frac{\partial c}{\partial t} = 0. \quad (2.23)$$

Solving equation 2.23 leads to the exponential concentration profile

$$c(z) = c_b + (c_s - c_b) \exp -\frac{z}{\sqrt{D\tau}} \quad (2.24)$$

with the bulk concentration c_b (the concentration in the well mixed water body) and the surface concentration c_s . This yields for the transfer velocity k

$$k = \frac{j}{c_s - c_b} = \frac{D}{z_*} = \frac{D}{\sqrt{D\tau}} = \left(\frac{D}{\tau}\right)^{\frac{1}{2}}. \quad (2.25)$$

A dimensional analysis leads to the following equation of the renewal time τ

$$\tau = \frac{\nu}{u_{*,w}^2} \beta^2 \quad (2.26)$$

with a dimensionless scaling factor β , which leads to

$$k = \frac{1}{\beta} \left(\frac{D}{\nu}\right)^{\frac{1}{2}} u_{*,w}. \quad (2.27)$$

The solution of equation 2.27 is for a free surface. With the additional parameter p by (Jähne et al., 1989) that varies between 0 and 1 it yields

$$k \propto \frac{\nu^{-\frac{p+1}{p+2}}}{D}. \quad (2.28)$$

which includes the solution for a free surface for $p = 0$.

Multi-stage small-eddy model

Another approach by (Jähne, 1985; Jähne et al., 1989), the so called multi-stage small-eddy model (K-model), is given if the local turbulent diffusion coefficient K follows a power law with depth z

$$K \propto z^m \quad (2.29)$$

with the factor $m \geq 2$. The transfer velocity for high Schmidt numbers is then proportional to

$$k \propto \left(\frac{\nu}{D}\right)^{-\frac{m-1}{m}} \quad (2.30)$$

which gives for $m = 2$ the same Schmidt number exponent as the surface renewal model for a free surface.

2.1.3 Schmidt number

The Schmidt number Sc is defined as the ratio between the kinematic viscosity ν and the diffusion constant D of the respective tracer.

$$Sc := \frac{\nu}{D} \quad (2.31)$$

Using the Schmidt number and adding the variable Schmidt number exponent n ($\frac{1}{2} \leq n \leq \frac{2}{3}$), the transfer velocity of equation 2.27 can be rewritten as

$$k = \frac{1}{\beta} (\text{Sc})^{-n} u_* \quad (2.32)$$

Schmidt number scaling

The Schmidt number scaling can be used to determine the transfer velocity k_A of tracer A from the transfer velocity k_B of tracer B. For given heat transfer velocities, the Prandtl number is used instead of the Schmidt number with $\text{Pr} = 7$. However, the Schmidt number exponent n can only be determined if at least two tracer transfer velocities have been measured. The value of n can vary between $\frac{1}{2} \leq n \leq \frac{2}{3}$.

$$\frac{k_A}{k_B} = \left(\frac{\text{Sc}_A}{\text{Sc}_B} \right)^{-n} \quad (2.33)$$

2.2 Wind Waves

Wave breaking is often described in the context of observed parameters of the waves. Therefore, the investigation of the occurrence of microscale breaking and boundary layer streaks needs to be placed in the context of the waves. This section is about the wind wave theory related to the mechanisms observed in this study. Most of the content of this section is taken from Kinsman (1965), and Massel (2013).

The Navier-Stokes equation

$$\rho \left(\frac{\partial \vec{u}}{\partial t} + \vec{u} \cdot \vec{\nabla} \vec{u} \right) = -\nabla p + \vec{F} + \mu \nabla^2 \vec{u} \quad (2.34)$$

describes the motion of a fluid. The mass in an incompressible fluid is conserved via the continuity equation:

$$\vec{\nabla} \cdot \vec{u} = 0. \quad (2.35)$$

2.2.1 Dispersion relation

The dispersion relation for gravity waves, with gravity as the restoring force, in water is given as

$$c_p = \left(\frac{g\lambda}{2\pi} \tanh \left(\frac{2\pi d}{\lambda} \right) \right)^{\frac{1}{2}}. \quad (2.36)$$

Here, c_p represents the wave phase velocity, g is the gravitational acceleration, λ is the wavelength of the wave, and d is the water depth. For deep water (i.e. $d \gg \lambda$) the dispersion relation can be approximated as

$$c_p = \left(\frac{g\lambda}{2\pi} \right)^{\frac{1}{2}}. \quad (2.37)$$

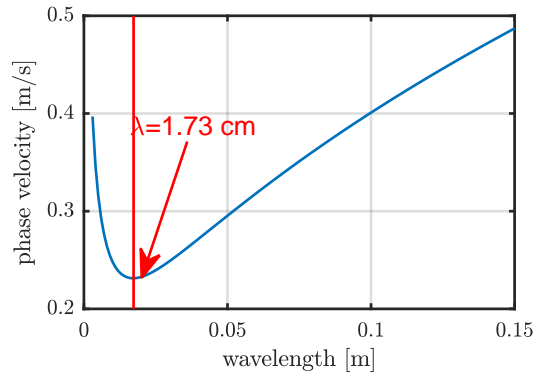


FIGURE 2.2: Dispersion relation of gravity-capillary waves in deep water. The minimum wavelength is at 1.73 cm.

Gravity-capillary waves

The dispersion relation for gravity-capillary waves is given as

$$\omega^2 = \left(gk + \frac{\sigma}{\rho} k^3 \right) \tanh(kh_d) \quad (2.38)$$

with $\omega = \frac{2\pi}{T}$ and the wave number $k = \frac{2\pi}{\lambda}$. The restoring force of capillary waves is the surface tension. All fetch experiment data sets lie in the range of the deep water waves which means the term $\tanh(kh_d)$ with the water depth h_d is approximately 1. The wave phase velocity c_p for deep water waves in dependence on the wavelength λ is then given as

$$c_p = \left(\frac{g\lambda}{2\pi} + \frac{\sigma}{\rho} \frac{2\pi}{\lambda} \right)^{\frac{1}{2}}. \quad (2.39)$$

σ represents the surface tension, and ρ the density of water. The minimum phase speed of deep water waves is thereby given as 23.2 cm s^{-1} at a wavelength of 1.73 cm (see figure 2.2).

2.2.2 Friction velocity

The friction velocity is given as

$$u_* = \left(\frac{\tau_{xz}}{\rho} \right)^{\frac{1}{2}} \quad (2.40)$$

with the shear stress τ_{xz} and the density ρ Roedel and Wagner (2017).

Friction velocities are only available for the infinite fetch data. However, a recent investigation by Schwenk (2019) determined the water sided friction velocity $u_{*,w}$ in the Aeolotron for the duration limited wave growth and found a nearly constant friction velocity for a given wind speed and over a time period of 500 s.

Different parameterizations to determine the friction velocity based on different parameters are available in the literature. A parameterization of the friction velocity for the open ocean by Gao et al. (2009) states that

$$u_{*,a} = c_g u_{10}^{\frac{4}{3}} c_p^{-\frac{1}{3}}, \quad (2.41)$$

with u_{10} the wind speed in ten meters height, $c_g = 0.0362$ an experimentally determined constant, and c_p the phase speed of the dominant waves. It was derived from a dimensional analysis of sea data with wind speeds larger than $u_{10} = 6.44 \text{ m s}^{-1}$. Another parameterization, the 3/2-power law by Toba (1997) is given as

$$u_{*,a} = \left(\frac{h}{g^{\frac{1}{2}} 0.062 T_s^{\frac{3}{2}}} \right)^2 = \frac{h^2}{0.062^2 g T_s^3} \quad (2.42)$$

with the gravitational acceleration g , the significant wave height h , and the wave period T_s . Badulin et al. (2007) stated that the Toba 3/2-power law is a certain case of the weakly turbulent law and neglects the nonlinear wave growth.

2.2.3 Non-Dimensional Parameters

Mean square slope

The mean square slope is a dimensionless roughness parameter for the water surface and is defined as the variance of the surface slopes.

Reynolds number

The Reynolds number Re for water waves is given as

$$Re = \frac{c_p h}{\nu} \quad (2.43)$$

with the phase velocity c_p , the wave height h , and the kinematic viscosity of water ν . It can be used to describe if a flow is turbulent or laminar. Larger Reynolds numbers refer to turbulent flow and smaller Reynolds numbers refer to laminar flow.

Another definition of the Reynolds number is the so called windsea Reynolds number and it is defined as

$$Re_b = \frac{u_*^2 T_s}{\nu} \quad (2.44)$$

with the wave period T_s , the friction velocity u_* and the kinematic viscosity of water ν .

The water surface can act as either a smooth surface or as a rough surface. Therefore, a roughness Reynolds number can be defined given as

$$\text{Re}_0 = \frac{u_* z_0}{\nu} \quad (2.45)$$

with the friction velocity u_* , the roughness parameter z_0 with the units of metres, and the kinematic viscosity ν (Roedel and Wagner, 2017). According to Nikuradse (1933) the interface is completely smooth for $\text{Re}_0 < 0.13$ and it is completely rough for $\text{Re}_0 > 2.5$.

Weber number

The Weber number We is given as

$$\text{We} = \frac{\rho c_p^2 \lambda}{\sigma} \quad (2.46)$$

with ρ the density of water, c_p the phase velocity of the wave, λ the wavelength of the wave, and σ the surface tension. It is used in calculating the wave profile of Crapper waves (Murashige and Choi, 2017) (see section 2.2.5).

2.2.4 Stokes waves

A well established theory for wind induced gravity waves are Stokes waves (see figure 2.3). They are called gravity waves because gravity is the main driving force. For the combined gravity-capillary waves dispersion relation, a good approximation for purely gravity driven waves is when the wavelength is larger than 7 cm. The third order approximation of the elevation η of a stokes wave is given as

$$\eta(x, t) = a \left(\left[1 - \frac{1}{16}(ka)^2 \right] \cos(\theta(x, t)) + \frac{1}{2}(ka) \cos(2\theta(x, t)) + \frac{3}{8}(ka)^2 \cos(3\theta(x, t)) \right) \quad (2.47)$$

k is the wavenumber, a is the wave amplitude, and $\theta(x, t) = (kx - \omega t)$.

For Stokes Waves, the Stokes' criterion for breaking is a when the crest angle of the wave exceeds 120° . This also corresponds to a maximum wave steepness of

$$\delta_{\text{max, Stokes}} = 0.142. \quad (2.48)$$

2.2.5 Crapper waves

Crapper waves are a solution for pure capillary waves and the solution for the wave form is given as

$$x(\sigma) = -\sigma + 4 \frac{A \sin \sigma}{1 + A^2 + 2A \cos \sigma} \quad (2.49)$$

$$y(\sigma) = -4 \left(1 - \frac{1 + A \cos \sigma}{1 + A^2 + 2A \cos \sigma} \right) \quad (2.50)$$

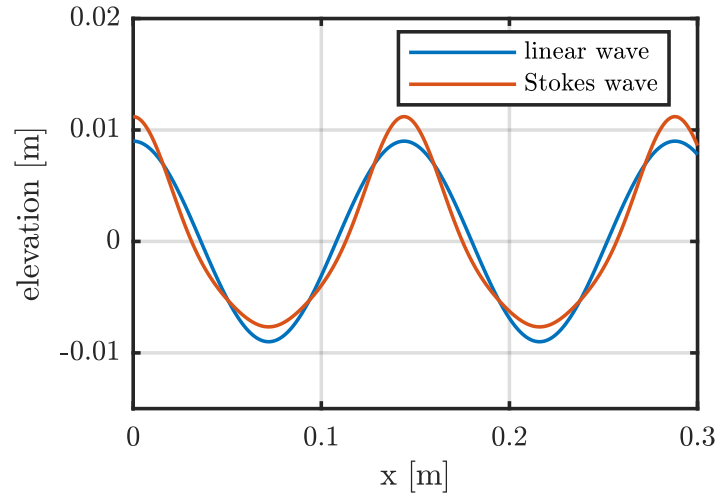


FIGURE 2.3: Example of a stokes wave compared to a linear wave.

with $-\pi < \sigma < \pi$, A given as

$$A = \frac{\left(\frac{2\pi}{We} - 1\right)}{\left(\left(\frac{2\pi}{We}\right)^2 - 1\right)^{\frac{1}{2}}} \quad (2.51)$$

and the steepness given as

$$\frac{h}{\lambda} = \frac{2}{\pi} \left(\left(\frac{2\pi}{We} \right)^2 - 1 \right)^{\frac{1}{2}} \quad (2.52)$$

(Murashige and Choi, 2017). The surface tension is the main driving force of crapper waves. If the steepness of crapper waves exceeds a limit of

$$\delta_{\max, \text{Crapper}} = 0.73, \quad (2.53)$$

adjacent crapper waves start to overlap each other and cause an instability with bubble entrainment. This steepness corresponds to a Weber number of $We = 4.129$ (see figure 2.4).

2.2.6 Parasitic capillary waves

Parasitic capillary waves have been studied for a long time. Important theories have been developed by Longuet-Higgins (1995) and Fedorov et al. (1998). In contrast to the dispersion relation for gravity-capillary waves, the parasitic capillaries ride on the lee side of the gravity wave with the same phase speed as the underlying gravity wave and their occurrence is linked to higher harmonics of the underlying wave that are amplified by a resonance (Fedorov et al., 1998).

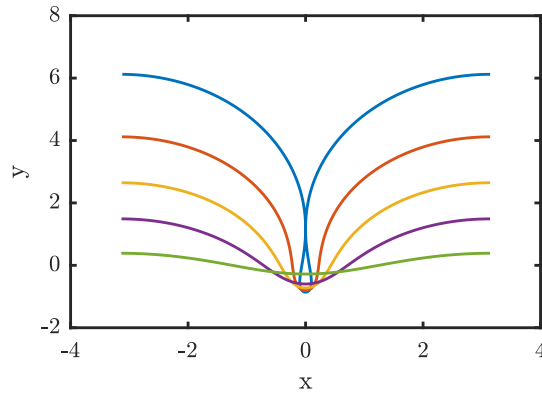


FIGURE 2.4: Crapper waves with different steepness from bottom to top: 0.11, 0.30, 0.44, 0.58, and 0.73.

2.2.7 Wave height

There exist different definitions to quantify the heights of the waves. A well established one is the significant wave height. It is defined as

$$h = 4\sqrt{\eta^2} = 4\sigma(\eta) \quad (2.54)$$

with η as the wave elevation, and represents the mean of the one-third highest waves Kinsman (1965). It can be calculated as four times the standard deviation σ of the wave elevation. It will be used in this thesis.

2.2.8 Wave breaking

Wave breaking with bubble entrainment is often classified in four different types, namely spilling breakers, plunging breakers, collapsing breakers, and surging breakers (Sunamura and Okazaki, 1996).

The Iribarren number ζ is a dimensionless parameter introduced to describe the type of wave breaking for deep water waves of significant wave height h and gravity wavelength λ over a topography inclined by a certain angle γ (Hughes, 2004). In some literature it is called the surf similarity parameter. The typical values of the Iribarren number for the different types of breaker are

$$\begin{array}{c|c|c} \text{surging or collapsing} & \text{plunging} & \text{spilling} \\ \zeta < 0.5 & 0.5 < \zeta < 3.3 & 3.3 < \zeta \end{array}$$

as given in Battjes (1974).

Dividing the Iribarren number ζ by the tangens of the topography inclination, an adapted Iribarren number ζ' can be written as

$$\zeta'(h, \lambda) = \frac{\zeta}{\tan \gamma} = \left(\frac{\lambda}{h}\right)^{0.5}. \quad (2.55)$$

The reason behind the introduction of the adapted Iribarren number is, that for the toe and bulge formations (see figure 2.5) of the wave crest in the case of microscale breaking, there can be a hidden information in the gravity wave that may act as an underlying slope structure, such as for example the asymmetry of the gravity wave, or the gravity wave phase position of the MB initiating disturbance.

In the context of different types of breaking waves, different types of microscale breaking will be introduced, as observed utilizing the measurement techniques of the FE. For a clean water surface with no surfactants, there exist two extrema of microscale breaking, that might indicate different types of microscale breaking.

2.2.9 Wave growth

Several theories exist, that describe the growth of the wave field. Most theories, such as the theories by e.g. Sverdrup and Munk (1947), Hwang (2006), and Fontaine (2013) differentiate between laws for the duration limited wave growth and the fetch limited wave growth. Considering the FE, the finite fetch measurements would then fall into the fetch limited case while the infinite fetch conditions would be considered in the duration limited wave growth regime.

Donelan et al. (1992) determined the fetch x in dependence on wave age τ (with the wave phase velocity c_p and the wind speed in ten meters height u_{10}) given as

$$\tau = \frac{c_p}{u_{10}} \quad (2.56)$$

of the growth rate of wind-generated waves under a constant wind to be

$$x = \alpha \cdot \ln \left(\frac{\tau^{-1}}{\tau^{-1} + \beta} \right) + \gamma (\tau^{-1} + \delta) \cdot \tau^2 \quad (2.57)$$

with $\alpha = 4.09 \times 10^4$, $\beta = -0.83$, $\gamma = -3.4 \times 10^4$, and $\delta = 0.415$.

2.3 Mechanisms in the mass boundary layer

This section is about the predominant mechanisms occurring in the mass boundary layer for low to moderate wind speeds. While for the turbulent regime, these are mainly microscale wave breaking and streak formation (often referred to as micro-Langmuir streaks), especially in the laminar regime, the dominant mechanism is surface renewal by local upwelling events, referred to as horseshoe vortices.

2.3.1 Microscale wave breaking

Microscale wave breaking (MB), small breaking events of the waves without bubble entrapment (Banner and Phillips, 1974) are known to cause a local renewal of the

boundary layer with the well mixed bulk water. This mechanism is thought to be the main driving mechanism of local heat and gas transfer for low to moderate wind speeds (Siddiqui et al., 2004; Siddiqui and Loewen, 2007).

There exist many descriptions of the microscale breaking event. However, the exact nature of the mechanism causing the initial disturbance that creates the high vorticity in the wave crest is so far not well understood (Siddiqui and Loewen, 2007).

Some descriptions focus on the knobby flow, or wake turbulence, in the wake of the MB wave (see figure 2.5), where the water surface shows a rough pattern due to the underlying vortices of the surface renewal. Other definitions describe the presence of parasitic capillary waves and a bulge or toe forming at the wave crest as a necessary condition for MB (Longuet-Higgins, 1992; Komori et al., 1993; Peirson and Banner, 2003) where a bulge is the larger version of a toe, a small overhanging of the wave crest. Some of the literature descriptions that fit most with the experimental observations of the FE are mentioned in the following.

Longuet-Higgins (1994) described that the initial instability causing MB originates from the highly curved troughs of the capillary waves lee side of the toe. Duncan et al. (1999), and Qiao and Duncan (2001) specified in addition that vorticity in the bulge of the wave only occurs after the initial instability. Iafrati and Campana (2005) also mention secondary separation effects of the water surface skin layer from the troughs of the free surface fluctuations. Smaller MB events are initiated by a toe

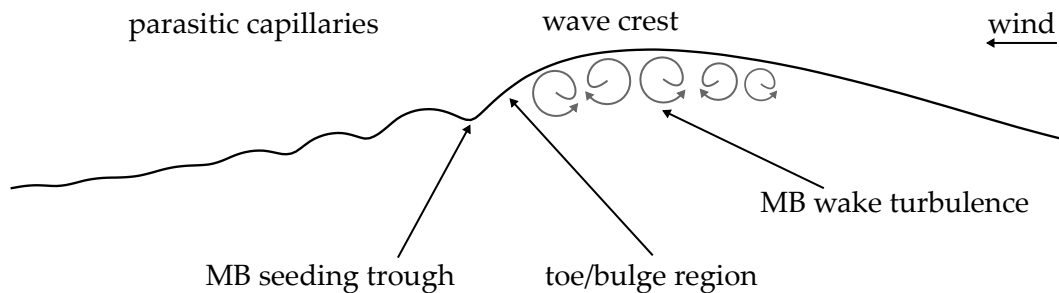


FIGURE 2.5: Wave elevation profile as reconstructed from the ISG slopes of a microscale breaking wave crest of the FE campaign.

formation at the wave crest, while larger MB events are accompanied by a bulge formation.

The impact of microscale wave breaking, i.e. the surface renewal regime observed as knobby flow in the wake of a breaker and the time the boundary layer needs to reform, is so far mostly studied by thermography imagery and water sided vorticity measurements utilizing LIF methods.

Several laboratory studies have been conducted to quantify the wind and fetch dependent abundance of MB. An established parameter to describe the occurrence of MB is the percentage of wave crests that break n_{break} of all measured wave crests

TABLE 2.1: Occurrence of MB in other studies

| Source | wind [m/s] | fetch [m] | MB [%] |
|----------------------------|------------|-----------|--------|
| Jessup et al. (1997) | 5 | 5 | 33 |
| Banner and Peirson (1998) | 4.8 | 4.35 | 53 |
| | 6.3 | 4.35 | 70 |
| | 8.1 | 4.35 | 89 |
| Siddiqui and Loewen (2007) | 4.5 | 5.5 | 11 |
| | 6.1 | 5.5 | 47 |
| | 7.4 | 5.5 | 80 |
| | 8.5 | 5.5 | 79 |
| | 11.0 | 5.5 | 90 |

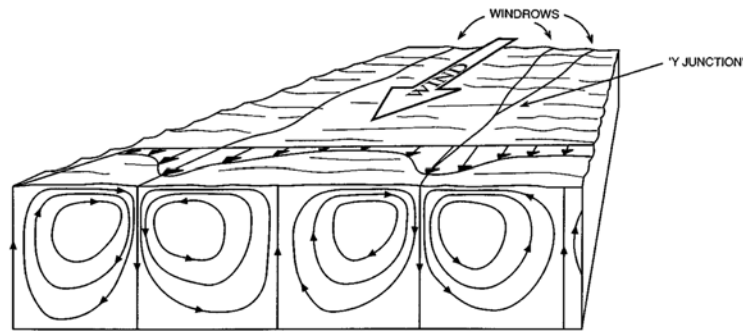


FIGURE 2.6: Sketch of Langmuir circulation by Thorpe (2004).

n_{all} per data set

$$MB = \frac{n_{\text{break}}}{n_{\text{all}}}. \quad (2.58)$$

Table 2.1 shows a list of the breaking percentage of wave crests from the literature.

2.3.2 Boundary layer streaks

A formation of streaks has been observed in both solid wall boundary layers and fluid-fluid boundary layers. The streak formation in fluids has been investigated in several studies. Some investigate the streak formation near solid walls (e.g. Chernyshenko and Baig (2005), Brandt (2014), Jung and Zaki (2015)). Streaks observed on the ocean surface at the fluid-fluid interface of water and air and also in small scale laboratory studies are often referred to as Langmuir circulation (LC) or micro Langmuir circulation (e.g. Veron and Melville, 2001, Tsai et al., 2013). The preferred wind speed condition under which these streaks occur is between $u_{10} = 3 \text{ m s}^{-1}$ and $u_{10} = 10 \text{ m s}^{-1}$ (Thorpe, 2004).

Langmuir circulation is described as counter rotating vortices below the water surface that cause a transport of boundary layer towards the converging vortices and thus causing streaky structures (see figure 2.6).

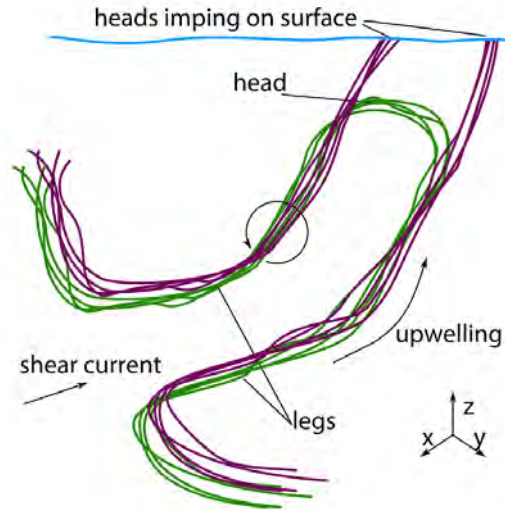


FIGURE 2.7: Development of the upwelling of a horseshoe vortex as proposed by Tsai (1998) and sketched by Kräuter (2015). The green lines show the early stage, and the violet lines the later stage of the horseshoe vortex.

A characteristic parameter studied in the context of boundary layer streaks is the streak spacing. Laboratory studies (under low to moderate wind speeds up to $u = 7 \text{ m s}^{-1}$) utilizing visualization methods such as thermography indicate a decrease in micro Langmuir streak spacing for a water sided friction velocity below $u_* = 0.7 \text{ cm s}^{-1}$ and a constant streak spacing above the given friction velocity (Schnieders et al., 2013; Handler et al., 2001). For wind speeds between $u_{10} = 10 \text{ m s}^{-1}$ to 16 m s^{-1} simulations lead to a different relationship between wind speed and streak spacing with a much larger spacing of the Langmuir circulation (Shuang and Jinbao, 2012).

A characteristic streak spacing l for purely shear induced turbulence is given as

$$l = 100 \frac{\nu}{u_*} \quad (2.59)$$

with the kinematic viscosity ν and the friction velocity u_* (Schnieders et al., 2013).

2.3.3 Horseshoe vortices

There exists a third mechanism, the so called local upwelling by horseshoe vortices (see figure 2.7). Tsai et al. (2005) proposed that the streaks are caused by the stretching of multiple upwelling events of horseshoe vortices. The streaky structure caused by the smearing out of the surface renewal area has been referred to as fish-scales (see figure 2.8) (Handler et al., 2001; Scott et al., 2008). By and large, the exact nature and cause of the fish-scales is still unclear. However, based on the observations of the FE data sets, this theory fits well with the fetch dependent development of the BLI data in the laminar regime (for further detail see section 5.5.1).

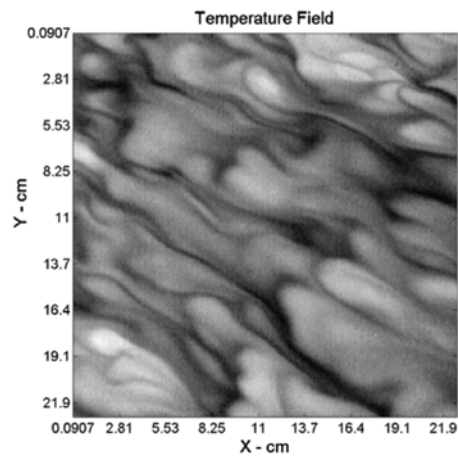


FIGURE 2.8: Fish-scales in thermal images of (Scott et al., 2008).

Chapter 3

Measurement techniques, facility, and measurement campaign

The preprocessing steps described in this chapter were implemented in a MATLAB object class and build the basic evaluation. Since all further processing is based on the output of the preprocessing mentioned in this chapter, the description of the processing steps is mentioned separately with the basic preprocessing written in this chapter, and the further processing steps described in chapter 4.

3.1 The Aeolotron

The Aeolotron is an air-tight annular wind-wave facility at the Heidelberg University, Germany. It has a flume width of 0.6 m and a mean diameter of 10 m. The water depth is 1 m, the channel height is 2.4 m, and the water volume is 18.000 l (see figure 3.1). Four axial fans are installed at the facility that provide wind speeds up to $u_{10} = 25.4(22) \text{ m s}^{-1}$. The uncertainty is given as brackets after the main part of the number. Besides measurements under quasi infinite fetch conditions, a mobile wave absorber can be installed (see figures 3.1 and 3.2). It enables fetch variable measurements between 1 m and 22 m.

3.2 Imaging slope gauge (ISG)

The imaging slope gauge (ISG) is a measurement technique to capture the slopes of the water surface (e.g. Jähne and Riemer, 1990, Zhang and Cox, 1994, Kiefhaber et al., 2014). A red light source below the water compartment is coded to switch between four different intensity gradient wedges (see figure 3.3). The refraction of each wedge is captured with a high speed camera (*pco.dimax*). The combination of respectively two intensity wedges for the wave slopes in along-wind and in cross-wind direction lead to 2D slope data for the along-wind slopes s_x and cross-wind slopes s_y . It thereby utilizes a beforehand calibrated lookup table (LUT). Figure 3.4 shows a sketch of the geometry of the ISG.

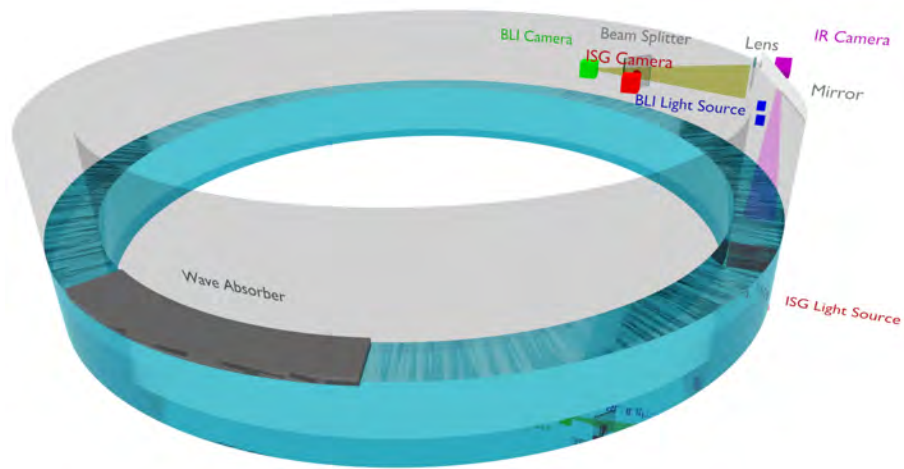


FIGURE 3.1: Sketch of the water and air compartment and the measurement setup of the annular wind wave facility Aeolotron, Heidelberg University. The diameter of the facility is 10 m, the flume width is 0.6 m, the channel height is 2.4 m and the water depth is 1 m. The wave absorber (depicted in gray) can be moved to enable measurements at varying fetches.

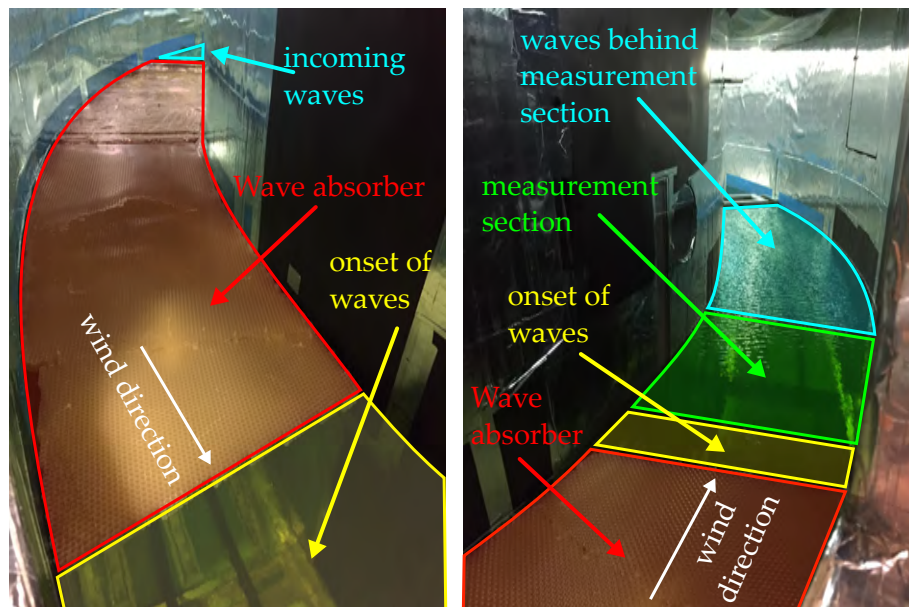


FIGURE 3.2: (left) Mobile wave absorber in the Aeolotron facility. (right) Onset of waves on the lee side of the wave absorber and measurement section of the Aeolotron facility.

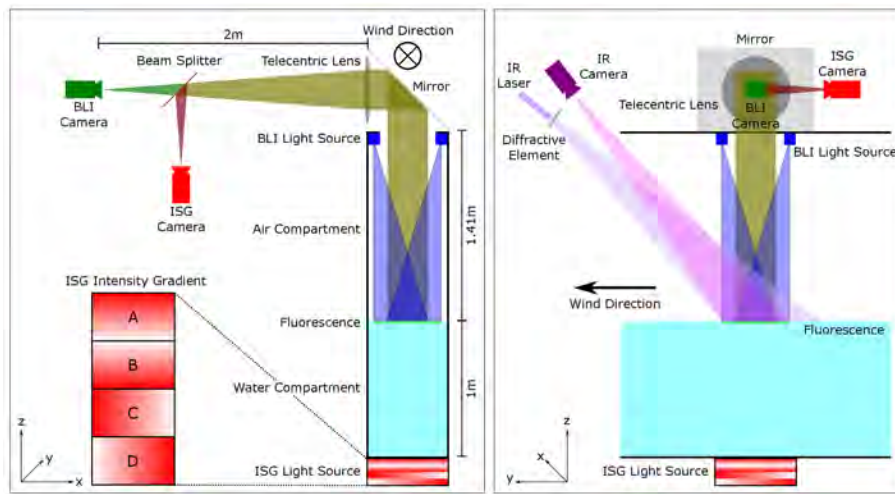


FIGURE 3.3: The combined measurement setup of the three imaging measurement techniques, ISG, BLI, and AT (see sections 3.2, 3.3, and 3.4).

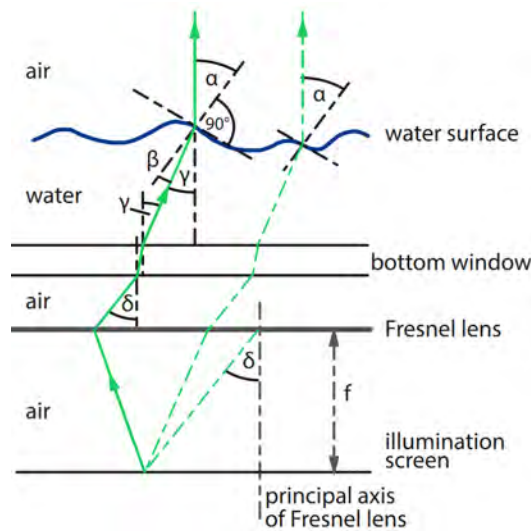


FIGURE 3.4: Refraction of the light at the water surface of the ISG setup as sketched by Kieffhaber et al. (2014). The illumination screen can quickly switch between the four intensity gradient wedges.

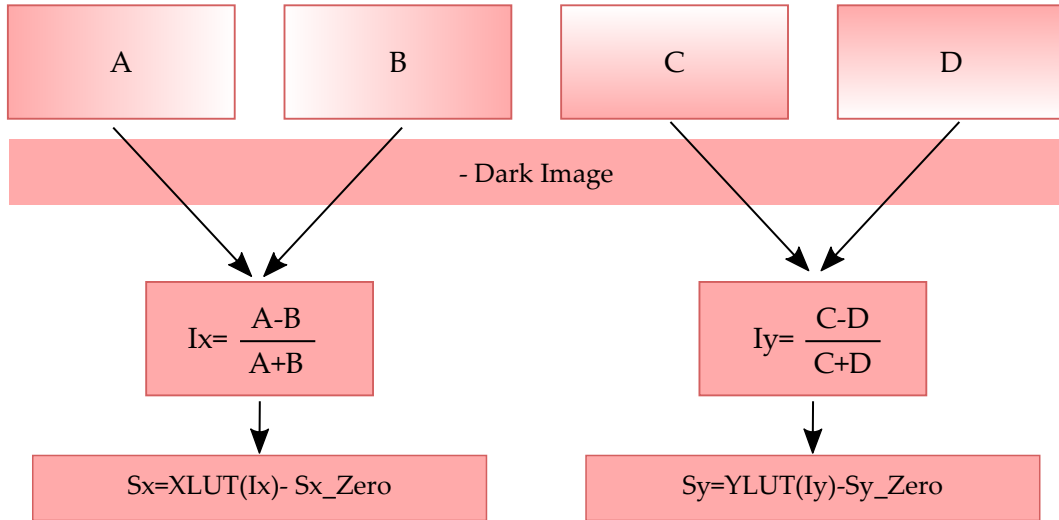


FIGURE 3.5: Preprocessing scheme of the ISG images to determine the wave slopes.

3.2.1 Preprocessing

Figure 3.5 shows the preprocessing scheme, that leads to the slope images of the ISG. First, the dark images are subtracted from the four intensity gradient images. Afterwards, intensity images of the along-wind and cross-wind slopes are calculated. The intensities are then converted to slope values utilizing a look up table (LUT) that was created beforehand using a special calibration bowl. Lastly, the zero slope values are subtracted.

3.3 Boundary layer imaging (BLI)

The boundary layer thickness measurements have been conducted using the boundary layer imaging (BLI) measurement technique developed by Kräuter (2015), Kräuter et al. (2014) based on an idea by Hiby et al. (1967). While it was initially proposed for the investigation of the gas absorption in falling films, Jähne (1985), however, was the first to suggest its application in the investigation of gas exchange processes. First experiments utilizing a 3-D reconstruction of the boundary layer have been done by Trofimova (2015). A similar method visualizing the mass boundary layer was developed by Roth (2018).

The pH dependent fluorescence dye 8-Hydroxypyrene-1,3,6-Trisulfonic Acid (HPTS, also called Pyranine) is added to deionized water. Hydrochloric acid (HCl) is used to shift the pH value of the water to 3.7. When ammonia (NH_3) is added to the air compartment, it gets transported through the mass boundary layer to the water bulk and increases the pH value in the boundary layer (see figure 3.6). When the pH value is larger than 7, the dye starts to fluoresce green ($\lambda_{\text{max, emi}} = 511 \text{ nm}$) if it gets excited by a blue light source ($\lambda_{\text{max, abs}} = 455 \text{ nm}$) (see figure 3.7). To suppress

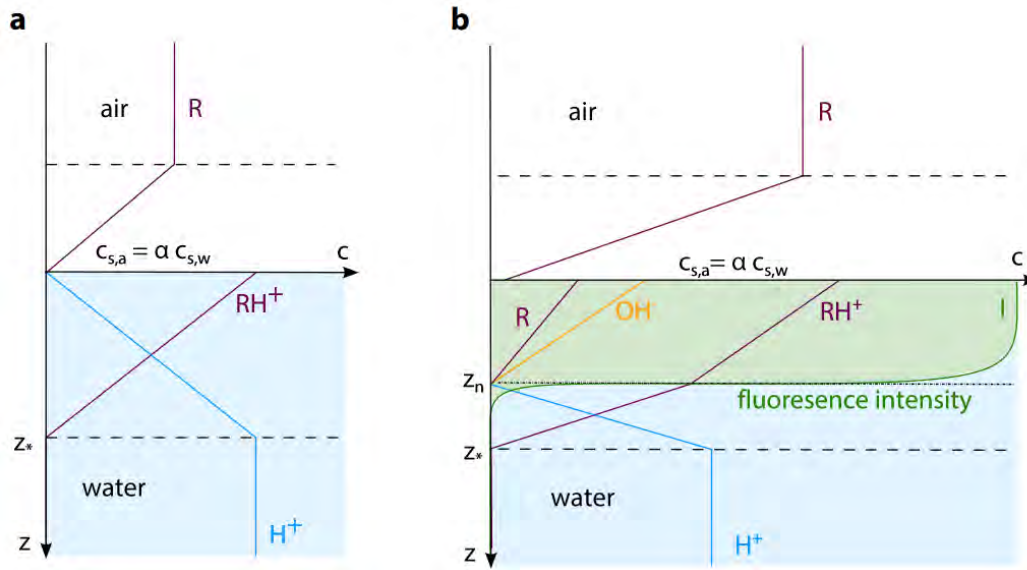


FIGURE 3.6: The invasion of an alkaline gas R (e.g. Ammonia) from air into water sketched as a concentration profile by Kräuter (2015). (a) shows the case when the alkaline gas completely reacts to RH^+ . Increasing the alkaline gas concentration in the air compartment (b) leaves an alkaline layer in the boundary layer. If the pH value is thereby increased over 7, the dye starts to fluoresce (here depicted as a green layer).

the background fluorescence of the water bulk, Tartrazine is added to the water as an absorbing dye to absorb the excitation light.

The fluorescence intensity is captured by an orthographic camera setup (*pco.edge*) with a field of view (FOV) of 20.7 cm by 17.7 cm, a spatial resolution of 0.23 mm and a temporal resolution of 0.01 s (see figure 3.3).

3.3.1 Preprocessing

The images captured with the BLI camera are stored as compressed images to enable a fast capturing frequency of 100 Hz. The used compression method is nearly lossless and is described in Jähne (2013). Figure 3.8 shows the preprocessing steps yielding the calibrated images. The gain was set to 4, and the offset was set to 80. The variable $g(x, y)$ represents the gray values of the pixels of the image.

The calibrated images still need to be further corrected for two effects. First, the refraction of the incident excitation light of the fluorescence causes a slightly inhomogeneous illumination of the boundary layer (see figure 3.9). Using Snellius law, the refraction of the incident light can be calculated using

$$\frac{n_1}{n_2} = \frac{\sin(\theta_2)}{\sin(\theta_1)} \quad (3.1)$$

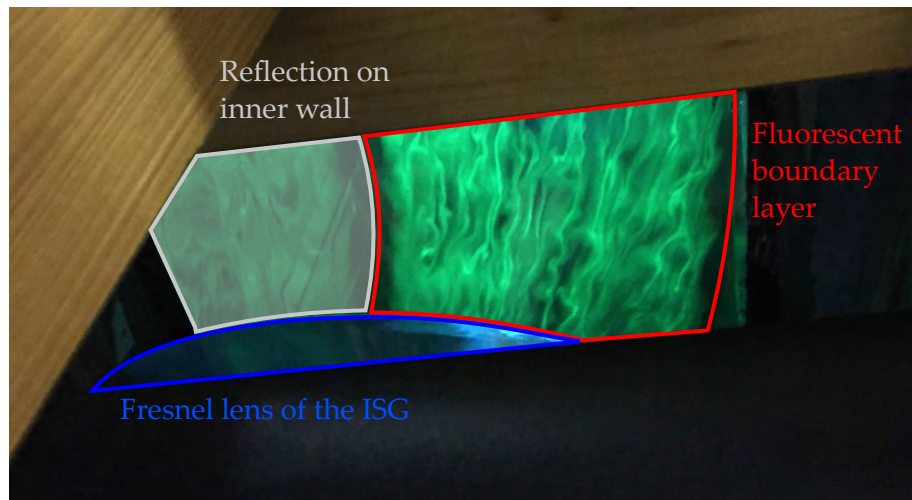


FIGURE 3.7: Green fluorescence of the boundary layer of the BLI technique as seen from below the measurement facility.

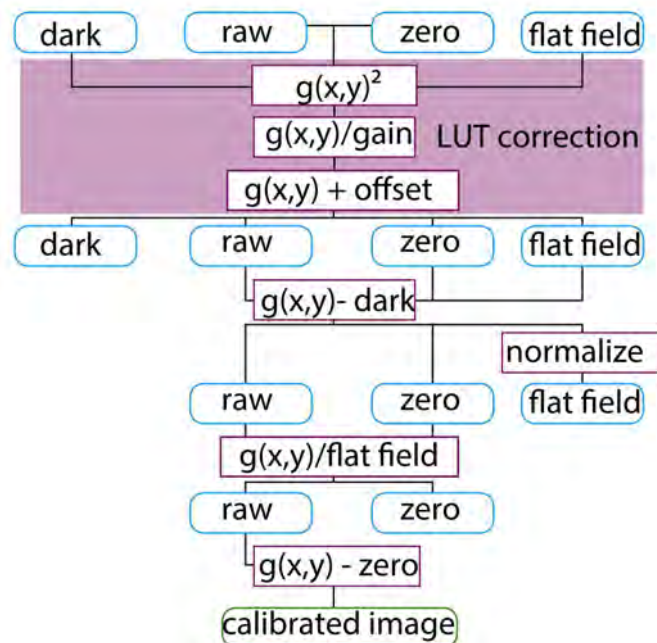


FIGURE 3.8: Preprocessing scheme of the BLI images by Kräuter (2015).

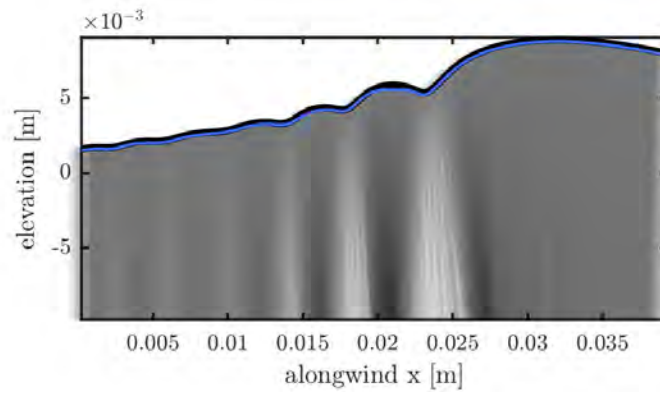


FIGURE 3.9: Refraction of the incident light due to the curvature of the water surface. The mass boundary layer is very thin and therefore only slightly affected (thickness indicated as blue line directly below the black line of the water surface). Still a small intensity variation across the parasitic capillary wave trains caused by this effect can be observed.

with the refraction index of air $n_1 = 1$, the refraction index of water $n_2 = 1.333$, the incident light angle θ_1 , and the refracted angle θ_2 (Demtröder, 2008).

Secondly, the observation of the boundary layer with the orthographic camera setup also exhibits a refraction of the viewing angle in the water sided mass boundary layer following equation

$$d_b = \cos \left(\arcsin \left(\frac{n_1}{n_2} \sin(s) \right) \right) d_m \quad (3.2)$$

with d_b the perpendicular thickness of the mass boundary layer with respect to the water surface, d_m the observed thickness of the mass boundary layer with BLI, and the slope s of the water surface utilizing the ISG data. An example of such a correction can be seen in figure 3.10.

The two additional calibration steps are shown in figure 3.11.

Since the slope of the water surface is captured with the ISG, it is possible to correct for these effects. However, the calculation of the correction is negligible for most cases. They were only applied for a detailed study of the strongly curved and strongly inclined parasitic capillary waves.

3.4 Active Thermography (AT)

Regarding thermography, there exists a differentiation between active and passive thermography. Utilizing active thermography, which was used in this thesis, an external heat source, here a CO_2 laser, actively heats the water surface and deposits a controlled heat flux density at the water surface. Active thermography was first used by Jähne et al. (1987) and Libner (1987).

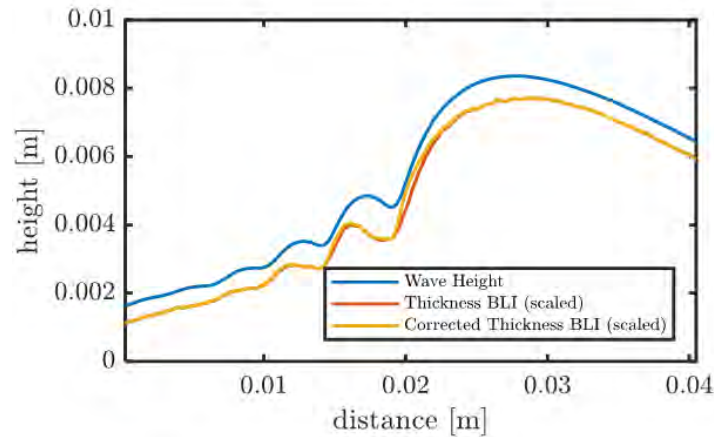


FIGURE 3.10: Correction of the observed mass boundary layer thickness for the slope of the water surface and therefore inclined observation of the orthographic BLI setup. The shown thickness is exaggerated compared to the actual thickness, so that the differences are visible.

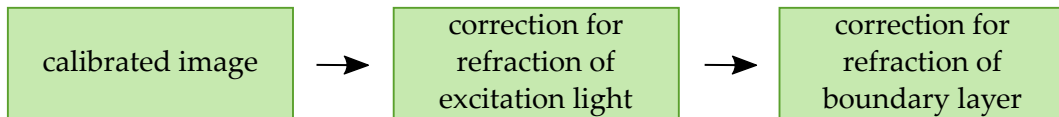


FIGURE 3.11: Additional calibration steps of the BLI images for the closer investigation of image regions with large slopes and/or high curvature.

The AT setup of the FE campaign was adjusted in a way that the fully heated area (see figure 3.12) was in the FOV of the BLI and the ISG setup.

A detailed description of the active thermography measurement technique can be found in Kunz (2017). An overview of the evaluation steps of the multifrequency excitation method by Kunz (2017) is shown in figure 3.13.

3.5 Fetch experiment (FE)

The fetch experiment (FE) is a measurement campaign conducted in 2017 with the goal to facilitate understanding of the fetch dependent development of the boundary layer mechanisms driving local gas and heat transfer. It is a crucial step to improve the comparability of field data and laboratory data since most laboratory facilities can only simulate the ocean for relatively short and often even only constant fetches that do not necessarily compare to the long fetches that can be achieved on the open ocean under steady wind conditions.

The first half of the experiment with water charge 1 was conducted together with Dr. Jakob Kunz, who supervised the fetch dependent active thermography measurement setup.

The second half of the experiment was conducted together with Dr. Kerstin Krall,

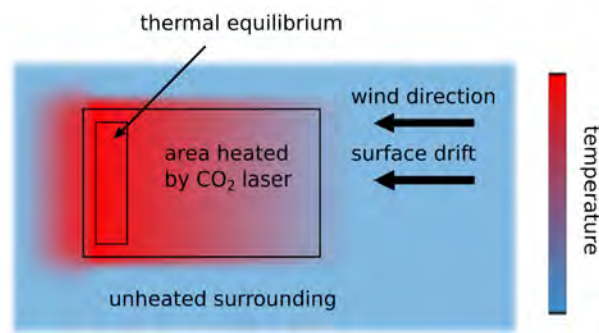


FIGURE 3.12: Heating of the water surface as sketched by Kunz (2017). The BLI and ISG setup FOV were chosen as to lie within the fully heated area of the heating scheme of the AT setup.

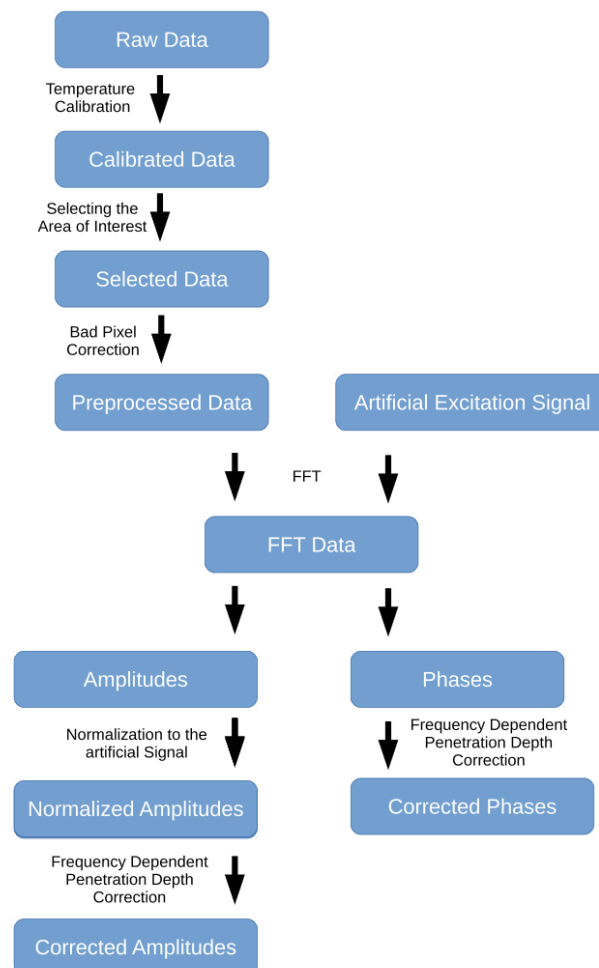


FIGURE 3.13: Evaluation steps of the multifrequency method of the thermography setup as sketched by Kunz (2017). The temperature calibration of the data is done before saving the data. The area of interest is then chosen manually as the heated area in thermal equilibrium in figure 3.12. All the additional steps are then carried out by the MATLAB evaluation script developed in Kunz (2017).

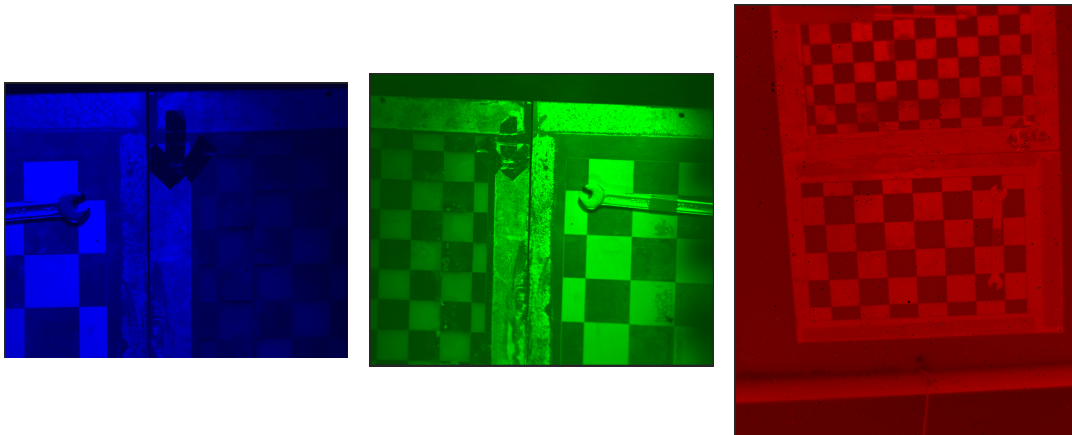


FIGURE 3.14: Falsecolor images of the checkerboard pattern captured with the three measurement setups from left to right: ISG, BLI, and AT.

that provided the global gas transfer velocities for the second water charge measurements.

The wind speeds, infinite fetch friction velocities, and the bulk water velocities were evaluated by Dr. Maximilian Bopp.

3.5.1 Data merging

Each measurement technique (ISG, BLI, and AT) delivered a time stack of raw data images that at first needed to be transformed to the same coordinate system and matched into the same coordinate reference frame, before applying further evaluation techniques.

Therefore, a checkerboard pattern was captured with all three measurement techniques, the recorded data are then mapped onto the ISG coordinate frame as determined using the checkerboards (see figure 3.14).

The AT images need to be rotated by 90 degree. Afterwards the image needed to be flipped upside down using the *flipud* function of MATLAB, since the ISG and BLI were observing the water surface through a mirror and the AT setup was not. Afterwards, a geometric transformation was used to map the AT field of view (FOV) onto the ISG FOV by applying the built in function *fitgeotrans* of MATLAB and using the corners of the checkerboard pattern as reference points.

The BLI images need to be flipped sideways using *fliplr* from MATLAB, since the ISG in comparison with the BLI setup is observing the water surface additionally using a beam splitter and therefore left and right are switched. The BLI images are then also transformed to the reference frame of the ISG using the *fitgeotrans* function. The final transformed images are shown in figure 3.15. The image size of the final coordinate frame is 901 pixels along-wind times 768 pixels cross-wind with a resolution of 0.23 mm in each direction and thus covers a water surface area of 366.1 cm². As a result of the calibration, the temperature, and the qualitative boundary layer

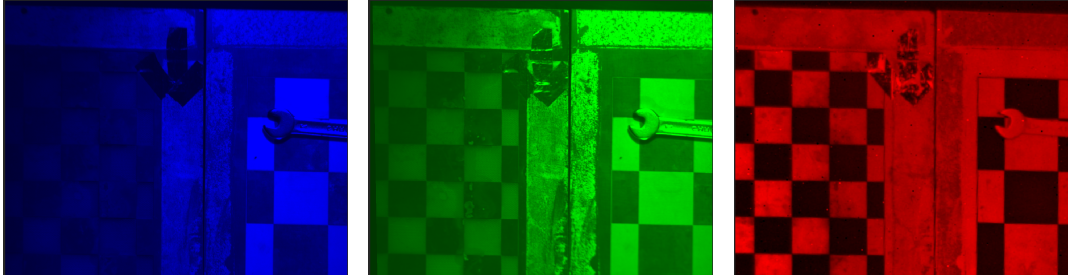


FIGURE 3.15: Falsecolor images of the finished mapping of the checkerboard pattern onto the ISG reference. The temperature image of the thermography setup shows the inverse intensity pattern for the checkerboard. This is due to the fact, that the dark areas on the checkerboard were warmer than the bright areas.

TABLE 3.1: All fetch and wind conditions of the FE. The frequency of the wind generator is given as f_{wind} . u_{10} is the calculated reference wind speed in 10 meters height and $u_{*,w}$ is the water sided friction velocity.

| f_{wind} [Hz] | u_{10} [m s ⁻¹] | $u_{*,w}$ [cm s ⁻¹] | fetches [±0.15 m] | | | | | | | | | | | |
|---------------------------|----------------------------------|------------------------------------|----------------------|---|---|---|---|---|----|----|----|----|----------|----------|
| 5 | 2.4(2) | 0.253(21) | | | | | | | | | | | | infinite |
| 7.5 | 3.7(2) | 0.382(24) | 2 | 3 | 4 | 5 | 6 | 8 | 10 | 12 | 16 | 21 | infinite | |
| 10 | 4.8(3) | 0.505(38) | 2 | 3 | 4 | 5 | 6 | 8 | 10 | 12 | 16 | 21 | infinite | |
| 12.5 | 6.2(4) | 0.666(48) | 2 | 3 | 4 | 5 | 6 | 8 | 10 | 12 | 16 | 21 | infinite | |
| 15 | 7.4(4) | 0.832(62) | 2 | 3 | 4 | 5 | 6 | 8 | 10 | 12 | 16 | 21 | infinite | |
| 17.5 | 8.9(5) | 1.066(85) | | | | | | | | | | | infinite | |

thickness can be mapped onto the slope images of the water surface and the influence of the waves on the pattern can be investigated (see figure 3.16).

3.6 Overview of the measurement conditions

The FE utilized the above imaging techniques ISG, BLI and AT with additional measurements of temperature, wind speed, and for selected infinite fetch data sets gas exchange rates determined using a mass balance method that integrated the exchange over the whole facility. An overview of all the measurement conditions can be seen in table 3.1. f_{wind} is the wind generator frequency of the Aeolotron, u_{10} is the equivalent wind speed in 10 m height, $u_{*,w}$ is the water sided friction velocity of the infinite fetch data, and the fetches are the length of water over which the wind blew until it reached the measurement section.

The mean squared slope of each measurement condition was tracked and the combined BLI, ISG and AT measurements were started after the wave field was in equilibrium, as indicated by a stagnation of the mean square slope value and the bulk velocity of the water. The combined data sets for each measurement condition of

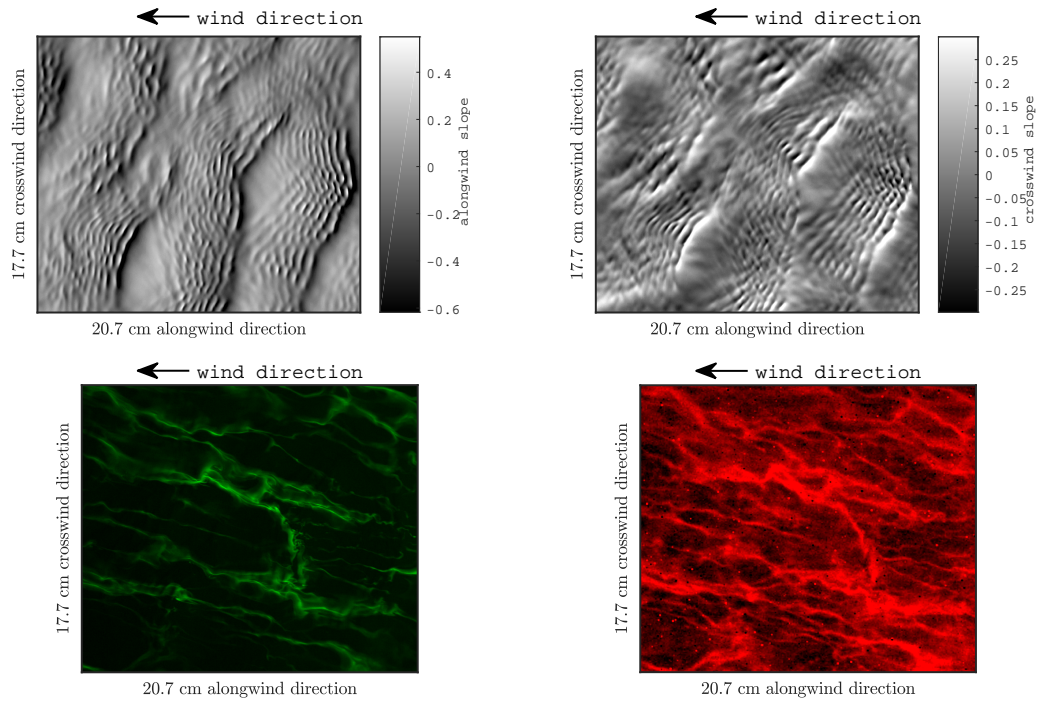


FIGURE 3.16: The finalized mapping of the BLI and AT images onto the slope images captured by the ISG setup.

each measurement technique give a time stack of 7500 images with a temporal resolution of 0.01 s, a spatial resolution of 0.23 mm and a spatial field of view of 20.7 cm times 17.7 cm.

Table 3.2 shows the different ammonia influx chosen for the infinite fetch data of water charge 1, and water charge 2. For water charge 2, a low and a high influx data set was captured separately to vary the visible fraction of the boundary layer.

TABLE 3.2: For the infinite fetch data, multiple data sets with a different fraction of the mass boundary layer visualized were captured. By changing the ammonia concentration in the air compartment, a variable visualization of the mass boundary layer could be achieved.

| f_{wind} [Hz] | u_{10} [m s ⁻¹] | $u_{*,w}$ [cm s ⁻¹] | infinite fetch | | |
|--------------------|----------------------------------|------------------------------------|------------------------|----------------|------|
| | | | ammonia influx [l/min] | | |
| | | | water charge 1 | water charge 2 | |
| 5.0 | 2.4(2) | 0.253(21) | | 0.08 | 0.11 |
| 7.5 | 3.7(2) | 0.382(24) | 0.09 | 0.07 | 0.10 |
| 10.0 | 4.8(3) | 0.505(38) | 0.13 | 0.12 | 0.15 |
| 12.5 | 6.2(4) | 0.666(48) | 0.16 | 0.16 | 0.20 |
| 15.0 | 7.4(4) | 0.832(62) | 0.20 | 0.30 | 0.50 |
| 17.5 | 8.9(5) | 1.066(85) | 0.40 | 0.40 | 0.60 |

Chapter 4

Evaluation Methods

4.1 Wave properties

The wind-wave triplets wind speed u_{10} , significant wave height h , and wave period T_p are the most basic parameters to quantify wind waves. While the reference wind speed u_{10} in this thesis was provided by Dr. Maximilian Bopp, the significant wave height and the wave period were determined using the ISG slope data.

4.1.1 Significant wave height

A common method to derive elevation values from slope images is by using a shape from shading algorithm. Scherr (2017) compared different implementations of depth reconstruction from gradient based images. The surface reconstruction algorithm used in this thesis is the Frankot and Chellappa algorithm (Frankot and Chellappa, 1988). It uses the integrability condition

$$z_{xy} = z_{yx} \quad (4.1)$$

where z denotes the surface, and x and y denote the spatial dimension, which in the ISG data sets is the along-wind and cross-wind direction, respectively. The functional to be minimized is given as

$$S = \iint [(z_x - p)^2 + (z_y - q)^2] dx dy \quad (4.2)$$

with the gradient field components p and q . Using the Fast Fourier Transform (FFT), this functional can be solved in the Fourier space

$$z = \mathcal{F}^{-1} \left(-i \frac{k_x \mathcal{F}(p) + k_y \mathcal{F}(q)}{k_x^2 + k_y^2} \right) \quad (4.3)$$

where k_x and k_y are the wavenumbers and \mathcal{F}^{-1} denotes the inverse Fourier transform of the Fourier transform \mathcal{F}

$$\mathcal{F}(f) = \iint f(x, y) e^{-i(k_x x + k_y y)} dx dy \quad (4.4)$$

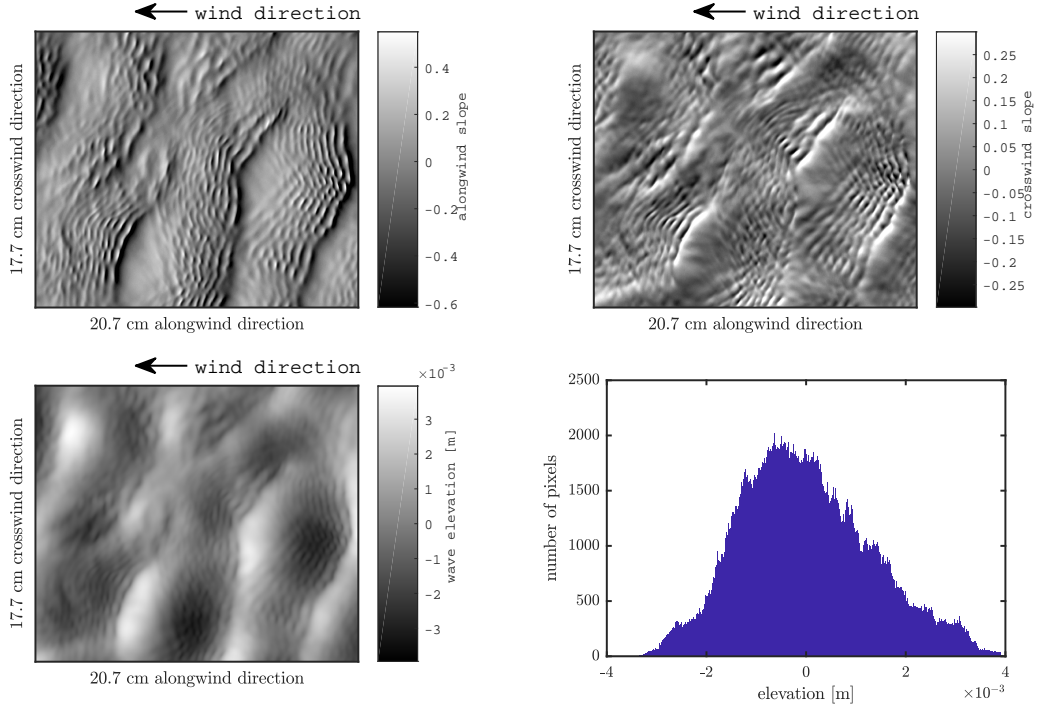


FIGURE 4.1: Slope images of the wave field (upper left: along-wind slope; upper right: cross-wind slope) and the resulting reconstruction of the surface elevation using the Frankot and Chellappa algorithm (lower left). The lower right image shows the elevation distribution for the given example image.

For the evaluation of the ISG slope data, the Frankot and Chellappa algorithm implemented for MATLAB by Xiong et al. (2015) has been used. An example of the resulting elevation of the wave field can be seen in figure 4.1.

The significant height h has been derived from the standard deviation $\sigma(\eta)$ of all elevation values η of the pixels of each data set following equation

$$h = 4\sigma(\eta). \quad (4.5)$$

The reconstructed elevation data have also been used for the 3-D surface images of this thesis (see for example figure 4.2).

4.1.2 Wave phase velocity

The mean phase velocity c_p of the dominant gravity wave of each data set was determined by using the Standard Hough Transform of a space-time image slice of the data. A line, utilizing the *houghlines* function of MATLAB, is then parameterized as

$$\rho = x \cos(\theta) + y \sin(\theta) \quad (4.6)$$

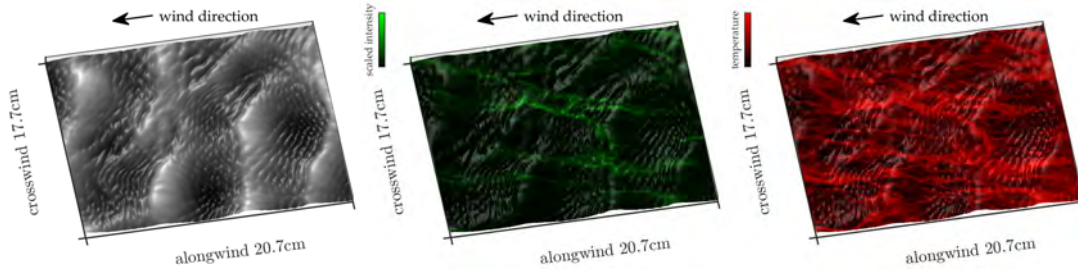


FIGURE 4.2: Surface reconstruction of the wave elevation for a mapping of the boundary layer structures as observed with BLI and AT. (left) Surface elevation with additional lighting condition to emphasize the visible structures. (middle) Surface elevation with lighting overlaid with the BLI structures. (right) Surface elevation with additional lighting overlaid with the temperature structure of the AT measurement technique.

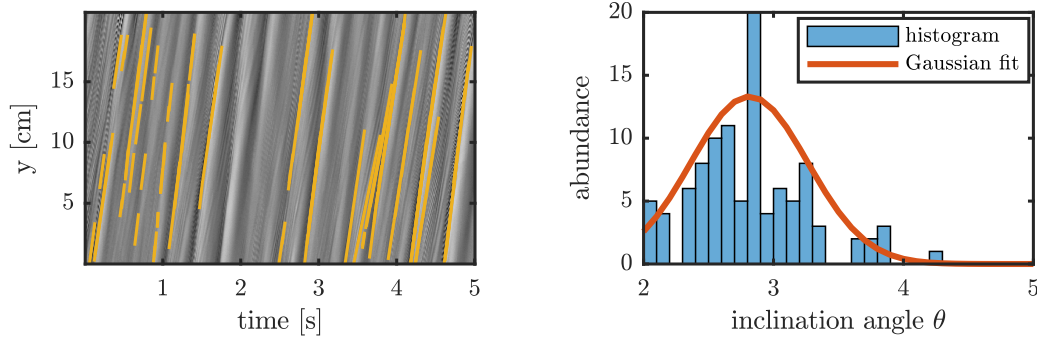


FIGURE 4.3: (left) Space time image of the along-wind slopes. The lines detected in the image are depicted in yellow. Their inclination represents the velocity. (right) Histogram of the inclination angles detected in the left figure and a Gaussian distribution fit.

with ρ as the distance from the origin of the image and θ as the inclination angle. The dominant wave phase velocity c_p can be calculated by fitting a Gaussian distribution

$$f(x) = \frac{1}{\sigma\sqrt{2\pi}} e^{-\frac{(x-\mu)^2}{2\sigma^2}} \quad (4.7)$$

to the inclination angle θ (see figure 4.3). Using the mean μ of the distribution and the size of the projected pixel 0.23 mm, the velocity is then

$$c_p = \frac{0.23 \text{ mm}}{\tan \theta} \quad (4.8)$$

The error was then determined using the standard deviation of the angle distribution. Shorter lines were more often affected by outliers, wrong line detections caused by the parasitic capillary waves. Therefore, a weighting term was added to the abundance that penalized shorter line length θ angles. For long fetches and high wind exist more parasitic capillary waves that caused wrong velocity detections, causing a wrong mean velocity. For these data sets, the dominant velocity of the gravity waves was determined using a multiple Gaussian fit distribution (see figure 4.4).

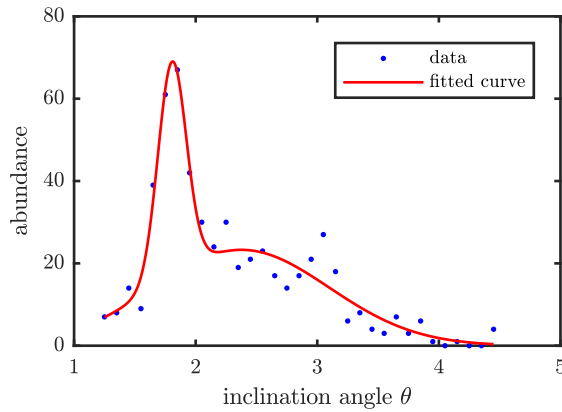


FIGURE 4.4: Adapted fit routine for data sets with many parasitic capillary waves influencing the Hough line detection.

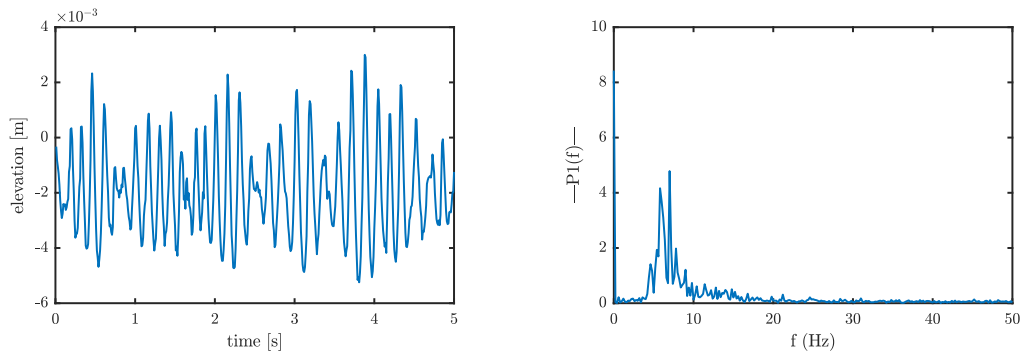


FIGURE 4.5: (left) Wave elevation of a single pixel in the xy -frame over time. The example image shows just a time of 5 seconds. A whole data set of a FE measurement condition covers 75 seconds. (right) FFT spectrum of the signal with its corresponding peak frequency.

Since the Aeolotron is an annular wind wave facility, it exhibits an underlying current, the bulk water velocity c_b . The wave phase velocity needs to be corrected for this wind speed dependent offset, leading to equation 4.9.

$$c_p = \frac{0.23 \text{ mm}}{\tan \theta} - c_b \quad (4.9)$$

4.1.3 Wave period and wavelength

The wave period t was determined using the FFT implemented in MATLAB on a signal of a pixel fixed in x and y over time of the height reconstructed images (see figure 4.5).

The dominant wavelength λ could then be determined using the mean wave phase velocity c_p and the wave period t as

$$\lambda = c_p t. \quad (4.10)$$

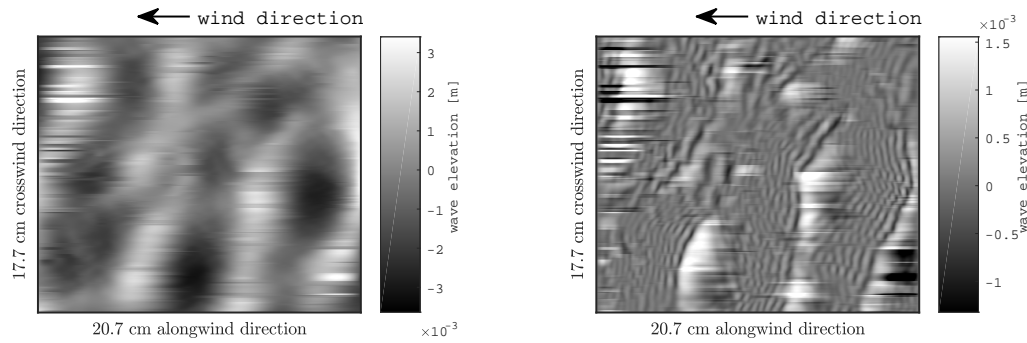


FIGURE 4.6: Separation of the gravity wave signal from the capillary wave signal using empirical mode decomposition. (left) Gravity wave contribution to the wave elevation signal. (right) Capillary wave contribution to the wave elevation signal. The wave crest of the gravity waves are still slightly visible. This may be due to the bulge formation. The thin lines of sometimes too large and sometimes too low elevation are artifacts of the algorithm, when the algorithm did not work properly.

The error of the wavelength was then determined using Gaussian error propagation. This approach to the wavelength determination was more accurate than the determination from the xy-images, since a detection from xy-images is restricted to wavelengths smaller than the along-wind image length of 20.7 cm.

4.1.4 Parasitic capillary waves

The determination of the predominant wavelength of the parasitic capillary waves has been determined using the following steps.

First, the slope values of the ISG images has been separated into gravity and capillary contribution by using the empirical mode decomposition algorithm (see figure 4.6).

Second, the parasitic contribution signal was split up at the position of the zero crossing of the gravity wave slopes (see figure 4.7).

Third, since the parasitic capillary waves are not a continuous repeating signal, instead of a Fourier transform the peaks of the capillary slopes signal were used to determine the spatial length of the capillary waves (see figure 4.8).

4.2 Microscale wave breaking

Microscale wave breaking (MB), small breaking events of the waves without bubble entrapment Banner and Phillips (1974) are known to cause a local renewal of the boundary layer with the well mixed bulk water. This mechanism is thought to be the main driving mechanism of local heat and gas transfer for low to moderate wind speeds (Siddiqui et al., 2004; Siddiqui and Loewen, 2007). In this chapter the initial

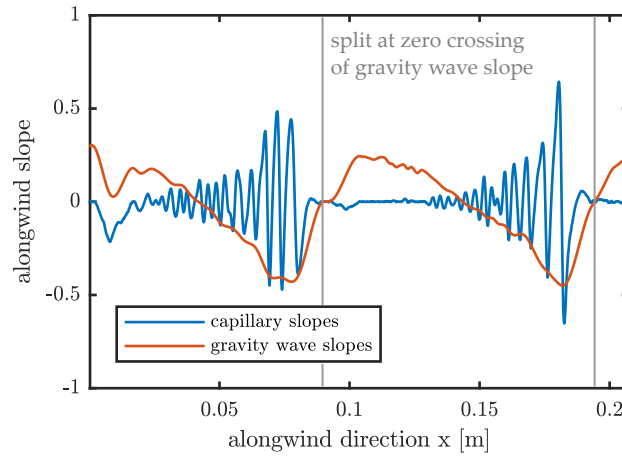


FIGURE 4.7: Split up slope contribution for the parasitic capillary waves and the gravity waves. The zero crossing of the gravity wave is used to split up the parasitic capillary signal into individual gravity wave related parts.

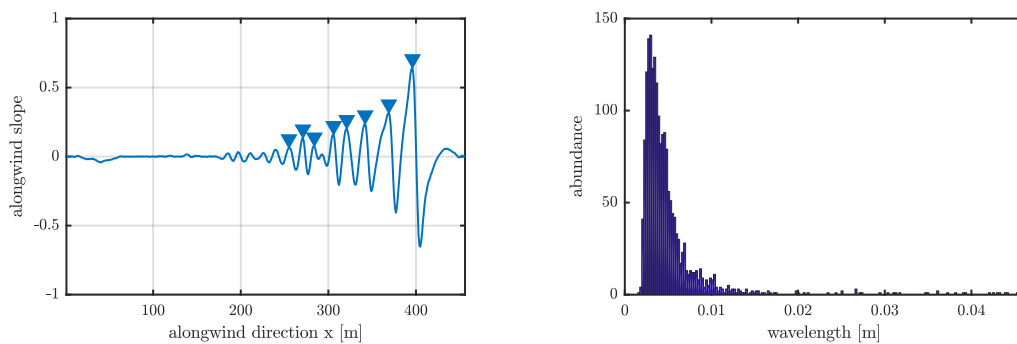


FIGURE 4.8: (left) Peak detection in the parasitic capillary slopes of a single gravity wave. (right) Example distribution of the detected capillary wavelengths.

disturbance of microscale breaking will be investigated with respect to the water sided mass boundary layer and statistical evaluations of MB of the FE.

4.2.1 Detection threshold of microscale breaking

The general formulation of microscale wave breaking describes it as a wave breaking without bubble entrapment that is accompanied by parasitic capillary waves and leaves turbulent vortices in its wake. In laboratory measurements it was observed that incident to a microscale wave breaking event occurs a toe formation at the wave crest. Evaluating the data sets of the fetch experiment made it necessary to even more specify the description of microscale wave breaking, since sometimes very small disturbances occurred which were ambiguous if they fall into the above vague definition of microscale breaking. Therefore to provide a clear definition of microscale breaking, the initial disturbance causing the turbulence in the wake of the microscale breaker was chosen to be a curvature radius c_r of the water surface that is smaller or equally large as the mass boundary layer thickness d . The reason for choosing the mass boundary layer thickness, and not the viscous boundary layer thickness, will be given in section 5.4.1.

$$c_{r,MB} \lesssim d \quad (4.11)$$

The image area in the combined BLI-IR-ISG that fulfills equation 4.11 will be referred to as the microscale breaking seeding (MBS) area. It is the position at the wave crest that initiates the microscale breaking while the impact of the seeding, i.e. the turbulent surface renewal following up in the wake of the seeding, might be dependent on more parameters than simply the seeding area.

The BLI data sets cannot provide a sufficient calibration of the measured fluorescent intensities to boundary layer thickness values. Therefore, a second seeding detection method was implemented utilizing only the curvature radii of the ISG slope data of the water surface. As seeding curvature radius threshold a typical mean thickness of the mass boundary layer as derived from gas and heat transfer measurements was selected.

$$c_{r,MB} \lesssim d_{\text{mean}} \quad (4.12)$$

4.2.2 Wave phase dependent MB

The wave phase of the gravity waves was determined using the Hilbert transform following the algorithm of Marple (1999) as implemented in MATLAB. Before applying the Hilbert transform to the height reconstructed data set, the parasitic capillaries were filtered out using empirical mode decomposition as described in Mandic et al. (2013). An example of the wave phase determination of two example wave fields is given in figure 4.9.

Thus, for each pixel of the time series of images the wave phase and the MBS condition are given (see figure 4.10).

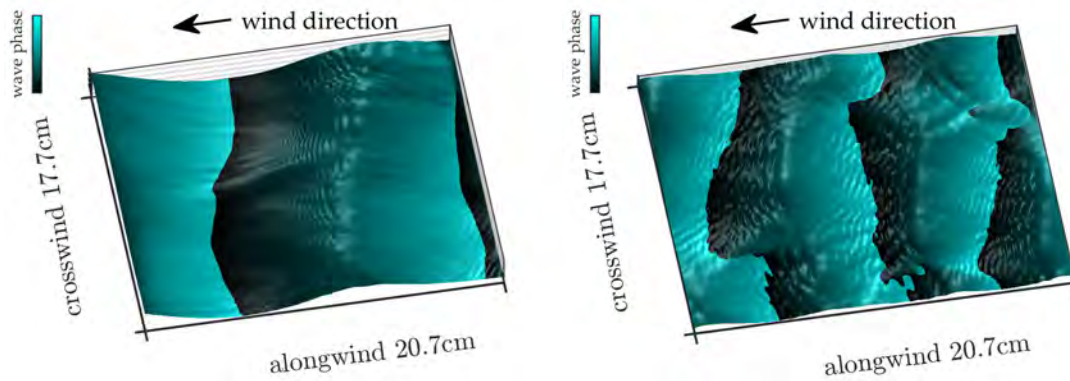


FIGURE 4.9: Surface plot of the wave elevation overlaid with the wave phase position determined with the Hilbert transform. The wave crest is the position of the zero phase. (left) Example for larger waves and (right) example for smaller waves.

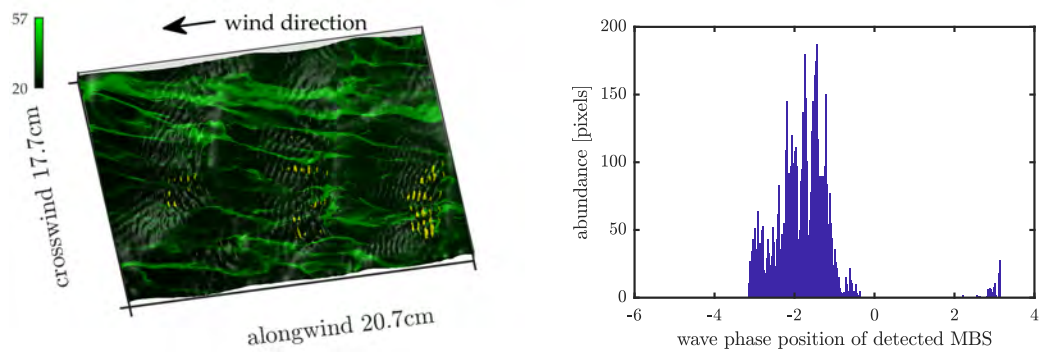


FIGURE 4.10: (left) BLI image at the same moment as the wave phase distribution of figure 4.9 and the detected MBS curvatures (in yellow). (right) Histogram of the wave phase distribution of the detected MBS pixels of the left image. Since part of the detected pixels reach into the trough of the gravity waves, some few positive phase positions are detected. For the Gaussian fit in figure 4.11 they can be shifted towards the negative side of the phase position by subtracting 2π .

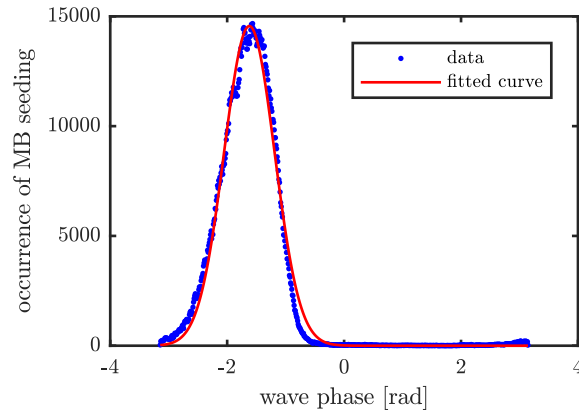


FIGURE 4.11: Gaussian fit to the distribution of the MBS detection along the wave phase of the dominant gravity wave for a time series of images of a measurement condition.

Afterwards, a Gaussian fit to the distribution of all pixel wise phase positions (as seen in figure 4.11) of MBS leads to the mean wave phase position of the initial disturbance causing MB. The error was determined as the standard deviation of the fit.

4.3 Heat transfer velocity

The heat transfer velocities were determined using the evaluation MATLAB scripts that have been implemented in Kunz (2017) and Kunz and Jähne (2018).

4.4 Boundary Layer Imaging

Since the chemical system of the BLI measurement technique is slightly changing over the course of the measurement campaign due to changes in the water bulk pH value caused by the ammonia inlet and a readjustment of the pH using HCl, it is not possible to globally calibrate the measured intensity values to thickness values. However, observations of the BLI data sets led to the conclusion, that the mass boundary layer thickness is pushed together (see section 5.4.1). This leads to the assumption that curvature radii of the water surface that are smaller than the mass boundary layer thickness can only contain their radii as respective boundary layer thickness d (see figure 4.12).

$$d(r) = \begin{cases} r - \sqrt{(r - 2d_{init})r} & \text{for } r \geq 2d_{init} \\ r & \text{for } r < 2d_{init} \end{cases} \quad (4.13)$$

Using this hypothesis based on the observations it is possible to at least qualitatively calibrate the BLI images to boundary layer thickness values. The branch of figure 4.12 that shows a linear decrease for small curvatures towards zero gives a

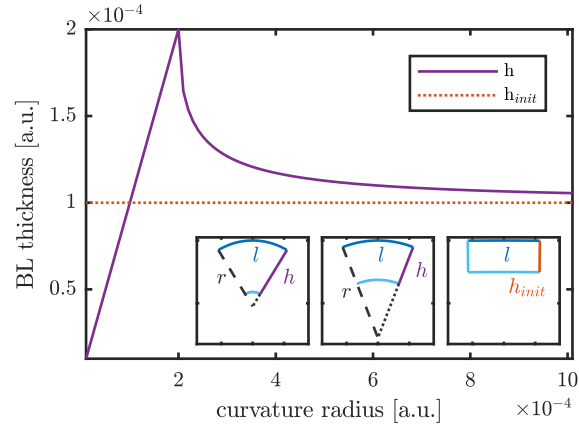


FIGURE 4.12: Theoretical thickness variation h of a boundary layer of constant thickness h_{init} under the change of the surface curvature. The surface length l of a given parcel is kept constant.

linear correlation between the boundary layer thickness and the thickness that fits into the respective curvature, yielding a calibration of the BLI data sets to qualitative mass boundary layer thicknesses.

The estimation is too imprecise and also lacks the information of the invisible area caused by the detection threshold of the method to give quantitative thickness results. However, it can be used to qualitatively visualize the thickness as has been used in figure 5.23. The indication that this accumulation might be a valid assumption is discussed in section 5.4.1.

To qualitatively calibrate the BLI data, first the curvature of the slopes as determined with the ISG needs to be determined. As long as the parasitic capillary are aligned perpendicular to the wind direction and therefore aligned with the image coordinate system, the along-wind curvature c_{xx} given as the gradient of the along-wind slopes s_x are sufficient to determine the local curvature radii. However, for waves not propagating along the predominant wind direction, the smallest principal curvature needs to be determined using the eigenvalue decomposition of the Hessian Matrix

$$H = \begin{pmatrix} c_{xx} & c_{xy} \\ c_{yx} & c_{yy} \end{pmatrix} \quad (4.14)$$

with the x and y curvatures c of each slope image (e.g. Deng et al., 2007).

Chapter 5

Results

Section 5.1 describes the observed regimes of the FE and gives an overview of the dominant mechanisms in each regime. Section 5.2 presents the measured heat and gas transfer velocities. The following sections about waves, microscale breaking, and streaks then place the respective observations into the frame of the regimes and connect fetch dependent statistics with the heat transfer velocities. Section 5.3 places the wave dependent variables such as wave steepness and wave period into the respective regimes and investigates links to the observed heat transfer velocities. Separately, a section about microscale wave breaking (section 5.4) investigates the regime dependent development of microscale breaking and gives a close insight into the cause of microscale breaking. In the end, the appearance of the streaky structures as observed with BLI and AT (see section 5.5) will be investigated.

5.1 Regimes

Figure 5.3 shows the fetch dependent heat transfer velocities. There occurs an overshoot in heat transfer velocities for finite fetch that decreases again for longer fetches. This overshoot region varies with the wind speed. This observation already indicates that there seems to be at least two different regimes captured by the FE. Together with a laminar regime for short fetches, the FE could overall be separated into three different regimes for finite fetch. The respective regimes in dependence of the wind speed are sketched in figure 5.1.

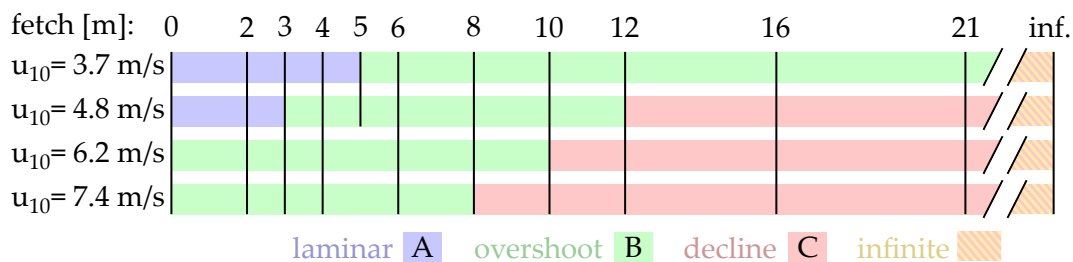


FIGURE 5.1: Regimes of the FE wind conditions in dependence on the fetch.

While for the different wind speeds, the regime change occurred at different fetches, the FE can be divided into three different fetch dependent regimes, referred to as regime A, B, and C in dependence on the Reynolds number, or alternatively in dependence on the dominant gravity wavelength, or the significant wave height, respectively (see figure 5.2). This is due to the fact that in the FE, the wave height depends linearly on the wavelength and the Reynolds number depends linearly on the wave height (see equation 2.43). While the Reynolds number Re , the gravity wavelength λ and the significant wave height h can be used to define the regimes, variables such as capillary wavelength λ_c , dimensionless transfer velocity k_+ , wave steepness η , position of MB along the wave crest MB_{pos} , and strength of MB seeding $MBS_{strength}$ show a change in their development in dependence of the regime defining variables.

- A For short fetches and $u_{10} \leq 4.8 \text{ m s}^{-1}$, the mass boundary layer is still under the influence of a laminar flow which can be seen by a homogeneous fluorescence of the mass boundary layer in the BLI images. Very thin streaky structures within this homogeneous mass boundary layer can be seen in the images, starting a few tens of milliseconds into the data set. They only occur during the combined measurements of AT and BLI and are caused by the thermography setup. This influence of the thermography setup was only present in the laminar regime, as derived from comparison measurements for different selected test data. No microscale breaking occurred for the laminar flow, and the water surface does not consist of fully formed waves yet. It is governed by wavy wiggles, or perturbances, with a significant height at or even below the detection threshold of the ISG.

- B The laminar regime is followed by a streaky regime for higher wind speeds and longer fetches with an increase in microscale breaking. This regime tends to overshoot in certain measured values such as the heat transfer velocities, the microscale breaking strength and abundance, the mean square slope (mss) and other variables.

- C The third regime, that covers the longest fetches and probably the infinite fetch data, is a regime, where the previous overshoot declines towards the infinite fetch equilibrium state. Here, the overshooting variables of the second regime, decrease again, following sometimes an individual trajectory for each wind speed u_{10} . While the fetch development of some parameters indicate that the infinite fetch belongs in regime C (e.g. heat transfer velocities), some parameters indicate that it does not (e.g. different streaky structures). Therefore, the infinite fetch case in figure 5.1 is sketched as a mixed color between regime C and an individual regime.

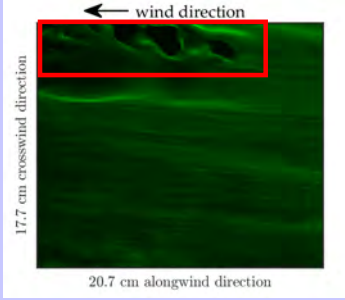
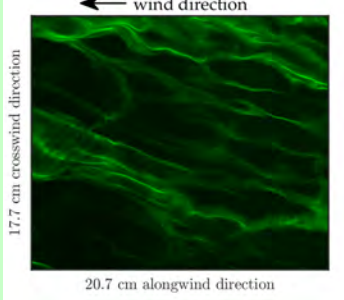
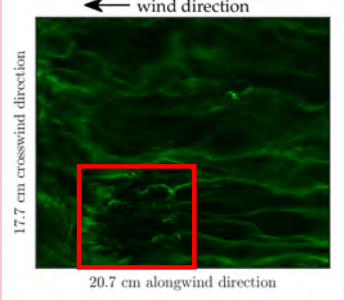
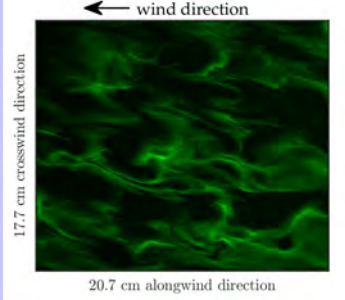
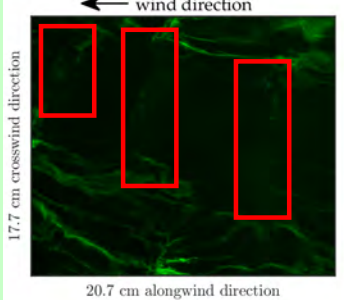
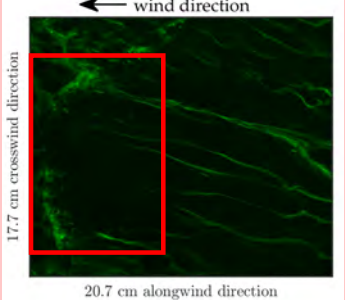
| Regime A - laminar regime | Regime B - MB build up | Regime C - MB decline |
|---|--|--|
| < 800 | $800 - 10\,000$ | $10\,000 - > 30\,000$ Re \rightarrow |
| < 4 cm | 4 cm - 13.0 cm | 13.0 cm - > 30.0 cm λ \rightarrow |
| < 0.3 cm | 0.3 cm - 1.8 cm | 1.8 cm - > 4 cm h \rightarrow |
|  <p style="text-align: center;">Surface renewal by local upwelling</p> |  <p style="text-align: center;">Surface renewal by microscale breaking</p> |  <p style="text-align: center;">Surface renewal by microscale breaking</p> |
|  <p style="text-align: center;">Upwelling smeared out by drift</p> |  <p style="text-align: center;">Often several consecutive MB events in one region</p> |  <p style="text-align: center;">Streaks quickly get broader again after surface renewal</p> |

FIGURE 5.2: Schematic overview of the fetch dependent regime classification and the regime dependent mechanisms. The red boxes show surface renewal, which is caused by local upwelling in the laminar regime (regime A), and by microscale breaking in regime B and C. This classification is only suitable for fetch limited waves and does not include the infinite fetch data. Therefore the largest wavelength, Reynolds number, and wave height of regime C are the largest values of the fetch limited FE data.

The transition from regime B to regime C, that happens at wavelengths of 13 cm is accompanied by a relatively broad gap in the respective wavelength and height range, as can be seen in figure 5.9.

The following sections will now elaborate the regime dependence of the different variables obtained by the FE.

5.2 Heat and gas transfer

5.2.1 Heat transfer velocities

The heat transfer velocity as determined using active thermography for all fetches is shown in figure 5.3. For all measured wind speeds, there occurs an overshoot for intermediate fetches. This phenomenon for heat transfer velocities has first been observed by Kunz (2017).

The measurements at fetches between 2 m and 5 m and a wind speed of $u_{10} = 7.4 \text{ m s}^{-1}$ show still laminar and shear dominated flow with no developed wave field and no microscale wave breaking. The increase in heat transfer velocities can solely be contributed to the formation of streaks and to the occurrence of local upwelling due to horseshoe vortices. However, the streaky structure observed at fetches of 5 m and 6 m show nearly the same pattern but the heat transfer velocities are deviating from each other.

The infinite fetch heat transfer velocities of both water charges are shown in figure 5.4.

5.2.2 Gas transfer, Schmidt number exponent, and scaling factor β

The gas transfer velocities, determined by mass balance methods integrating over the whole surface area of the Aeolotron, could only be determined for infinite fetch (see figure 5.5) and for the second water charge.

The chosen wind speeds were just in the range where the Schmidt number exponent varies from $n = \frac{2}{3}$ to $n = \frac{1}{2}$ (see figure 5.6).

Additionally, the wind speeds of $u_{10} \geq 7.4 \text{ m s}^{-1}$ were already in the range, where a surface film would tear open.

For the infinite fetch conditions β could be determined since all other variables were given. Figure 5.7 shows the individual values for β for each infinite fetch data set.

These values deviates significantly from the value given by Deacon (1977) of $\beta = 12.2$. However, they lie closer to the range of $\beta = 6.7$ as determined by Krall (2013), $\beta = 7.5$ as previously determined for the Aeolotron facility with different fans than the current setup has installed (Nielsen, 2004), and $\beta = 4.5$ as determined in a much smaller annular wind wave facility (Degreif, 2006).

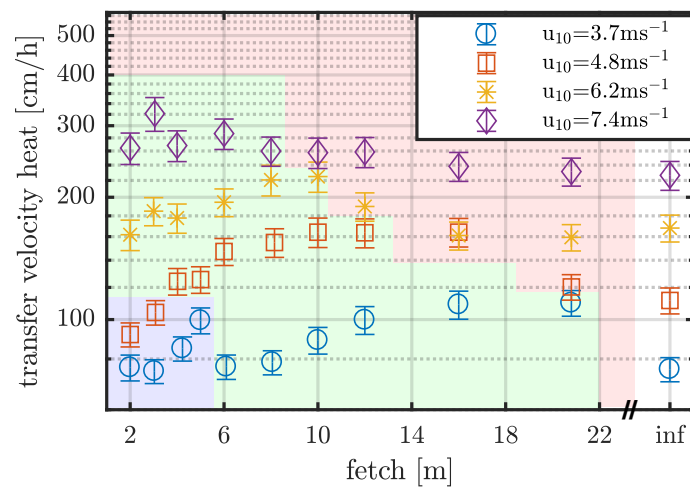


FIGURE 5.3: Heat transfer velocity k of the fetch experiment. For intermediate fetches the heat transfer velocity seems to overshoot in comparison with the infinite fetch condition. For the lowest wind speed of $u_{10} = 3.7 \text{ m s}^{-1}$ the four shortest fetches were in the laminar regime and the only surface renewal mechanism occurring was the upwelling of horseshoe vortices. Still this mechanism leads to a significant increase for the heat transfer velocity especially for a fetch of 5 m compared to the 6 m heat transfer velocity that was decreased again.

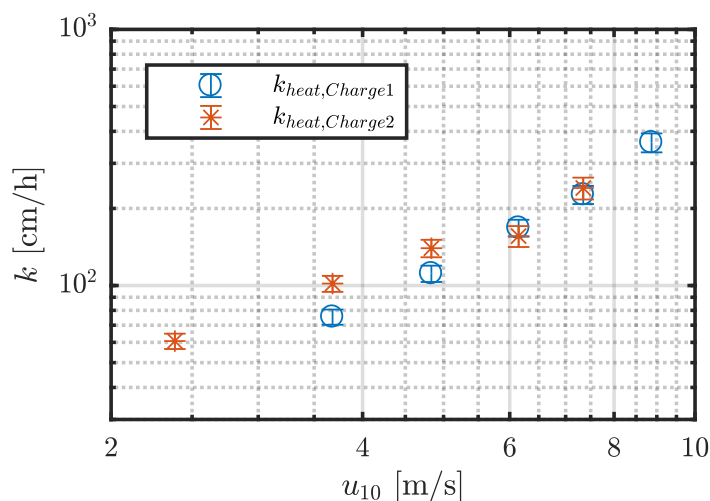


FIGURE 5.4: Infinite fetch heat transfer velocities of water charge 1 and 2. The former has also been used for the finite fetch measurements and the later were accompanied by global gas transfer velocity measurements.

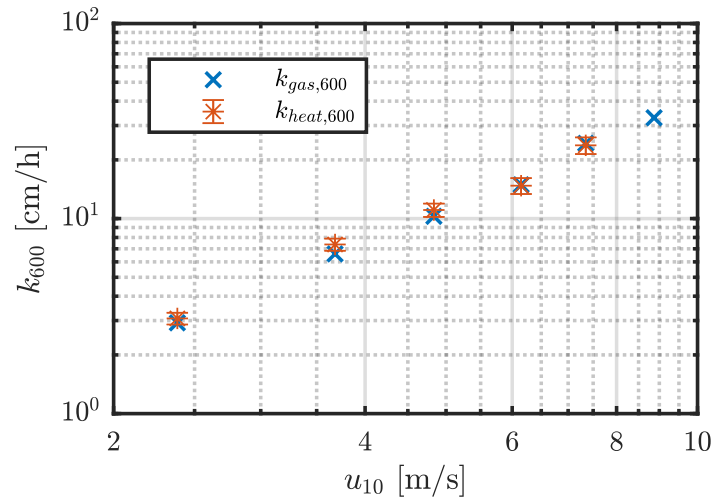


FIGURE 5.5: Global gas transfer velocities for infinite fetch scaled to a Reynolds number of 600. The blue crosses show the transfer velocities of the global gas measurements, the red circles the scaled local heat transfer velocities.

5.3 Waves

This section is about the fetch dependent development of the waves. It also investigates the wave parameters in context with the previously defined regimes and in the context of the occurrence of the different boundary layer mechanisms.

5.3.1 Significant wave height and steepness

During the FE, a linear fit could be applied to the significant wave heights in dependence of the wavelengths (see figure 5.8) given as

$$h(\lambda) = a \cdot \lambda + b. \quad (5.1)$$

The fitted variables were $a = 0.13(1)$ and $b = -0.0037(10)$ m.

According to equation 5.1, the minimum wavelength for $h = 0$ m is

$$\lambda = \frac{-b}{a} = 2.8(10) \text{ cm}. \quad (5.2)$$

This value is already in the gravity wave range ($\lambda > 1.7$ cm) where the capillary effects are not negligible yet. The shortest observed dominant gravity wavelengths of the FE were $\lambda = 3.4(4)$ cm, however, due to the chosen fetch resolution the shortest wavelengths might not be captured by the FE. The wave steepness $\eta = \frac{h}{\lambda}$, on which microscale breaking was observed was $\eta > 0.06$ which would correlate to wavelengths of $\lambda > 5.2$ cm. For longer wavelengths, the steepness converges towards

$$\eta(\lambda)_{\lambda \rightarrow \infty} = 0.1325(87) \cong \delta_{\max, \text{Stokes}} \quad (5.3)$$

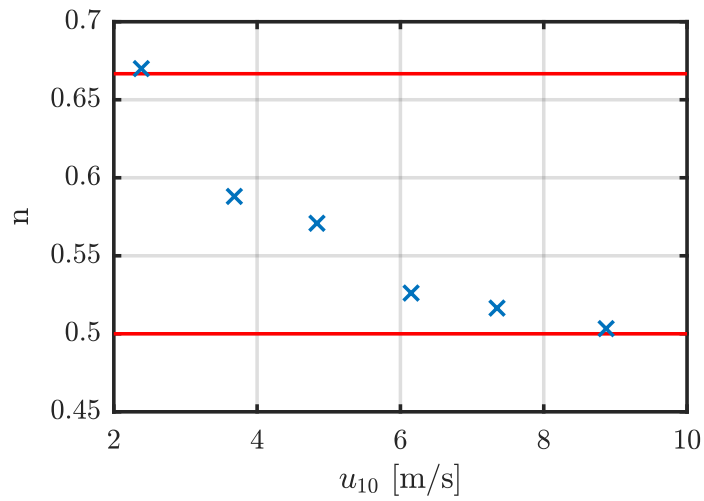


FIGURE 5.6: Schmidt number exponent for the infinite fetch data. The red bars show the limit for $n = \frac{2}{3}$ and $n = \frac{1}{2}$.

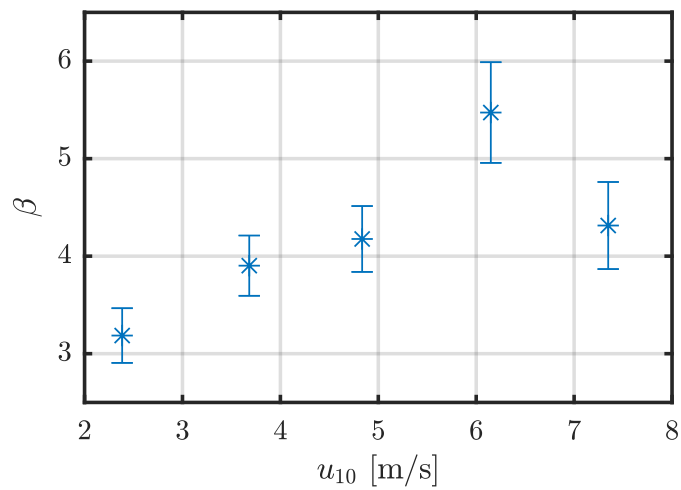


FIGURE 5.7: β determined for the infinite fetch data for water charge 2.

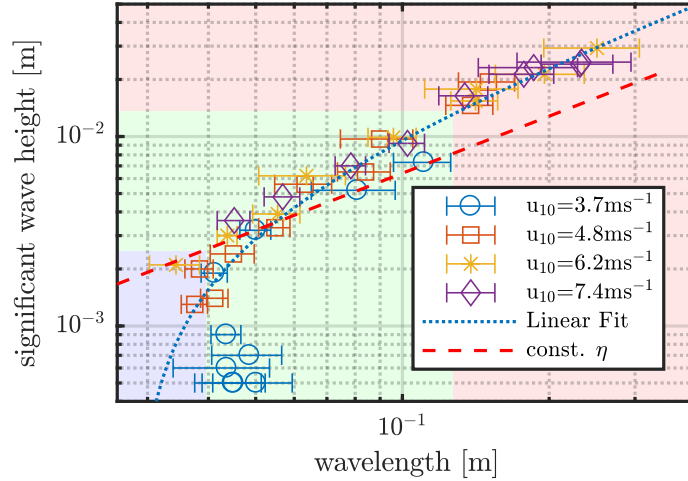


FIGURE 5.8: Significant wave height vs wavelength of the gravity wave for the finite fetch data. The dotted lines represent a linear fit to the data. The dashed line shows the line of constant steepness of $\eta = 0.06$ (which is the steepness threshold of MB as can be seen in section 5.4.4).

which is consistent with the Stokes limit of $\eta = 0.14$ (Kinsman, 1965).

According to Toba (1997) the relationship between wavelength and significant wave height is

$$h_{toba} = 0.062(gu_{*,a})^{\frac{1}{2}} \left(\frac{\lambda}{c_p} \right)^{3/2} \quad (5.4)$$

with the gravitational acceleration g , the air sided friction velocity $u_{*,a}$, the wavelength λ , and the wave phase velocity c_p . Figure 5.9 shows the significant wave heights plotted against each other. The significant wave height determined by equation 5.4 underestimates the significant wave height by

$$h_{toba} = 0.6h + 0.0016 \text{ m}. \quad (5.5)$$

Additionally, there occurs a gap for the wavelength range between 10 cm and 14 cm. That is also the wavelength range at which the regime changes occur.

5.3.2 Wave period and phase speed

The wave period in context with microscale wave breaking can be a useful parameter in investigating the surface renewal rate of the mass boundary layer in dependence of for example microscale wave breaking.

Figure 5.10 shows the wave period T_s plotted against the fetch for the different wind speeds. Only for $u_{10} = 7.4 \text{ ms}^{-1}$ is the wave period in the range of the heat transfer velocity time constant t_k . The wave phase velocity in dependence on the dominant gravity wavelength is shown in figure 5.11. Only for larger

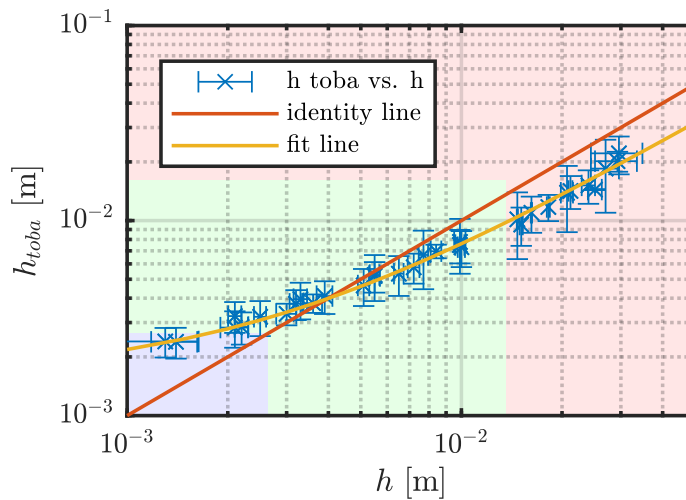


FIGURE 5.9: Significant wave height determined using equation 5.4 plotted against the significant wave height of the FE data. The significant wave height of Toba (1997) underestimates the measured significant wave height for $h > 0.005$ m. Also, there occurs a gap for wavelengths between 10 cm and 14 cm which is also the wavelength range at which the regime change occurs. The red line represents the identity line and the yellow line shows the fit of equation 5.5.

wavelengths comes the phase velocity in the range of the theoretical phase speed of the dispersion relation. The measured phase velocities for smaller wavelengths are larger than the theoretical values. This deviation might be caused for measurements of short fetches and therefore close to the wave absorber by a different underlying current.

Figure 5.12 shows the wave age $\tau = c_p u_{10}^{-1}$ plotted against the fetch. Fitting equation 2.57 to the FE data, the fit yields slightly different parameters, namely $\alpha = 3.68 \times 10^4$, $\beta = -0.86$, $\gamma = -3.2 \times 10^4$, and $\delta = 0.417$. Since the parameters have been determined empirically, a slight deviation is reasonable.

The measurement conditions before the onset of MB are also the data points in figure 5.12 that deviate from the empirical equation.

5.3.3 Mean square slope

The mean square slope, mss, is a parameter that is used to determine if the wave field is already in an equilibrium state, and the moment it reaches a constant value after the wind has been turned on, the measurements can be conducted. Additionally, it can be used to quantify if a surface film is developing over time that suppresses the waves.

Figure 5.13 shows the mss in dependence on the fetch and the mss scaled with the air sided friction velocity u_* in dependence on the dominant gravity wavelength. While the mss plotted against λ show the regime change at $\lambda = 13$ cm, the values

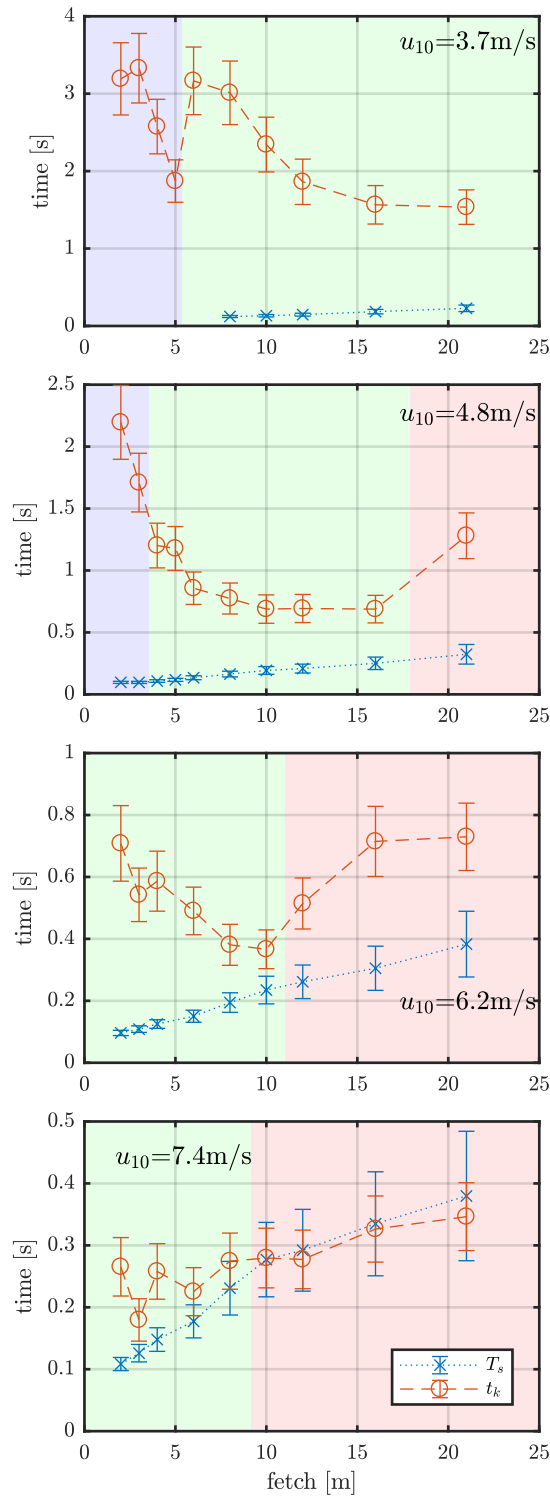


FIGURE 5.10: Fetch and wind dependent wave period T_s plotted alongside t_k , the time constant of the heat transfer velocity k . Only for the large fetches and the highest wind speed does the wave period come in the range of the time constant.

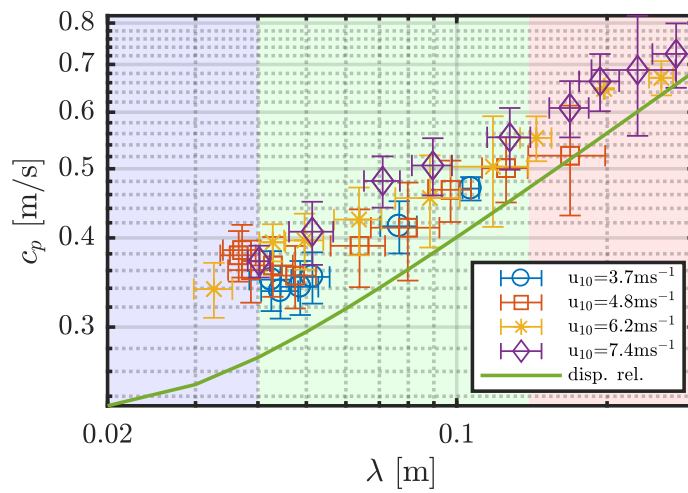


FIGURE 5.11: Wave phase velocity c_p plotted against the dominant gravity wavelength λ . The green line shows the gravity-capillary dispersion relation. The shortest measured phase velocities were larger than the theoretical value.

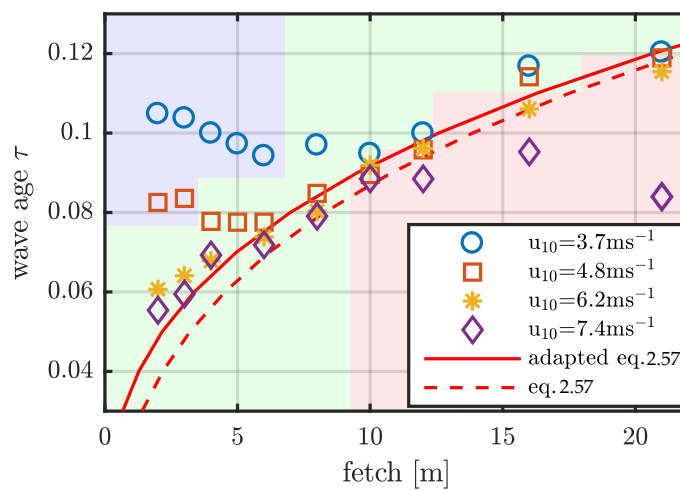


FIGURE 5.12: The wave age vs fetch plot shows a significant deviation from (Donelan et al., 1992) for soft wind and short fetches.

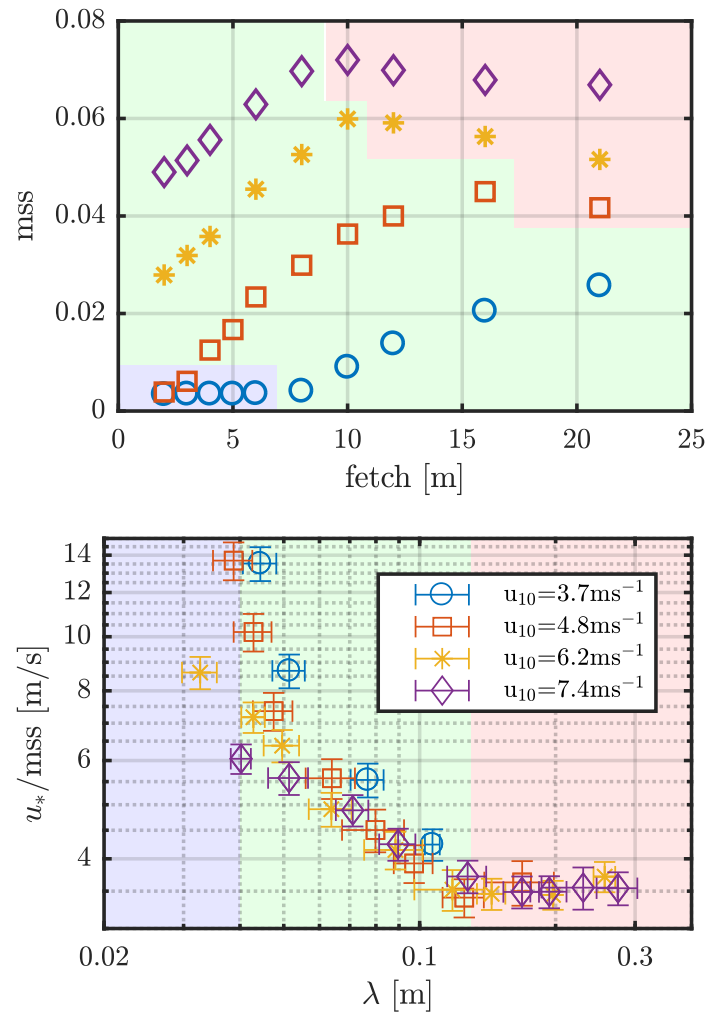


FIGURE 5.13: (upper) Fetch dependent development of the mss. The regime change from B, with an increasing mss, to C correlates with a starting decrease in the mss. (lower) Air sided friction velocity divided by the mss. Here, the regime change starts for $u_{*,a}/\text{mss} = 3.5 \text{ m s}^{-1}$.

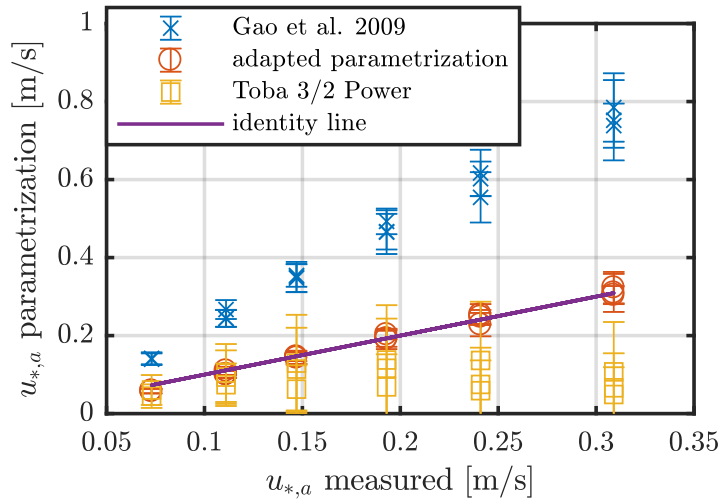


FIGURE 5.14: Adaption of the parametrization by Gao et al. (2009) for the local friction velocity by using the infinite fetch data set friction velocities as a calibration. The parametrization by Toba (1997) seems to be only suitable for small $u_{*,a}$.

still deviated by a certain offset for each wind speed. However, dividing the friction velocity by the mss leads to a stagnant value with respect to the wavelengths λ . Here, the regime change starts for

$$\frac{u_*}{\text{mss}} \geq 3.5 \text{ m s}^{-1}. \quad (5.6)$$

5.3.4 Friction velocity

While it is a good approximation to assume the air sided friction velocity is nearly constant over the different fetches (Schwenk, 2019), applying the parametrization of the friction velocity by Gao et al. (2009) or Toba (1997) might lead to some variation of the parameterized friction velocity along the fetches.

The parametrization by Gao et al. (2009) does fit the measured friction velocities $u_{*,a,\text{meas}}$ for infinite fetch apart from a fit constant

$$u_{*,a,\text{Gao}} = 2.43(6)u_{*,a,\text{meas}}. \quad (5.7)$$

Therefore for this thesis the parametrization was adapted to

$$u_{*,a} = \beta_g u_{10}^{\frac{4}{3}} c_p^{-\frac{1}{3}}. \quad (5.8)$$

with $\beta_g = 0.015$. Figure 5.14 shows the two parametrizations plotted against the measured friction velocities. Utilizing this parametrization, there seems to occur an overshoot in the friction velocities that moves towards shorter fetches for increasing wind speed (see figure 5.15).

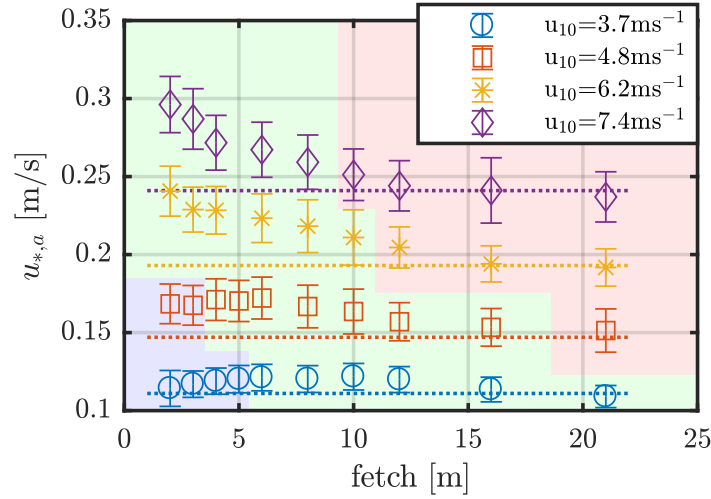


FIGURE 5.15: Fetch dependent parameterized air sided friction velocity for the FE. The dotted lines show the friction velocities measured at infinite fetch.

The adapted parametrization was also applied to the wind duration limited data of Schwenk (2019) and lead to comparable friction velocities (see figure 5.16). To apply the adapted parametrization, first, the wave phase velocity needed to be estimated by using the parametrization

$$c_p = \left(\frac{g(h-b)}{2\pi a} \right)^{\frac{1}{2}} \quad (5.9)$$

derived from the linear dependence of the wave height h on the wavelength λ and the dispersion relation for deep water waves, since only the significant height of the data was given besides the friction velocities. The complete parametrization that lead to the solid lines in figure 5.16 is

$$u_{*,w} = u_{*,a} \left(\frac{\rho_a}{\rho_w} \right)^{\frac{1}{2}} \beta_g u_{10}^{\frac{4}{3}} \left(\frac{g(h-b)}{2\pi a} \right)^{-\frac{1}{6}}. \quad (5.10)$$

However, in both the fetch and the duration limited case, the friction velocity was in an approximation nearly the same as for the infinite fetches.

5.3.5 Dimensionless transfer velocity utilizing the friction velocity

For a given friction velocity u_* , and gas transfer velocity k , the fetch and wind speed dependent dimensionless transfer velocity k_+ can be determined as

$$k_+ = \frac{k}{u_{*,w}} = \sqrt{\frac{\rho_w}{\rho_a}} \frac{k}{u_{*,a}} = \frac{\text{Sc}^{-n}}{\beta} \quad (5.11)$$

With respect to the regime division by wavelength, height, or Reynolds number,

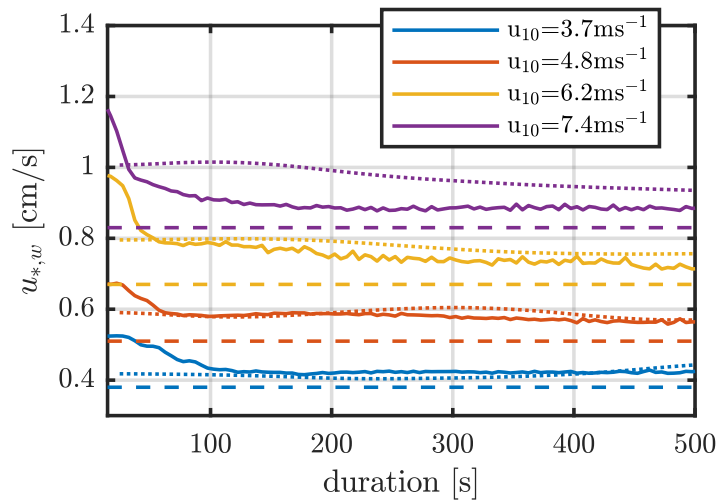


FIGURE 5.16: Duration limited friction velocities as determined by the (solid line) adapted parametrization of Gao et al. (2009), (dotted line) direct measurements of Schwenk (2019), and (dashed line) global infinite fetch measurements.

respectively, the dimensionless transfer velocity of the FE can be plotted as in figure 5.17. While for $\lambda < 13$ cm, or $h < 1.2$ cm, or $Re < 10\,000$, respectively, the dimensionless transfer velocity seems to follow a single trajectory, for larger wavelengths, heights, and Reynolds numbers this trajectory splits up.

5.3.6 Reynolds number

Reynolds number

The regimes of section 5.1 can be plotted against the wavelength λ , the height h , or the Reynolds number Re , respectively. However, it should be noted that while the height seems to correlate linearly with the wavelength, the Reynolds number can therefore not correlate linearly with the wavelength. Rearranging the wave phase velocity c_p (see equation 2.37) to λ and applying the fit equation for the wave height (see equation 5.1) and rearranging it to λ too, equation 2.43 yields

$$Re = \frac{1}{\nu} \left(\frac{g\lambda}{2\pi} \right)^{\frac{1}{2}} (a\lambda + b). \quad (5.12)$$

The Reynolds number in dependence on the wavelength can be seen in figure 5.18. The small deviations can be caused by a slightly different bulk velocity of the water for finite fetches compared to infinite fetches, which would cause a slight underestimation of the wavelengths.

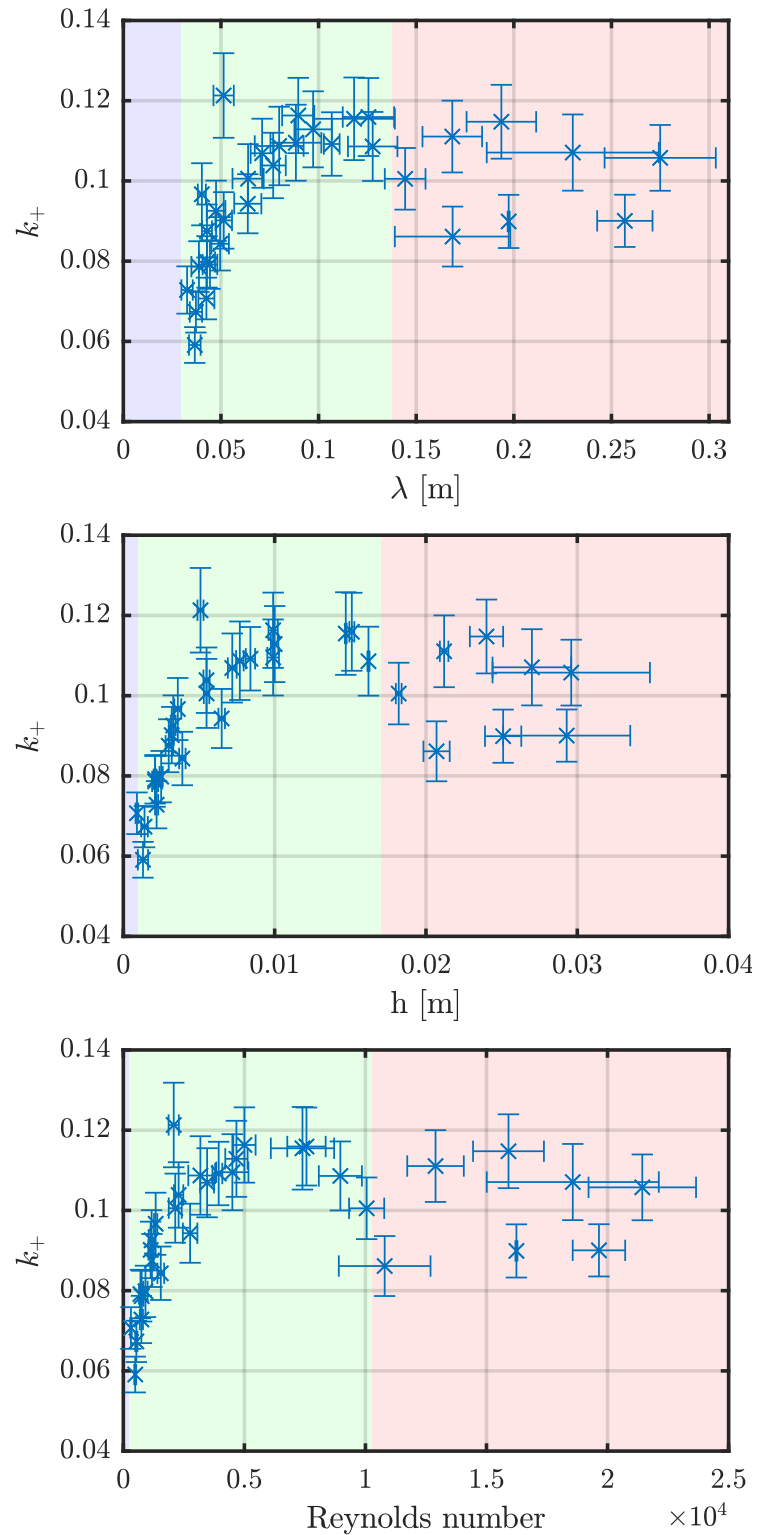


FIGURE 5.17: Fetch dependent dimensionless transfer velocity k_+ plotted against the regime defining variables λ , h , and Re. For regime B, the dimensionless transfer velocity follows a single trajectory that then splits up in regime C.

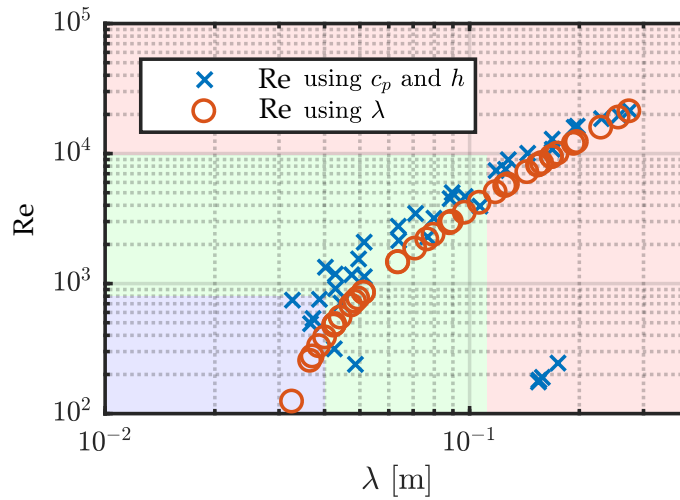


FIGURE 5.18: Reynolds number Re plotted against the wavelength. The blue crosses represent Re determined using the significant wave height h and the dominant phase velocity c_p . The red circles represent Re determined using equation 5.12. Small Re with large wavelengths are a measurement artifact, since no waves were present yet.

Windsea Reynolds number

Rearranging the gas transfer velocity equation to the air sided friction velocity $u_{*,a}$ yields

$$k = \frac{1}{\beta} u_{*,a} \left(\frac{\rho_a}{\rho_w} \right)^{\frac{1}{2}} Sc^{-n}. \quad (5.13)$$

Rearranging to the friction velocity leads to

$$u_{*,a} = \beta \left(\frac{\rho_w}{\rho_a} \right)^{\frac{1}{2}} k Sc^n. \quad (5.14)$$

Inserting the transfer velocity time constant t_k given as

$$t_k = \frac{D}{k^2}, \quad (5.15)$$

the windsea Reynolds number can be rewritten as

$$Re_b = \frac{t_s}{t_k} \left(Sc^{2n-1} \beta^2 \frac{\rho_w}{\rho_a} \right). \quad (5.16)$$

The windsea Reynolds number plotted against the ratio $\frac{t_s}{t_k}$ is shown in figure 5.19. For $Re_b > 1500$ the ratio $\frac{t_s}{t_k}$ gets larger than 1. This case is only given for a few data of the FE.

Roughness Reynolds number

Since the mean square slope is a parameter to describe the roughness of the water surface, the roughness Reynolds number was adapted to incorporate the mss by

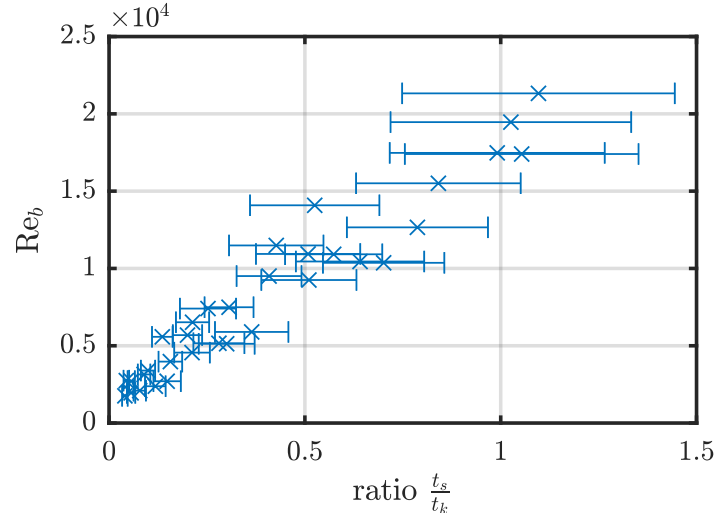


FIGURE 5.19: Windsea Reynolds number determined using the friction velocity parametrization of Gao et al. (2009) plotted against the ratio of the wave period t_s and the transfer velocity time constant t_k .

defining a mss dependent roughness parameter

$$z_{0,\text{mss}} = \text{mss} \Delta x \quad (5.17)$$

with $\Delta x = 0.00023$ m as the resolution of the ISG data that have been used to determine the mss. This yields an adapted roughness Reynolds number of

$$\text{Re}_{0,\text{mss}} = \frac{u_* z_{0,\text{mss}}}{\nu} = \frac{u_* \cdot \text{mss} \cdot 0.00023 \text{ m}}{\nu}. \quad (5.18)$$

The adapted roughness Reynolds number seems to correlate with the fetch dependent heat transfer velocities (see figure 5.20). The fit in figure 5.20 is given as

$$k \left[\text{cm h}^{-1} \right] = 54.5 \text{ cm h}^{-1} \cdot \text{Re}_{0,\text{mss}} + 84.6 \text{ cm h}^{-1}. \quad (5.19)$$

Parasitic capillaries

The parasitic capillary waves are a necessary contribution to the microscale breaking mechanism without which microscale breaking has yet not been observed. Therefore it is of importance to look into the capillary related variables of the FE. Figure 5.21 shows the dominant parasitic capillary wavelength λ_c plotted against the dominant gravity wavelength. In accordance with the previously defined regimes, there occurs a change in the trend of the parasitic capillary wavelength for a gravity wavelength of $\lambda = 13$ cm.

The longest parasitic capillary wavelength was shorter than 1 cm, which agrees with the observations by Zhang (1995).

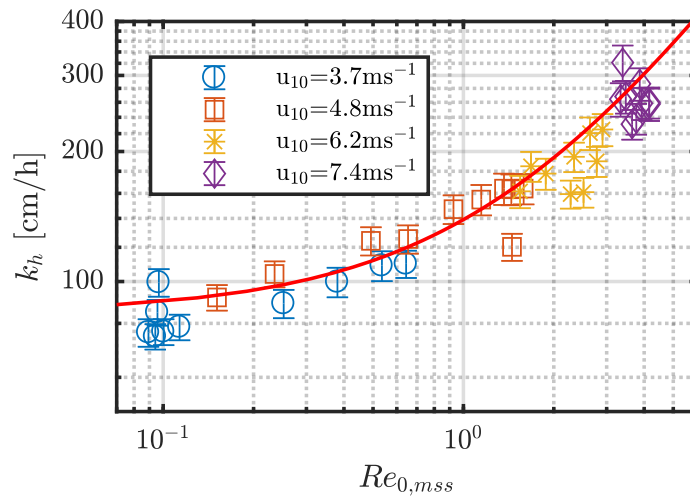


FIGURE 5.20: Fetch dependent heat transfer velocity plotted against the adapted roughness Reynolds number. The red line shows a linear fit to the data given in equation ??.

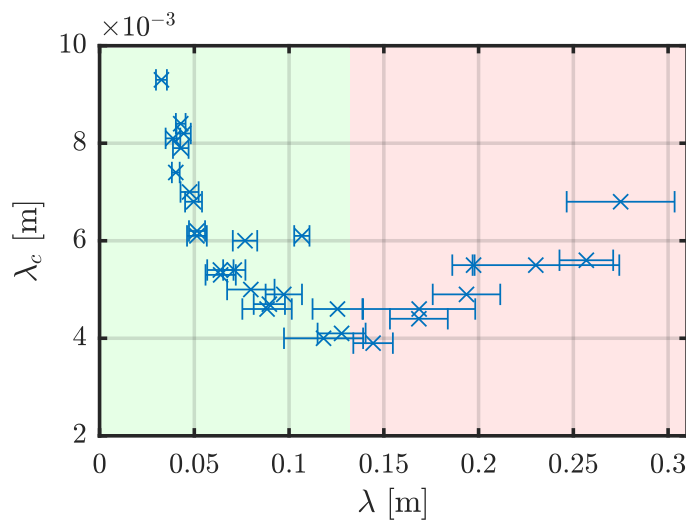


FIGURE 5.21: Dominant parasitic capillary wavelength plotted against the dominant gravity wavelength. In agreement with the regime division, there occurs a change in the trend for $\lambda = 13$ cm.

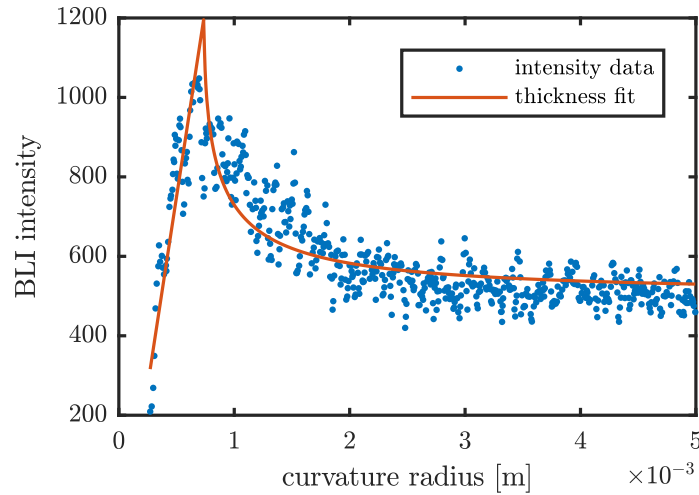


FIGURE 5.22: Intensities in dependence on the curvature radius and a fit of the theoretical dependence for the assumption of a curvature dependent accumulation of the mass boundary layer thickness. The observation seems to agree with the proposed boundary layer thickness accumulation in the parasitic capillary waves.

5.4 Microscale wave breaking

5.4.1 Dynamics of an MB event

Imminent to a microscale breaking event there occurs an accumulation of the mass boundary layer thickness in the parasitic capillary waves leewards of the wave crest toe formation. This accumulated boundary layer thickness is then released in the typically observed high vorticity wake of the MB wave.

Figure 5.22 shows a fit using equation 4.13 of the intensity variation due to the curvature to intensity values observed for microscale breaking at a single wind speed condition. Not only from the direct observations of the BLI data, also the fit indicates, that there occurs an accumulation of the mass boundary layer in the highly curved regions of the parasitic capillary waves.

The temporal evolution of such an event, which will be referred to as microscale breaking seeding event (MBS), can be seen in figure 5.23. The time increment of each plotted boundary layer thickness from top to bottom is 0.01 s. The plot shows the parasitic capillary waves lee side of the wave crest including the wave crest itself. Each time step, more mass boundary layer thickness is accumulated in the first lee side parasitic capillary waves until (marked with *MB seeding*) the accumulated mass boundary layer thickness is quickly released into the wake of the wave. The accumulation occurs lee side of the highly curved trough at the bulge formation.

The FE provides a first insight in the accumulation of the mass boundary layer thickness previous to an MB event leeward of the troughs of the parasitic capillary waves and the toe/bulge. This experimental observation can only be seen in the

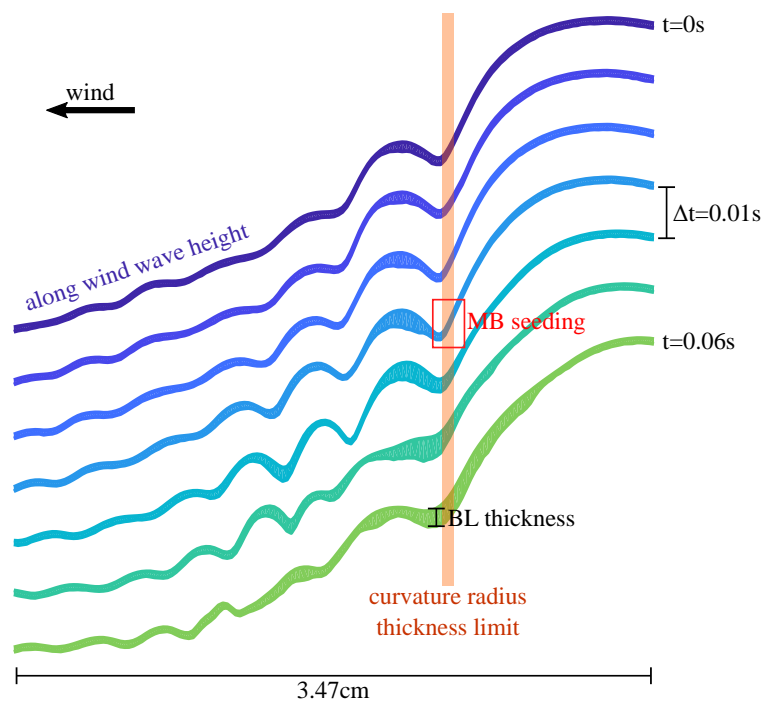


FIGURE 5.23: Change in mass boundary layer thickness due to the change in the curvature radius of the water surface. Each time step is represented by a different color, respectively. For times $t = 0$ s to $t = 0.03$ s there occurs an accumulation of the mass boundary layer thickness in the parasitic capillary wave adjacent to the wave crest caused by the curvature radius thickness limit. The build up of hydrostatic pressure then causes the microscale breaking seeding marked inside the rectangle and the break up of the small curvature radius region at the wave crest.

BLI data sets and not in the AT data sets, since an accumulation of a boundary layer thickness with a certain temperature still provides the same temperature as before.

Estimation of a simple velocity model

The model estimation for the velocity barrier of the MB seeding is calculated in the reference frame of the wave crest. The initial velocity of the BL was chosen as the drift velocity c_d of the BL in the trough of the data set. The initial thickness d_t was also taken from a qualitative thickness calibration of the BLI images in the wave trough. For the variation of the velocity along the parasitic capillary waves and the wave crest, the change in velocity u_1 was modeled as being solely due to the change in BL thickness d , following the equation of the volumetric flow of an incompressible fluid

$$u_1 d_m = u_{\text{init}} d_t = (c_p - c_d) d_t. \quad (5.20)$$

The solid line of figure 5.24 is calculated as

$$u_1 = (c_p - c_d) \frac{d_t}{d_m} \quad (5.21)$$

with the wave phase speed c_p , the drift velocity of the mass boundary layer in the trough of the wave c_d , the thickness of the mass boundary layer in the trough d_t , and the modeled thickness d_m caused by the curvature variation utilizing equation 4.13. The dotted line in figure 5.24 is calculated as the velocity u_2 due to the hydrostatic pressure given as

$$\frac{1}{2} u_2^2 = \frac{\Delta u}{\Delta t} s \quad (5.22)$$

$$u_2 = \sqrt{2 \frac{\Delta u}{\Delta t} s} \quad (5.23)$$

with s as the width of the boundary layer thickness accumulation area along the wave crest and $\frac{\Delta u}{\Delta t}$ is the pixel wise acceleration of the boundary layer due to the volumetric flow in the curvatures of the parasitic capillaries.

The time stamps in figure 5.24 are the same as in figure 5.23. It can be seen, that for $t = 0.03$ s, the moment of the MBS, u_2 briefly exceeds u_1 . However, the presented model is just a first approach toward the understanding of the cause of MBS, and the influence of e.g. gravity and variations of the velocity in the boundary layer along the z-axis have been neglected.

Toe cascading

The FE also gave insight, that the larger MB events are caused by a cascading of the initial disturbance lee side of the wave crest. In the instant where the initial disturbance causes MB, the toe/bulge becomes a ripple disturbance propagating towards the parasitic capillaries further down the wave crest and initiating secondary toe

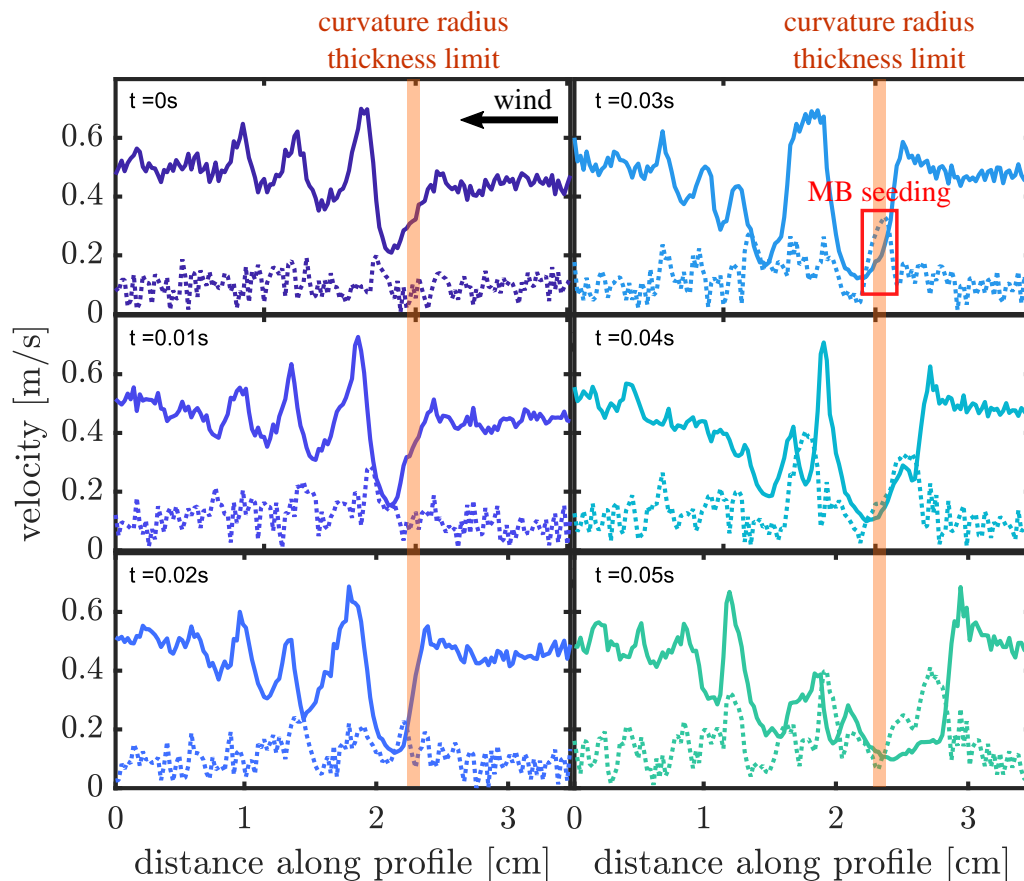


FIGURE 5.24: Estimation of the velocity components counteracting in the trough of the parasitic capillary waves of the wave crest and possibly causing the initiation of the microscale breaking. The solid line represents the model maximum velocity for a volumetric flow, with the volume fluctuation given by the curvature fluctuation. The dotted line represents the velocity determined using equation 5.22.

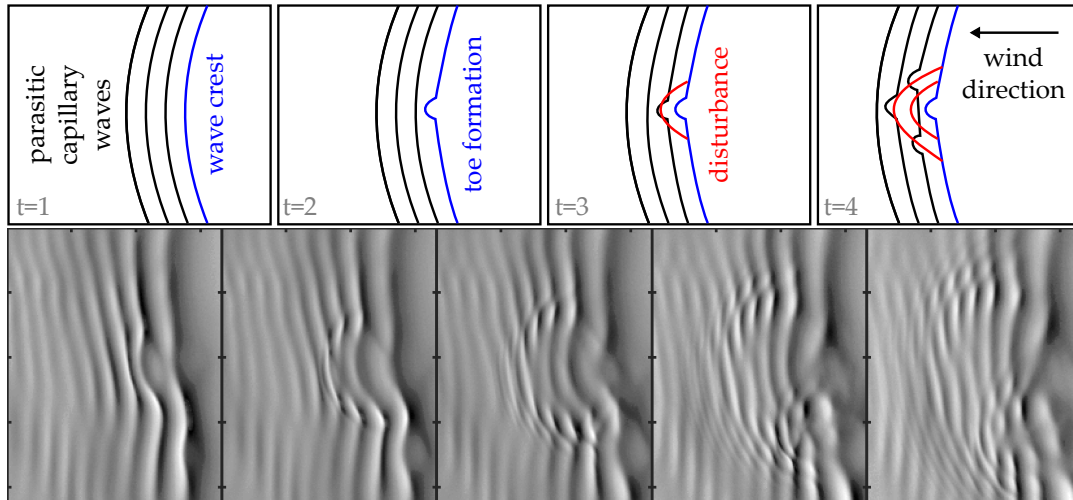


FIGURE 5.25: (top) Toe cascading leading to a larger MB event. The initial disturbance caused by the first toe at the wave crest causes a disturbance, seen as small capillary ripples, that propagate the lee side of the gravity wave and initiates secondary toes at the other parasitic capillary waves. (bottom) Example image time series of a toe cascading event as seen by the along-wind slope images of the ISG.

formations that cause MB. This event can also be described as toe cascading. An example of such a toe cascading is shown in figure 5.25.

5.4.2 Wind and fetch dependent occurrence of microscale breaking

While for short fetches and a wind speed smaller than 4.8 m s^{-1} there occurred no MB and the mass boundary layer was laminar, the percentage of wave crests that exhibit MB increases sharply for intermediate fetches to a rate of nearly 90% of MB wave crests. The rate decreases again towards the larger fetches of the FE (see figure 5.26).

Aside from the laminar regime, the heat transfer velocities exhibit a similar overshoot, indicating that the surface renewal of microscale wave breaking contributes to the heat transfer velocities (see figure 5.3).

The strength of MB in dependence of the dominant gravity wavelength is shown in figure 5.27. It is the percentage of pixels of the whole image that initiate MBS. It increases in regime B, for $\lambda < 13 \text{ cm}$ and decreases again for $\lambda > 13 \text{ cm}$.

5.4.3 Wave phase dependent occurrence of Microscale Breaking

The position of the initial disturbance leading to microscale wave breaking along the wave crest was determined using the algorithm developed in section 4.2.2. For the infinite fetch conditions, the disturbance occurred at the same position for each wind condition within the error range. At finite fetch conditions, the position of the

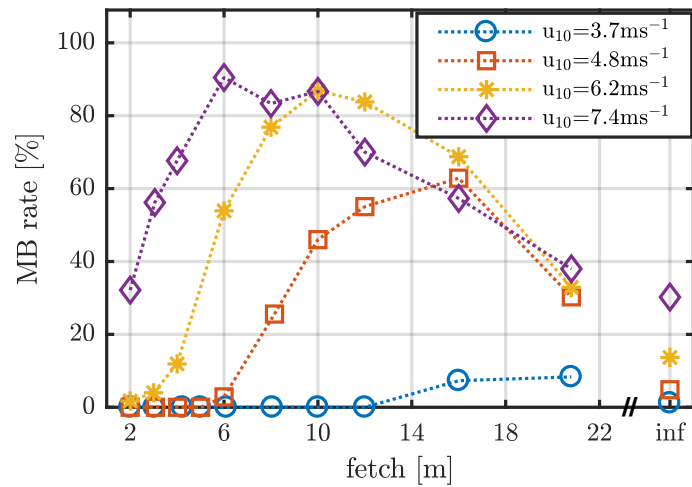


FIGURE 5.26: Percentage of breaking wave crests, denoted as MB rate, in dependence on fetch and wind speed. The most MB occurs at intermediate fetches and the number of microscale breaking waves decreases towards longer fetches. At low winds and short fetches no microscale breaking occurred. The dotted lines represent a guide to the eye.

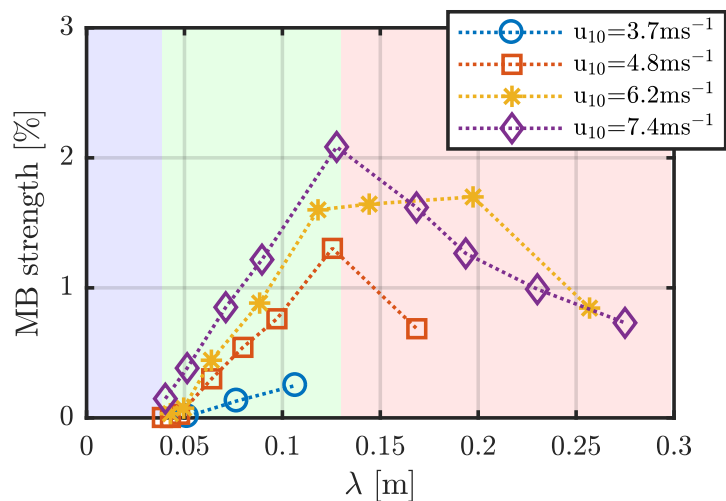


FIGURE 5.27: The wavelength dependent MB strength increases in regime B, and declines in regime C, similar to the heat transfer velocity. That also indicates the the microscale breaking indeed contributes to the heat and gas transfer velocities. The dotted lines represent a guide to the eye.

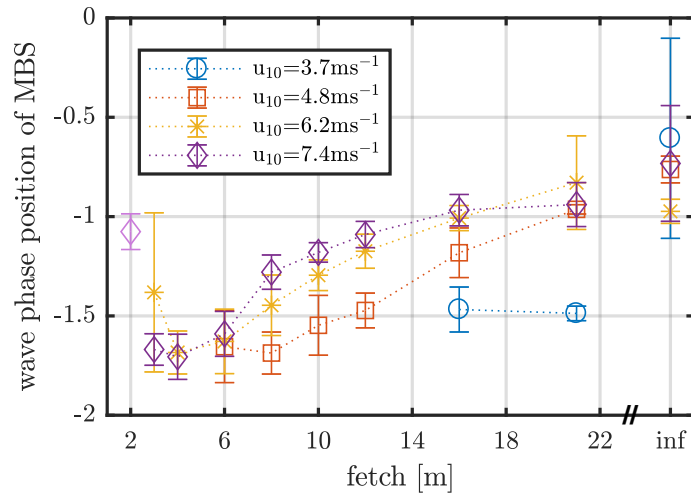


FIGURE 5.28: Wave phase position of MBS plotted against the dominant gravity wavelength. The wave phase position of MB changes for the different fetch conditions. The dotted lines represent a guide to the eye.

disturbance starts at a lower lee side position moving closer to the wave crest for longer fetches (see figure 5.28). That development is representative for the observed decrease in the formation of the toe/bulge. For longer fetches, the toe/bulge of the MB was less prominently formed.

Figure 5.29 shows the wave phase position plotted against the dominant gravity wavelength. The wave phase position is then following a single trajectory and is therefore one of the regime dependent variables.

Plotting the wave phase position of MBS against the strength of MB results in figure 5.30. There seems to exist a circular trajectory between these two variables.

5.4.4 Microscale wave breaking in dependence of the wave steepness

The occurrence of MB also correlates with a certain steepness threshold of $\eta > 0.06$ (see figure 5.31) for the average dominant gravity wave which is much smaller than the steepness threshold of wave breaking of 0.142 (e.g., Kinsman, 1965; Toffoli et al., 2010) and the steepness threshold of Crapper waves of 0.73 (Murashige and Choi, 2017). Additionally, the strength of MB (also referred to as MBS strength) seems to correlate with the wave steepness.

5.4.5 Microscale breaking and the surf similarity parameter

Figure 5.32 shows that the position of the incident MB disturbance along the wave crest seems to correlate with the adapted Iribarren number of the data. Since for wave breaking, the type of breaking, like spilling or plunging breakers, depends on the Iribarren number, also the type of MB breaking seems to be represented by a

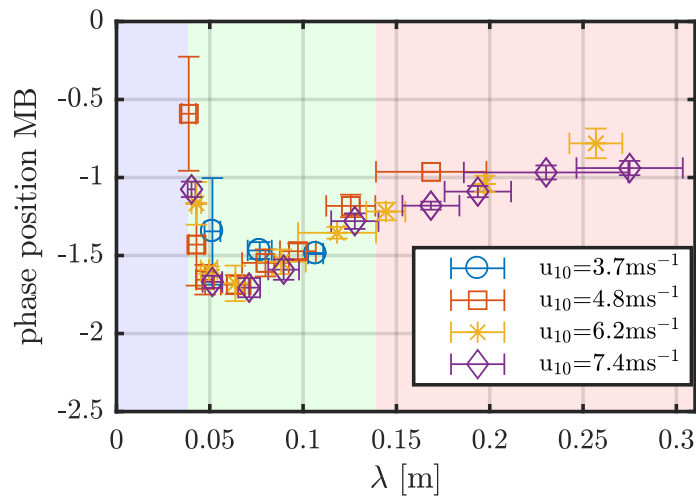


FIGURE 5.29: The wave phase position plotted against the wavelength follows a single trajectory for the different wind speeds, making it a regime dependent variable.

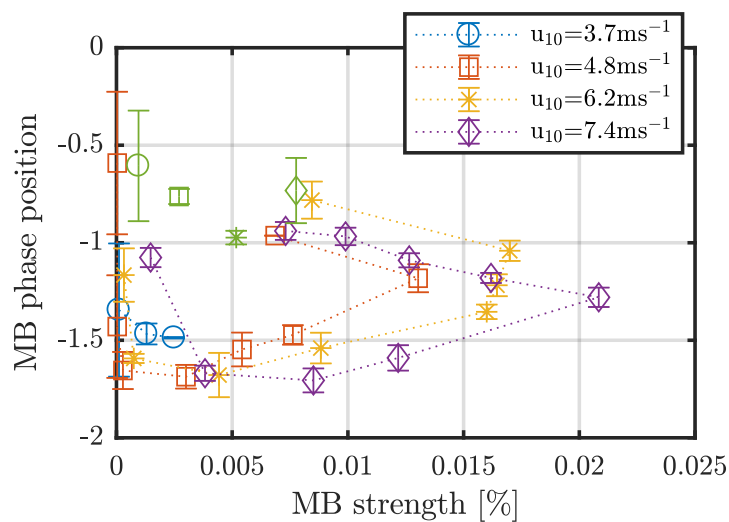


FIGURE 5.30: Wave phase position of MBS plotted against the strength of MB. There seems to exist a circular trajectory between these two variables. The green values show the infinite fetch data.

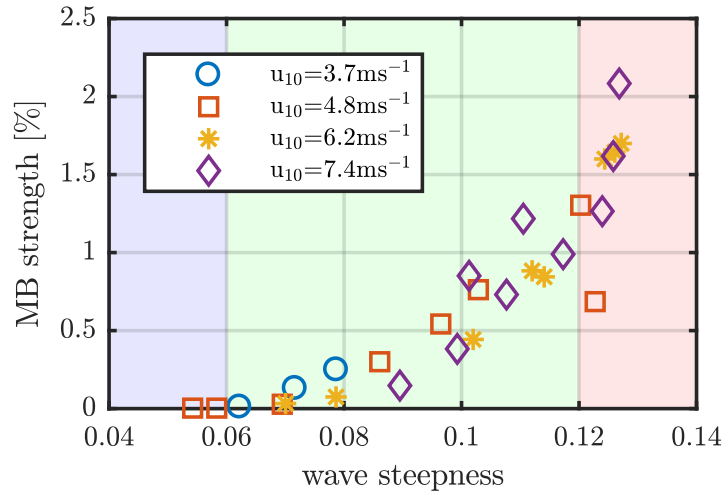


FIGURE 5.31: Strength of MB plotted against the steepness of the dominant gravity wave. The onset of MB is at a steepness of $\eta = 0.06$ which is less than half the steepness of a breaking wave.

change of the Iribarren number. The surf similarity parameter of regime B was larger than 3, while the surf similarity parameter of regime C is $\zeta' \leq 3$. Figure 5.33 shows the wave elevation of a wave of regime B and of regime B plotted over a Stokes wave profile. The waves of regime B show a slight asymmetry which may affect the type of microscale breaking similar to the differentiation of wave breaker into plunging and spilling.

5.4.6 Microscale breaking and heat transfer velocity

For infinite fetch, the heat transfer velocity correlates with the mean area percentage of the initial MBS event for each data set A_{MBS} . This agrees well with the observation of the streak regimes, where for infinite fetch the streaky structure is very broad and does not show the sharp gaps as for the finite fetch overshoot regime, indicating that not much surface renewal is caused by these streaks.

The fit shown in figure 5.34 is given as

$$k \left[\frac{\text{cm}}{\text{h}} \right] = 19.3(38) \text{ cm h}^{-1} A_{MBS} [\%] + 76(22) \text{ cm h}^{-1}. \quad (5.24)$$

The offset of this fit is the heat transfer velocity at which the microscale breaking started for infinite fetch.

Figure 5.35 shows the comparison if equation 5.24 is applied to the microscale breaking information of the finite fetch data sets. This was done to control if the measured data overshoot this modeled data which would indicate a second contribution to the heat and gas transfer velocities. However, on the contrary, the heat transfer velocities calculated utilizing the MB parametrization overshoot the measured heat transfer velocities. There can be two reasons for this observation. First, the wave

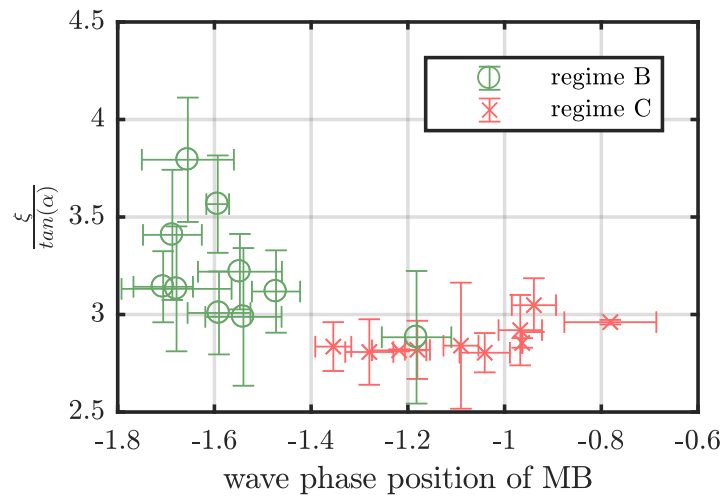


FIGURE 5.32: Adapted Iribarren number ζ' plotted against the wave phase position of MB. The data with too few statistics of MB have been excluded. The data belonging in regime B are plotted in green the data of regime C are plotted in red.

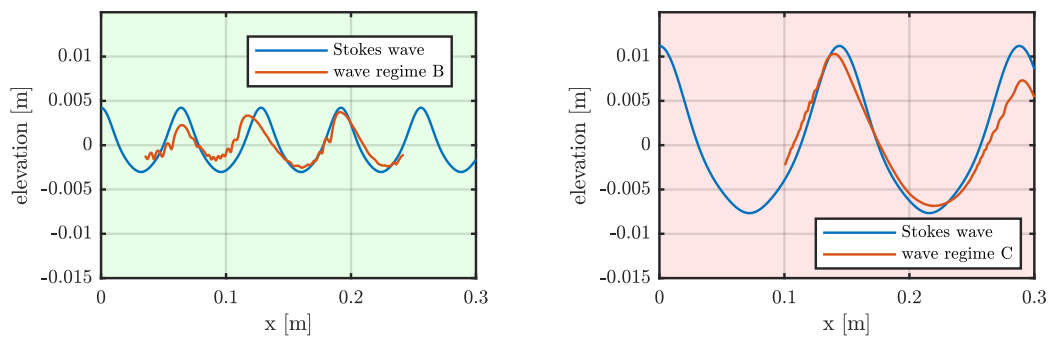


FIGURE 5.33: (left) Example of a stokes wave (depicted in blue) in comparison with a height reconstructed wave (red) of regime B of the FE. The small wiggles on the left hand slopes of the reconstructed waves are the parasitic capillary waves that are not governed by the stokes wave theory. (right) Example of a stokes wave (depicted in blue) in comparison with a height reconstructed wave (red) of regime C of the FE experiment.

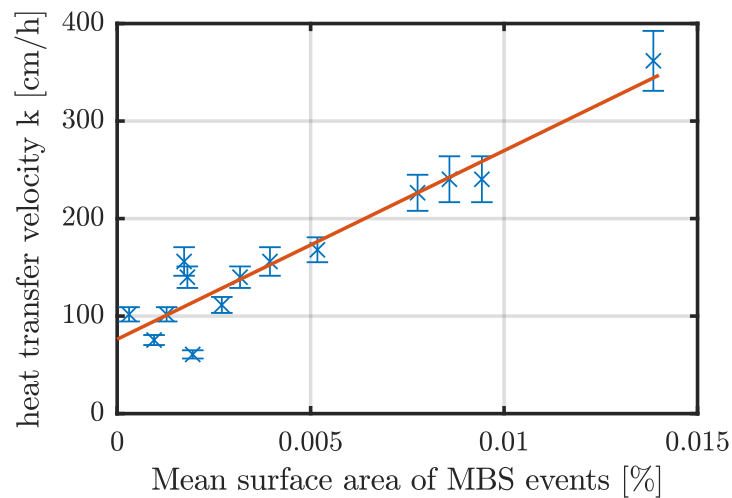


FIGURE 5.34: Heat transfer velocity k for infinite fetch plotted against the mean strength of the initial MBS disturbance per data set given as area percentage of the whole image. The heat transfer velocity for infinite fetch seems to correlate nearly linearly with the MBS strength.

phase position for the infinite fetch of MBS was different from the wave phase position of the shorter fetches of MBS. Therefore, the contribution of MB might not be similar. Second, the MBS strength was determined per image and not per single wave crest event. If for the infinite fetch a very broad wave crest underwent MB, then the surface renewal area might be significantly larger than for several smaller events distributed across the image. The calculated heat transfer velocities of regime C, however, show a decreasing trend towards the measured heat transfer velocities, which even gets reached for the highest wind speed condition and its longest fetch.

5.4.7 Occurrence of MB events over time

Besides the strength of MBS and the rate of MB, also the occurrence of MB events over time vary for the different regimes. Since it is not clear if the infinite fetch data can be counted towards regime C or if they are individual regimes due to the difference of fetch and duration limited wave growth, they were called regime 1 and 2, respectively. The separation between regime 1 and 2 was chosen because of the change in the streaky structure (see section 5.5).

5.5 Streak structures in the boundary layer

There occurred different types of streaky structures in the mass boundary layer of the BLI images. They could be classified into five different types. Three of the types coincide with the previously defined regimes A, B, and C. For the infinite fetch two regimes could be identified, referred to as regime 1 and 2.

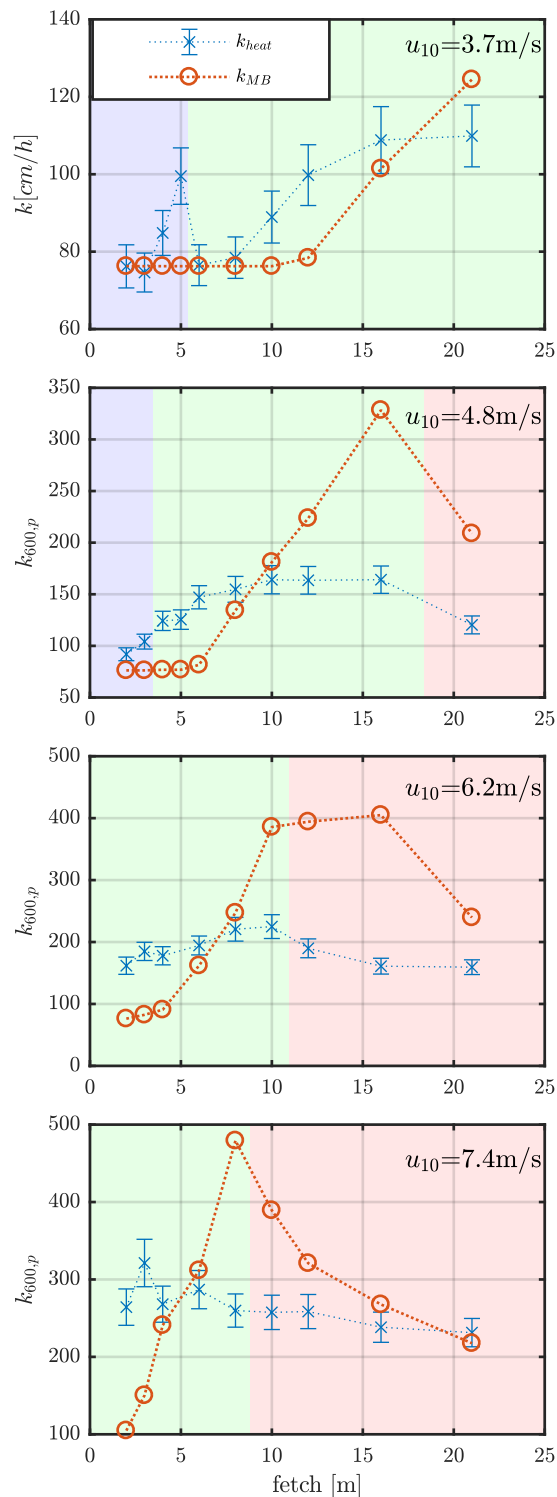


FIGURE 5.35: Comparison of the measured heat transfer velocities and using equation 5.24 on the microscale breaking information. If the finite fetch data are a combination of surface renewal due to MB and at least one other mechanism, then the red data should always be smaller or equal than the blue data. This is not the case, however, not only the strength of MB is affected by the fetch, also the position along the gravity wave phase which might cause a different impact of an MB of the same strength on the surface renewal of the boundary layer.

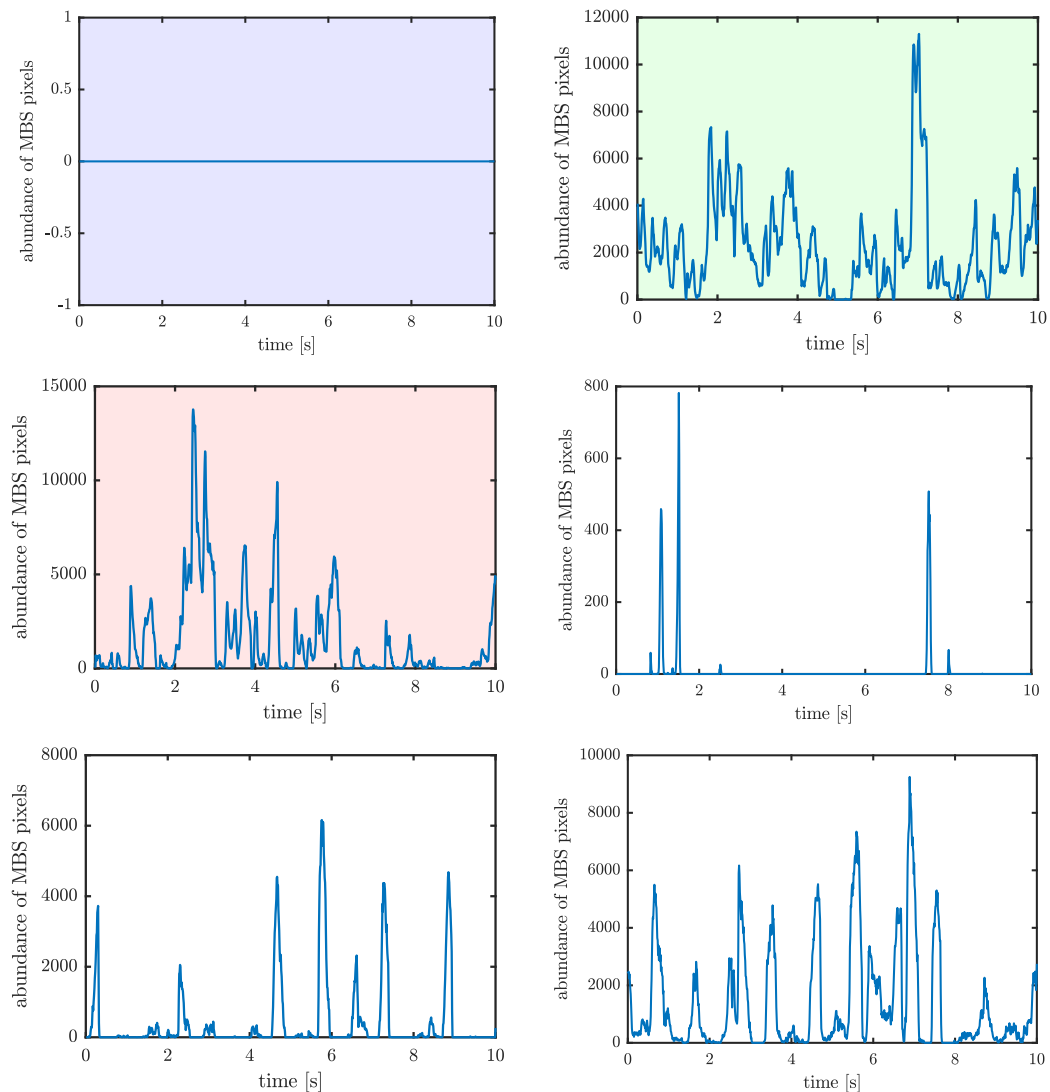


FIGURE 5.36: **(top left)** Regime A: Abundance of MBS pixel over time for 2m fetch and $u_{10} = 3.7 \text{ m s}^{-1}$. Not only did there occur no microscale breaking, also the wave field was not built either and consisted just of organized wiggles with two different dominant wavelengths. Their significant wave height was below the detection limit of the ISG. **(top right)** Regime B: Abundance of MBS pixel over time for finite fetch and $u_{10} = 4.8 \text{ m s}^{-1}$. The MB events are much less distinct than in the infinite fetch regimes and occur more frequently. **(middle left)** Regime C: Abundance of MBS pixel over time for 21m fetch and $u_{10} = 6.2 \text{ m s}^{-1}$. The MB events are now very variably where sometimes several successive strong MB breaker are followed up by nearly no MB for some seconds. **(middle right)** Regime 1: Abundance of MBS pixel over time for infinite fetch and $u_{10} = 3.7 \text{ m s}^{-1}$. **(bottom left)** Regime 1: Abundance of MBS pixel over time for infinite fetch and $u_{10} = 6.2 \text{ m s}^{-1}$. For infinite fetch the MB occurred much more apart and their appearance increases with increasing wind speed. **(bottom right)** Regime 2: Abundance of MBS pixel over time for infinite fetch and $u_{10} = 7.4 \text{ m s}^{-1}$. The MB events are now larger in size and occur more frequently as compared to the streaky pattern of regime 1.

5.5.1 Regime A: Laminar and fish scale regime - streaks

The small spaced and well aligned streaks occurred when the flow was still laminar (see figure 5.37).

In the laminar Regime occurred no microscale breaking and the wave crests were not significantly occupied by parasitic capillary waves. Figure 5.36 shows that no microscale breaking events have been detected for this regime and the wave elevation was close to the detection threshold. The water surface was disturbed by small organized wiggles with two different dominant wavelengths. The Reynolds number was smaller than $Re = 800$ for all laminar data sets of the FE. The dominant surface renewal mechanism was observed to be horseshoe-vortices. The fish-scale pattern for the longer fetches that were still in the laminar regime seem to confirm the theory proposed by Tsai et al. (2005) that they are caused by a smearing out and stretching of the initial upwelling areas of the horseshoe vortices. This theory fits well with the observations of the BLI data of the FE data sets.

Figure 5.39 shows the same wind speed of $u_{10} = 3.7 \text{ m s}^{-1}$ and a fetch of 4 meters. Here, the laminar area is only visible in the lower right corner of the image and the upwelling horseshoe vortices occur much more frequently. The same pattern is barely visible in the AT images (red).

In figure 5.3 can be seen, that in the laminar regime, where surface renewal only occurs by the upwelling of horseshoe vortices, the heat transfer velocity already increases significantly, followed up by a decrease at the regime change towards turbulent flow.

5.5.2 Regime B: Finite fetch with increasing microscale breaking - streaks

The overshoot regime of the finite fetch data shows the boundary layer streak pattern shown in figures 5.40 and 5.41. Two different images were chosen to show the streaky pattern with a big MB event and the thereby caused vanishing of the streaky pattern (figure 5.40) and the streaky pattern with no recent disturbance by a bigger MB event (figure 5.41). The streaks have a completely different structure compared to the other regimes. They are more equally spaced and in between the BLI signal vanishes completely.

5.5.3 Regime C: Finite fetch with declining microscale breaking - streaks

In the declining MBS regime, the boundary layer consists of small streaks directly after an MB event which quickly develops into broader streaks again until the next MB occurs (see figure 5.42). The recovered broader streaks show no significant surface renewal in between in contrast to the overshoot regime streaks.

There also occurred microscale breaking that only partly renewed the water surface in its wake (see figure 5.43).

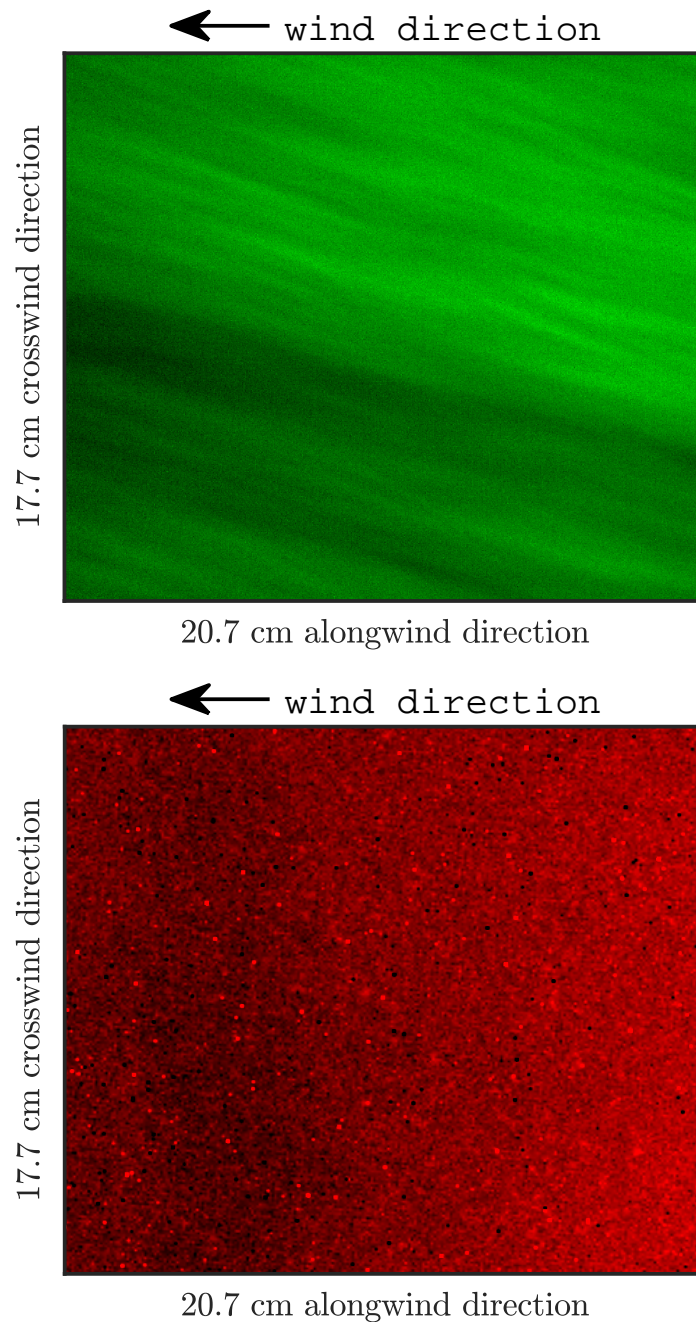


FIGURE 5.37: **(top)** 2m fetch and a wind speed of $u_{10} = 3.7 \text{ m s}^{-1}$ leads to a still laminar flow. The given image shows the laminar boundary layer where still no local upwelling due to horseshoe vortices occurs. **(bottom)** The same boundary layer as seen with thermography. A very early image of the time series was chosen such that the small streaky structure disturbance of the AT did not appear yet. Therefore the boundary layer in the AT image is not fully heated yet.

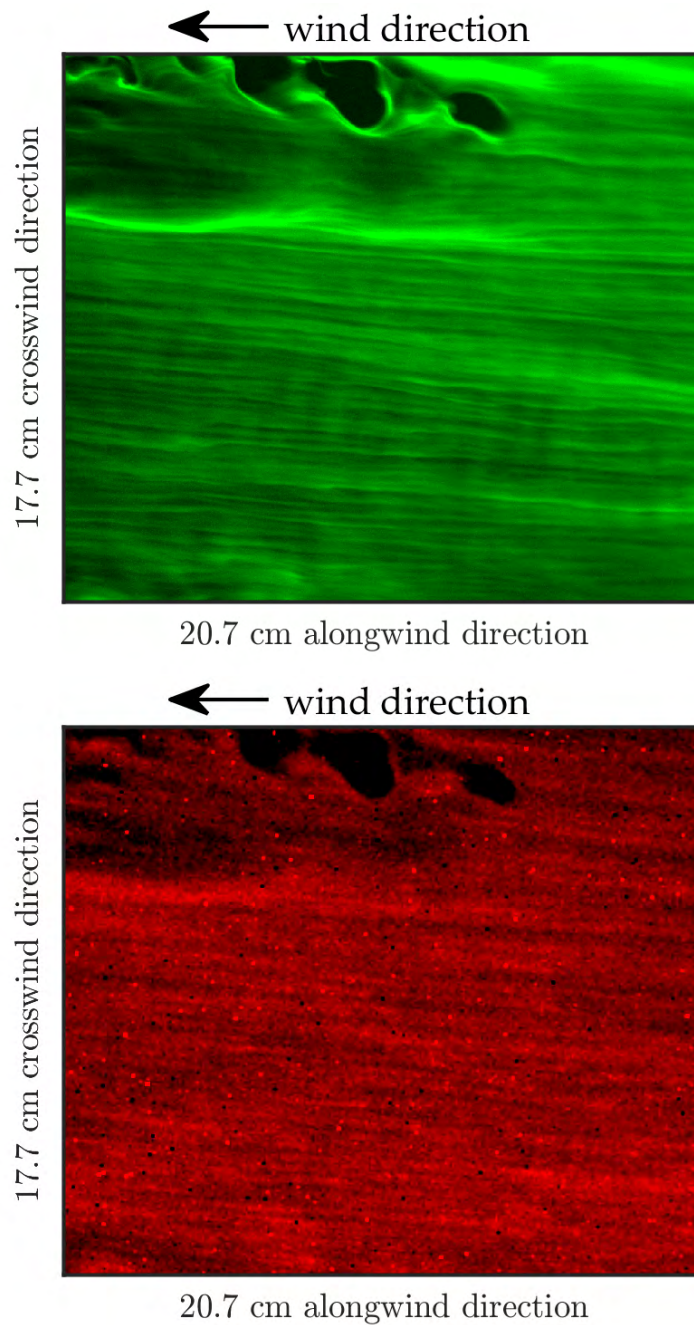


FIGURE 5.38: **(top)** 3m fetch and a wind speed of $u_{10} = 4.8 \text{ m s}^{-1}$ also leads to a still laminar flow. However, the first horseshoe vortices start to rise to the surface, causing a surface renewal and initiating the transition to streaks. The thin streaky structures appeared only when BLI and AT were measuring simultaneously. **(bottom)** The same boundary layer as seen with thermography.

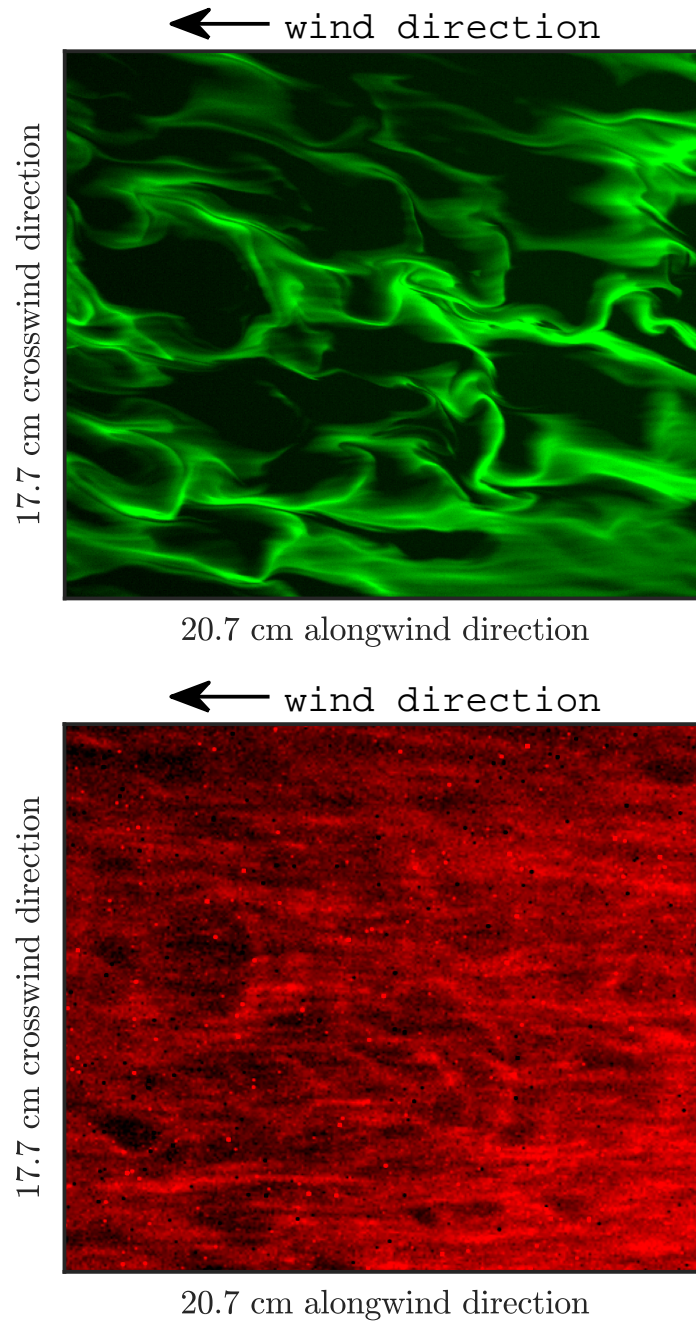


FIGURE 5.39: **(top)** For 4 m fetch and a wind speed of $u_{10} = 3.7 \text{ m s}^{-1}$ there occurred structures referred to as fish-scales. **(bottom)** The same pattern captured with the AT setup.

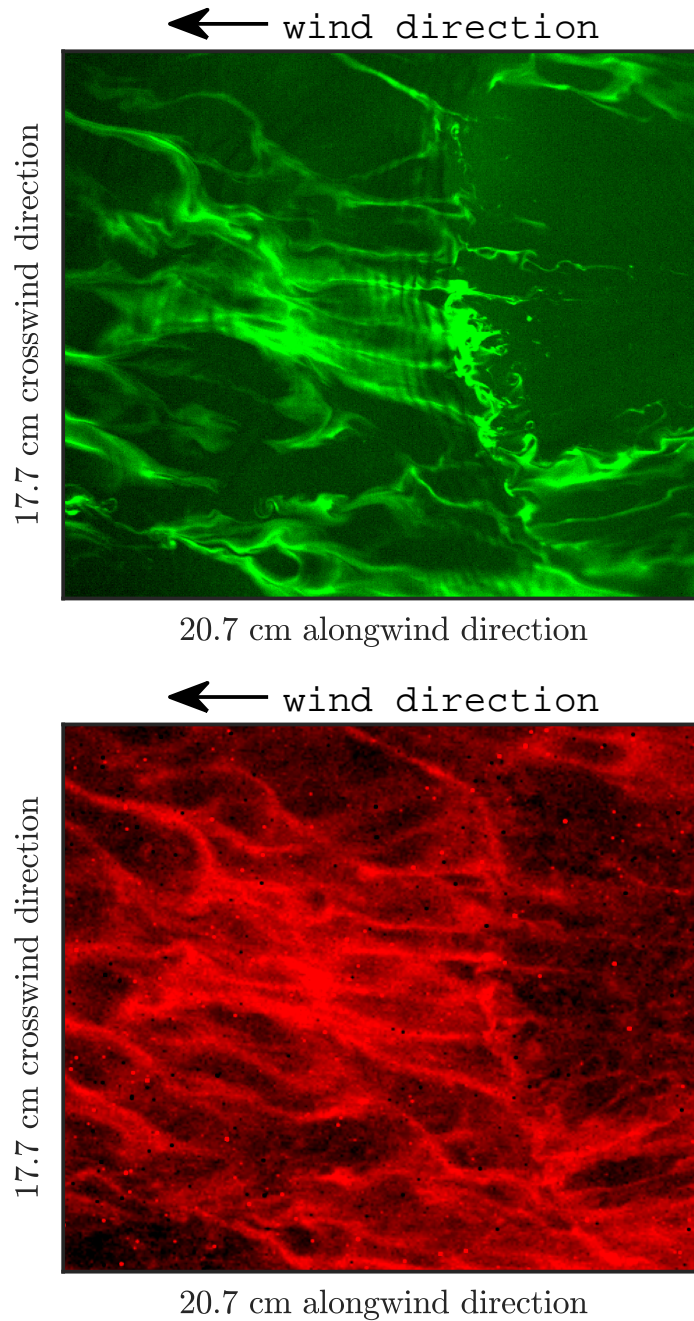


FIGURE 5.40: **(top)** 12 m fetch and a wind speed of $u_{10} = 4.8 \text{ m s}^{-1}$ lead to this type of streaky pattern. The chosen image also includes a typical MB event for the given measurement condition. **(bottom)** The streaky pattern as seen with the thermography setup.

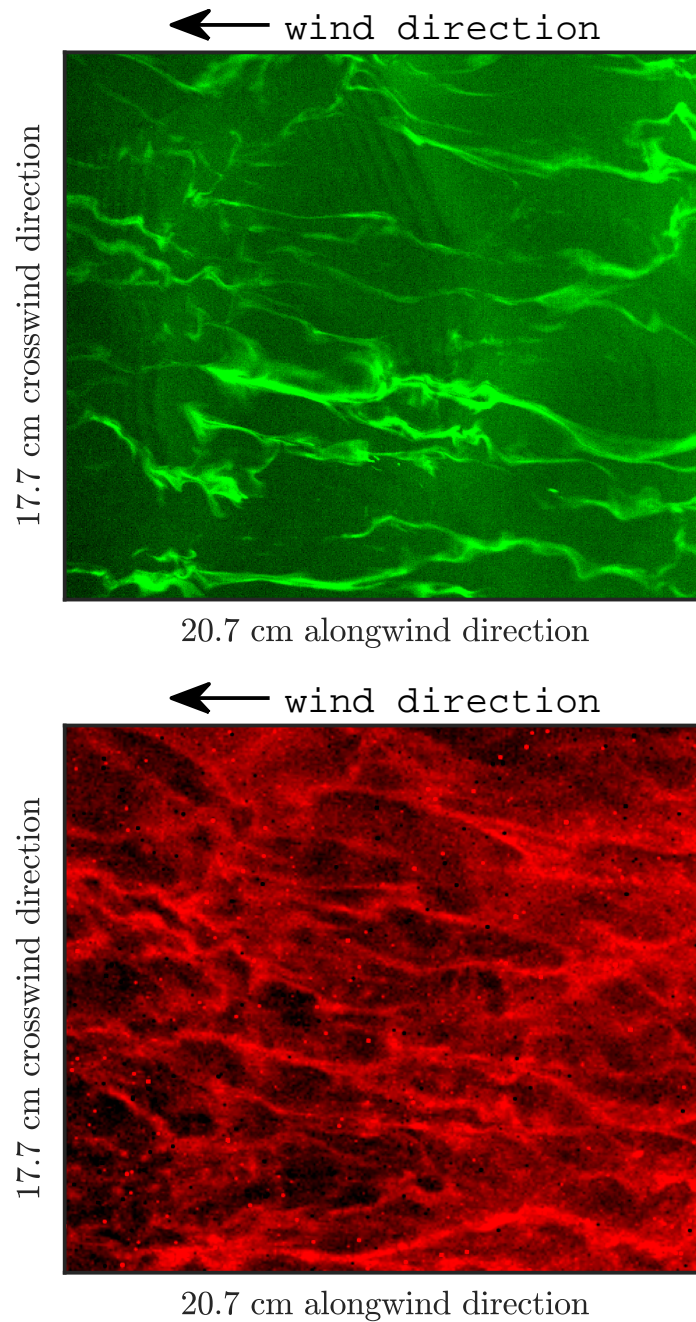


FIGURE 5.41: **(top)** 12 m fetch and a wind speed of $u_{10} = 4.8 \text{ m s}^{-1}$ lead to this type of streaky pattern. The chosen image shows the streaks of a time period where no MB occurred. The streaks are very slim and very regularly spaced. **(bottom)** The streaky pattern as seen with the thermography setup.

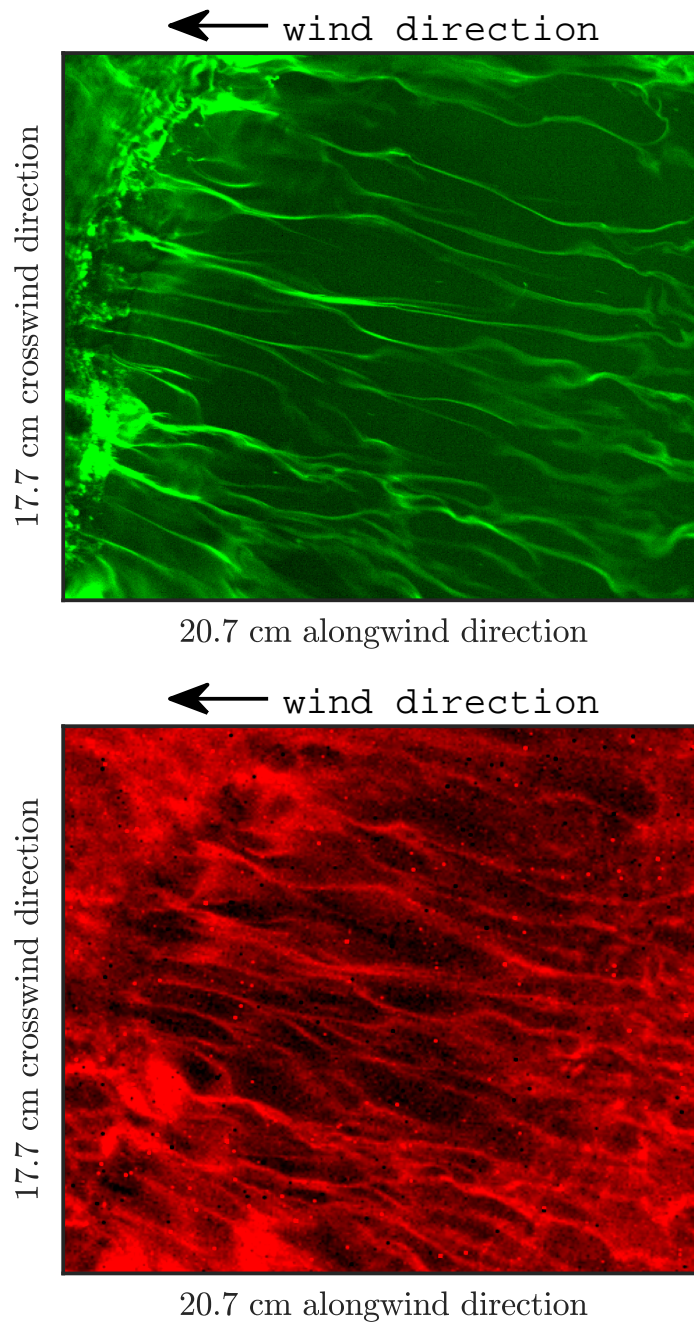


FIGURE 5.42: **(top)** 21 m fetch and a wind speed of $u_{10} = 6.2 \text{ m s}^{-1}$. The chosen image shows the alongwind stretching of the remaining streaks after an MB event. The streaks quickly get broader again. **(bottom)** The streaky pattern as seen with the thermography setup.

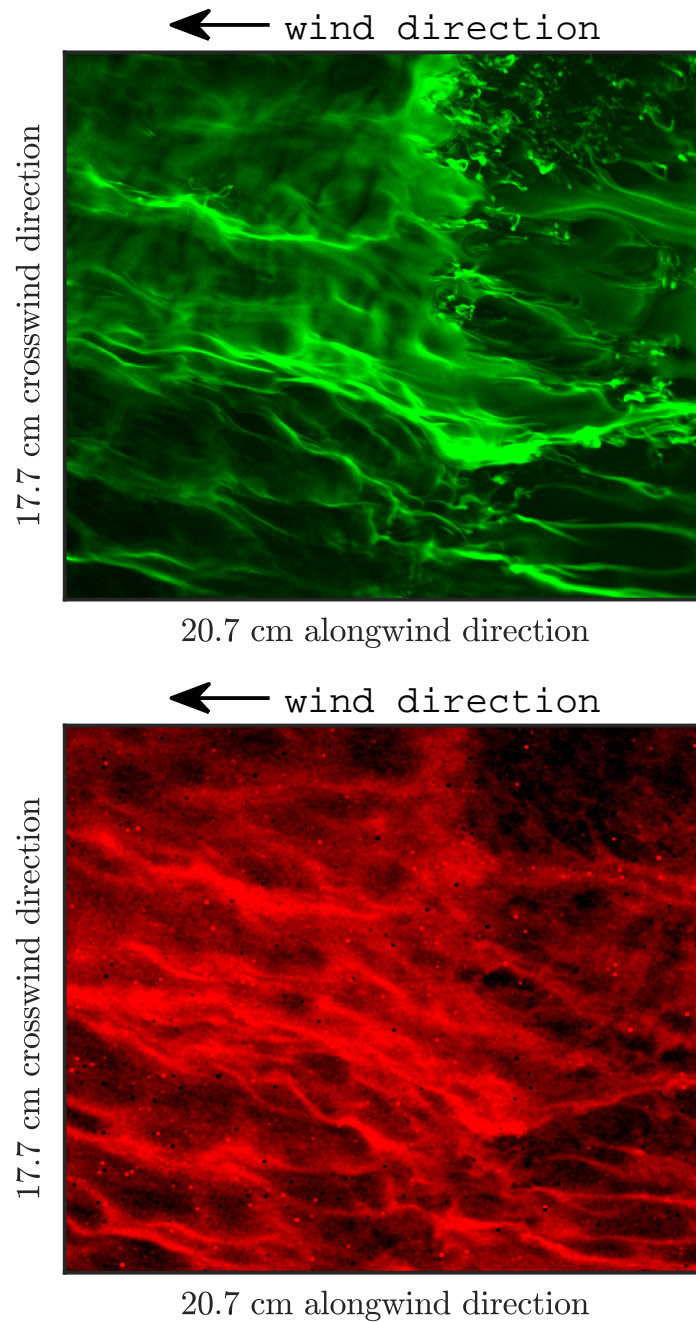


FIGURE 5.43: **(top)** 21 m fetch and a wind speed of $u_{10} = 6.2 \text{ m s}^{-1}$. The chosen MB event shows a different pattern compared to figure 5.42 where the mass boundary layer thickness is detaching from the surface in small curls. **(bottom)** The same time step as seen with the thermography setup.

5.5.4 Regime 1: Infinite fetch with sporadic microscale breaking - streaks

Another regime is the broad streaky regime that occurs for the infinite fetch data with $u_{10} < 7.3 \text{ m s}^{-1}$.

While for the laminar and fish scale streaks regime the streaky pattern is caused by the smearing out of the horseshoe vortices upwelling, the occasional appearance of toe formation microscale breaking events (see figure 5.36) is the underlying surface renewal mechanism that gets spread out by the Stokes drift of the waves and leads to a different streaky pattern in the mass boundary layer (see figure 5.44). The microscale breaking events usually occupy only a small fraction of the wave crest. Still, small toe cascading events can be observed. An explanation of toe cascading is given in chapter 5.4.1.

The occurrence of MB for this regime is seldom (see figure 5.36). Only from time to time occurs a small MB event followed up by several seconds of no MB. Still, an increase in MB can be found in this regime for increasing wind speed, agreeing with the observed increase in heat and gas transfer velocities (see figure 5.36).

5.5.5 Regime 2: Infinite fetch with broad and many microscale breaking - streaks

For the infinite fetch data with $u_{10} \geq 7.3 \text{ m s}^{-1}$ microscale breaking occurred much more frequently as compared to the data with lower wind speed. However, the microscale breaking is still distributed as distinguished single peaks, as opposed to the finite fetch microscale breaking data sets (see figure 5.36). The streaky structure consists of patches with small streak spacing divided by patches with much thinner boundary layer streaks (see figure 5.45). The cause for this pattern is most probably that the microscale breaker occupies a much broader wave crest width as compared to the lower wind speed MB and the surface renewal in their wake results in a broader area with renewing streaks.

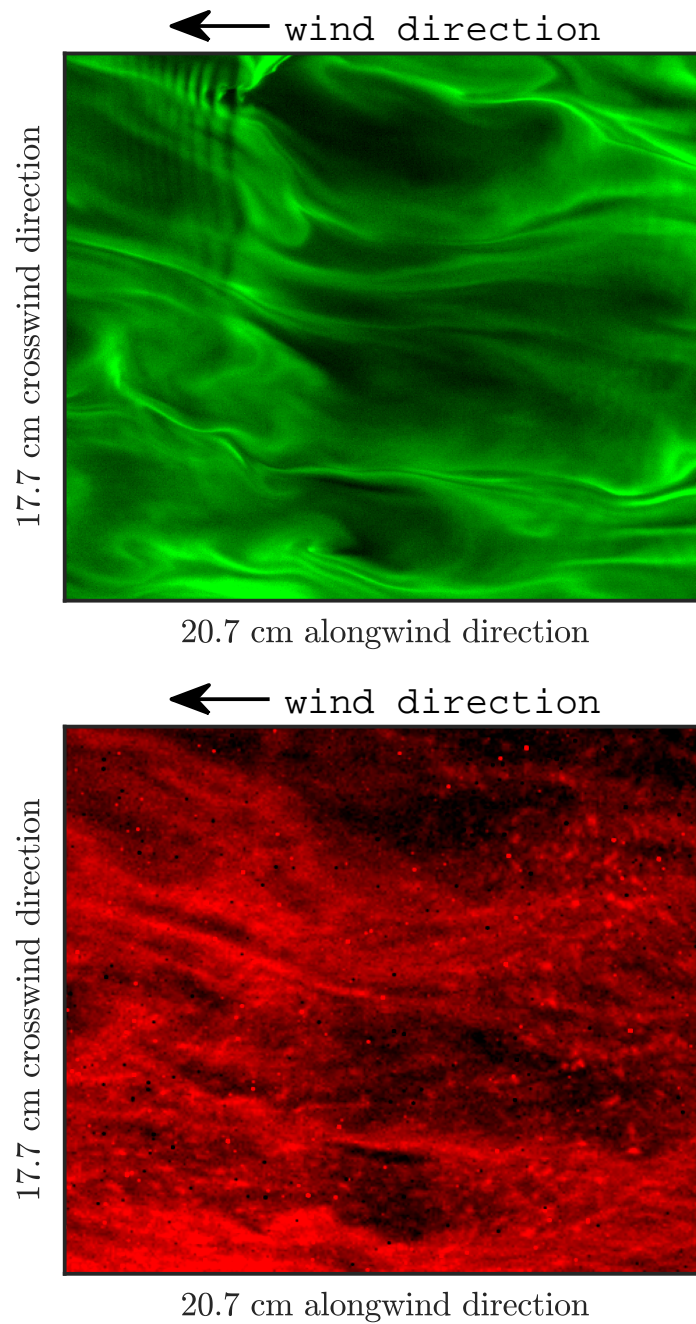


FIGURE 5.44: **(top)** Infinite fetch and a wind speed of $u_{10} = 3.7 \text{ m s}^{-1}$ lead to this type of streaky pattern. The chosen image also includes a typical MB event for the given measurement condition (upper left part of the image). A very small single vortex toe formation microscale breaking that caused practically no surface renewal. **(bottom)** The streaky pattern as seen with the thermography setup. The microscale breaking event is not clearly visible in the infrared images.

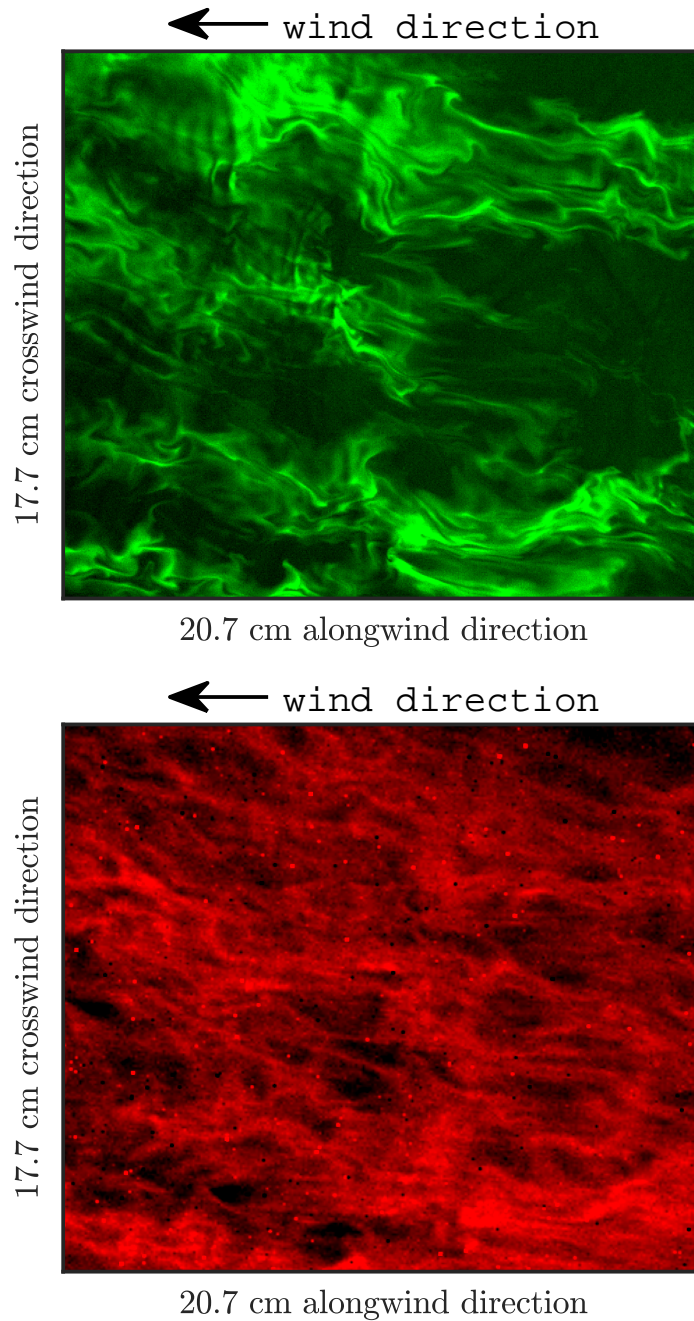


FIGURE 5.45: **(top)** Infinite fetch and a wind speed of $u_{10} = 7.4 \text{ m s}^{-1}$ lead to this type of streaky pattern. Narrow spaced streaks appear as patches and in between occur thin boundary layer regions. **(bottom)** The streaky pattern as seen with the thermography setup.

Chapter 6

Conclusions and Outlook

In the scope of this thesis, a measurement campaign was carried out that utilized the combined measurement techniques ISG, BLI, and AT, to investigate the fetch dependency of small-scale air-sea processes. Therefore, a wave absorber has been installed at the annular wind-wave facility Aeolotron, Heidelberg. For four different wind speeds between nine and ten fetches have been measured, varying between 2 m and 21 m. Additionally, quasi infinite fetch measurements were conducted by removing the wave absorber.

The resulting data of the wave slopes, a visualized fraction of the mass boundary layer, and the surface temperature, have then been analyzed for their fetch dependent development.

Conclusion

The fetch and wind dependent occurrence of microscale wave breaking and water sided mass boundary layer streaks was investigated in combination with the development of the wave field. A classification of three different regimes was implemented that depend on either the dominant gravity wavelength, the significant wave height, or the Reynolds number. They were named laminar regime (or regime A), overshoot regime (regime B), and declining regime (regime C). Regime A is defined by a Reynolds number smaller than 800 and no developed gravity waves yet. The dominant gravity wavelengths of Regime B were shorter than 13 cm and the Reynolds number was smaller than 10 000. Dominant gravity wavelengths larger than 13 cm defined regime C, where the Reynolds number was larger than 10 000.

The significant wave height of the FE depended linearly on the dominant gravity wavelength, which deviates from the Toba $3/2$ -power law. Several determined parameters, such as the mean square slope, and the dominant parasitic capillary wavelength, the local heat transfer velocities, the MB strength, and the MBS phase position, showed either directly a regime dependence or indirectly, by calculating the ratio between the parameter and the friction velocity.

For the finite fetch data, utilizing an adapted roughness Reynolds number, a correlation between the local heat transfer velocity, the mean square slope, and the friction velocity could be determined.

The data of the BLI measurement technique showed, that the initial disturbance causing the microscale wave breaking is accompanied by a previous accumulation of the mass boundary layer thickness in the parasitic capillaries. This effect could not be observed before since it is barely visible in previously used thermography images.

While for the data with a very sparse occurrence of MB, the MB events were characterized as single toe formation events, the larger MB events could be described by a mechanism, called toe cascading, that initiates a disturbance of the water surface which propagates the lee side of the gravity wave. It thereby initiates secondary toe formations in the capillary waves even further lee side of the wave crest.

A correlation between the occurrence of MB and the steepness of the waves was also discovered. The onset of MB occurs for waves with a steepness larger than $\eta = 0.06$.

For the infinite fetch, the occurrence of MB correlated directly with the heat transfer velocities. However, the same correlation did not fit the finite fetch data. For the same MB, it overestimated the heat transfer velocities, although in regime C, the overestimation decreases towards the measured heat transfer velocities, implying that the infinite fetch data might be the limiting case of regime C. The wave phase position of MBS varies for the regimes. Therefore, not only the strength of MB, but also the wave phase position of MBS might be of importance regarding its impact on local heat transfer velocities.

In the laminar regime, the dominant surface renewal mechanism is the upwelling of bulk water horse shoe vortices. Caused by an increased surface drift at the onset of wavy ripples, these upwelling regions are smeared out and result in the so-called fish-scale pattern. Thus, the observations of the FE in regime A agree with a theory stated by Tsai et al. (2005).

Outlook

The measurement campaign evaluated in this thesis governed a limited range of fetch conditions, while certain trends in regime C towards the infinite fetch conditions could be observed, it was not possible to further extend the range of the wave ages to fully cover the development of the wind wave field. This is due to the finite circumference of the Aeolotron wind-wave tank, in which this study was conducted with fetch limited conditions. Another measurement campaign with a time-limited wave age development could lead to an extended wave age development and close the gap towards infinite fetches. Additional local friction velocity measurements will also help to extend the range of measured local variables and prevents the need

to estimate the friction velocities using an empirical parameterization.

Further developments of the measurement techniques can also improve the investigation of the fetch dependent development of small-scale air-sea processes. E.g. Utilizing a light field setup to reconstruct the boundary layer thickness observed with BLI could lead to an improved calibration of the visible fraction of the mass boundary layer. Also, changing the chemical system used for BLI can lead to the visualization of the complete mass boundary layer thickness and not only a fraction of it.

Appendix A

Results as tables

The results are listed as tables in this appendix. The uncertainty of the data is given in brackets representing the uncertainty of the last digits of the given data before the brackets. The background colors blue green and red of the tables represent the three regimes, namely laminar (blue), overshoot (green), and decline (red) regime.

TABLE A.1: Local heat transfer velocities k_h and global gas transfer velocities k_g for infinite fetch. C represents the difference between the two water charges. Charge 1 was used for the finite fetch and infinite fetch without global gas transfer velocities, while charge 2 was used for infinite fetch with additional global gas transfer velocities.

| f_{wind} [Hz] | u_{10} [m/s] | C | u_b [m/s] | $u_{*,a}$ [m/s] | k_h [cm/h] | k_g [cm/h] | n | β |
|--------------------|-------------------|-----|----------------|--------------------|-----------------|-----------------|------|---------|
| 7.5 | 3.7(2) | 1 | 0.027(1) | 0.111(07) | 75.4(52) | - | - | - |
| 10.0 | 4.8(3) | 1 | 0.038(2) | 0.147(11) | 111.4(82) | - | - | - |
| 12.5 | 6.2(4) | 1 | 0.053(2) | 0.193(14) | 168.0(128) | - | - | - |
| 15.0 | 7.4(4) | 1 | 0.067(2) | 0.241(18) | 226.5(185) | - | - | - |
| 17.5 | 8.9(5) | 1 | 0.087(2) | 0.309(25) | 361.8(307) | - | - | - |
| 5.0 | 2.4(2) | 2 | 0.011(1) | 0.073(06) | 60.7(42) | 2.9 | 0.67 | 3.2(3) |
| 7.5 | 3.7(2) | 2 | 0.027(1) | 0.111(07) | 101.8(73) | 6.6 | 0.59 | 3.9(3) |
| 10.0 | 4.8(3) | 2 | 0.038(2) | 0.147(11) | 139.9(110) | 10.3 | 0.57 | 4.2(3) |
| 12.5 | 6.2(4) | 2 | 0.053(2) | 0.193(14) | 156.0(146) | 14.9 | 0.53 | 5.5(5) |
| 15.0 | 7.4(4) | 2 | 0.067(2) | 0.241(18) | 240.3(235) | 24.3 | 0.52 | 4.3(5) |
| 17.5 | 8.9(5) | 2 | 0.087(2) | 0.309(25) | - | 32.9 | 0.50 | - |

TABLE A.2: Local heat transfer velocities - fetch conditions. Here, only the $u_{*,a}$ parametrization data are shown since the alternative with a constant $u_{*,a}$ can be found in table A.1.

| f_{wind} [Hz] | u_{10} [m/s] | $u_{*,a}$ [m/s] | fetch [m] | k_h [cm/h] |
|--------------------|-------------------|--------------------|--------------|-----------------|
| 7.5 | 3.7(2) | 0.114(12) | 2 | 76.2(56) |
| | | 0.117(8) | 3 | 74.6(50) |
| | | 0.119(8) | 4 | 84.8(58) |
| | | 0.120(9) | 5 | 99.5(73) |
| | | 0.121(8) | 6 | 76.5(53) |
| | | 0.120(9) | 8 | 78.5(54) |
| | | 0.122(8) | 10 | 88.9(67) |
| | | 0.120(8) | 12 | 99.8(79) |
| | | 0.114(8) | 16 | 108.8(86) |
| | | 0.109(7) | 21 | 109.9(80) |
| 10.0 | 4.8(3) | 0.168(13) | 2 | 91.9(62) |
| | | 0.168(13) | 3 | 104.1(72) |
| | | 0.171(13) | 4 | 124.2(93) |
| | | 0.170(13) | 5 | 125.5(94) |
| | | 0.172(13) | 6 | 147.1(112) |
| | | 0.167(14) | 8 | 154.8(125) |
| | | 0.164(14) | 10 | 164.1(137) |
| | | 0.157(12) | 12 | 163.5(134) |
| | | 0.153(12) | 16 | 164.1(133) |
| | | 0.151(14) | 21 | 120.3(87) |
| 12.5 | 6.2(4) | 0.241(16) | 2 | 161.8(139) |
| | | 0.229(14) | 3 | 184.9(147) |
| | | 0.229(15) | 4 | 177.8(147) |
| | | 0.223(16) | 6 | 194.4(152) |
| | | 0.218(17) | 8 | 220.6(192) |
| | | 0.211(18) | 10 | 224.9(192) |
| | | 0.205(13) | 12 | 189.8(152) |
| | | 0.194(12) | 16 | 161.0(128) |
| | | 0.192(12) | 21 | 159.4(119) |
| | | 15.0 | 7.4(4) | 0.296(18) |
| 0.287(19) | 3 | | | 321.3(306) |
| 0.272(18) | 4 | | | 268.1(233) |
| 0.267(18) | 6 | | | 286.9(247) |
| 0.259(17) | 8 | | | 259.8(215) |
| 0.251(17) | 10 | | | 257.5(222) |
| 0.244(16) | 12 | | | 258.5(221) |
| 0.241(21) | 16 | | | 238.3(195) |
| 0.237(16) | 21 | | | 231.3(183) |

TABLE A.3: Fetch dependent wave field related variables of the FE. The **magenta** height values represent slight underestimations of the heights since the dominant gravity wavelength of these data was larger than the FOV and therefore no complete elevation reconstruction was acquired.

| f_{wind} [Hz] | fetch [m] | λ [cm] | h [cm] | c_p [cm/s] | T_s [s] | mss | λ_c [mm] |
|---------------------------|--------------|-------------------|-------------|-----------------|--------------|-------|---------------------|
| 7.5 | 2 | 17.5(41) | 0.06 | 40.8(95) | 0.43(13) | 0.003 | - |
| | 3 | 15.8(16) | 0.05 | 38.0(39) | 0.42(13) | 0.004 | - |
| | 4 | 15.5(14) | 0.05 | 36.2(33) | 0.43(13) | 0.004 | - |
| | 5 | 15.5(16) | 0.05 | 35.0(37) | 0.44(14) | 0.004 | - |
| | 6 | 4.9(4) | 0.07 | 34.2(30) | 0.14(2) | 0.004 | - |
| | 8 | 4.3(4) | 0.09 | 35.0(34) | 0.12(1) | 0.004 | - |
| | 10 | 4.4(4) | 0.21 | 33.7(29) | 0.13(2) | 0.009 | 8.2 |
| | 12 | 5.1(4) | 0.32 | 35.3(29) | 0.15(2) | 0.014 | 6.2 |
| | 16 | 7.7(7) | 0.55 | 41.5(35) | 0.19(3) | 0.021 | 6.0 |
| 21 | 10.7(4) | 0.84 | 46.9(18) | 0.23(4) | 0.026 | 6.1 | |
| 10.0 | 2 | 3.7(3) | 0.13 | 37.8(31) | 0.10(1) | 0.004 | - |
| | 3 | 3.7(3) | 0.14 | 38.5(33) | 0.10(1) | 0.006 | - |
| | 4 | 3.9(4) | 0.21 | 36.1(36) | 0.11(1) | 0.013 | 8.1 |
| | 5 | 4.3(4) | 0.25 | 36.6(35) | 0.12(1) | 0.017 | 7.9 |
| | 6 | 4.8(5) | 0.33 | 35.4(36) | 0.13(2) | 0.023 | 7.0 |
| | 8 | 6.4(8) | 0.55 | 39.0(49) | 0.16(2) | 0.030 | 5.3 |
| | 10 | 8.0(13) | 0.77 | 41.3(65) | 0.19(3) | 0.036 | 5.0 |
| | 12 | 9.7(10) | 1.00 | 46.7(46) | 0.21(4) | 0.040 | 4.9 |
| | 16 | 12.6(13) | 1.51 | 50.1(53) | 0.25(5) | 0.045 | 4.6 |
| 21 | 16.9(30) | 2.07 | 52.2(92) | 0.32(8) | 0.042 | 4.6 | |
| 12.5 | 2 | 3.3(3) | 0.22 | 33.9(30) | 0.10(1) | 0.028 | 9.3 |
| | 3 | 4.3(3) | 0.30 | 39.4(24) | 0.11(1) | 0.032 | 8.4 |
| | 4 | 5.0(5) | 0.39 | 39.7(36) | 0.13(1) | 0.036 | 6.8 |
| | 6 | 6.4(7) | 0.65 | 42.4(46) | 0.15(2) | 0.046 | 5.4 |
| | 8 | 8.8(13) | 0.99 | 45.5(67) | 0.19(3) | 0.053 | 4.6 |
| | 10 | 11.8(21) | 1.47 | 50.3(89) | 0.24(5) | 0.060 | 4.0 |
| | 12 | 14.4(10) | 1.82 | 55.2(40) | 0.26(5) | 0.059 | 3.9 |
| | 16 | 19.7(5) | 2.51 | 64.7(17) | 0.31(7) | 0.056 | 5.5 |
| | 21 | 25.7(14) | 2.93 | 67.1(37) | 0.38(11) | 0.052 | 5.6 |
| 15.0 | 2 | 4.0(2) | 0.36 | 37.1(19) | 0.11(1) | 0.049 | 7.4 |
| | 3 | 5.1(5) | 0.51 | 40.8(41) | 0.13(1) | 0.051 | 6.1 |
| | 4 | 7.1(6) | 0.72 | 48.1(40) | 0.15(2) | 0.056 | 5.4 |
| | 6 | 9.0(8) | 0.99 | 50.5(47) | 0.18(3) | 0.063 | 4.7 |
| | 8 | 12.8(13) | 1.62 | 55.3(55) | 0.23(4) | 0.070 | 4.1 |
| | 10 | 16.9(15) | 2.12 | 60.8(55) | 0.28(6) | 0.072 | 4.4 |
| | 12 | 19.4(18) | 2.40 | 66.3(61) | 0.29(7) | 0.070 | 4.9 |
| | 16 | 23.0(44) | 2.70 | 68.8(132) | 0.34(8) | 0.068 | 5.5 |
| | 21 | 27.5(29) | 2.96 | 72.4(75) | 0.38(10) | 0.067 | 6.8 |

TABLE A.4: Infinite fetch wave field related variables of the FE. The infinite fetch measurements of water charge 2 were each conducted twice, with a different ammonia influx in the air compartment. Therefore, also the wave related parameters could be determined for both data sets. The low ammonia data sets are denoted with 2-1, the high ammonia data sets as 2-2. However, the mean square slope of 2-1 and 2-2 are the same measurement. The underestimated heights due to the wavelengths exceeding the FOV are depicted in magenta.

| f_{wind} [Hz] | charge | λ [cm] | h [cm] | c_p [cm/s] | T_s [s] | mss |
|---------------------------|--------|-------------------|-------------|-----------------|--------------|-------|
| 7.5 | 1 | 14.3(30) | 1.1 | 45.9(96) | 0.31(7) | 0.016 |
| 10.0 | 1 | 27.4(25) | 2.2 | 58.4(54) | 0.47(15) | 0.023 |
| 12.5 | 1 | 29.3(14) | 2.7 | 56.7(28) | 0.52(18) | 0.036 |
| 15.0 | 1 | 37.0(48) | 3.2 | 63.3(82) | 0.58(22) | 0.057 |
| 17.5 | 1 | 58.7(82) | 3.6 | 73.0(102) | 0.80(36) | 0.079 |
| 5.0 | 2-1 | 16.4(25) | 0.6 | 56.6(86) | 0.29(7) | 0.01 |
| 7.5 | 2-1 | 19.5(40) | 1.0 | 60.0(122) | 0.33(8) | 0.014 |
| 10.0 | 2-1 | 29.9(75) | 1.6 | 61.9(156) | 0.48(16) | 0.017 |
| 12.5 | 2-1 | 38.8(142) | 2.9 | 67.4(247) | 0.58(21) | 0.027 |
| 15.0 | 2-1 | 64.1(225) | 3.3 | 81.2(285) | 0.79(35) | 0.058 |
| 17.5 | 2-1 | 62.5(271) | 3.7 | 69.1(299) | 0.91(43) | 0.079 |
| 5.0 | 2-2 | 14.4(24) | 0.7 | 53.9(89) | 0.27(6) | - |
| 7.5 | 2-2 | 19.4(37) | 1.1 | 60.0(113) | 0.32(8) | - |
| 10.0 | 2-2 | 27.0(77) | 2.0 | 60.2(171) | 0.45(14) | - |
| 12.5 | 2-2 | 45.8(121) | 2.9 | 66.8(177) | 0.69(28) | - |
| 15.0 | 2-2 | 42.7(112) | 3.3 | 58.9(154) | 0.73(31) | - |
| 17.5 | 2-2 | 40.2(131) | 3.4 | 60.8(198) | 0.66(26) | - |

TABLE A.5: Fetch dependent microscale breaking related variables of the FE.

| f_{wind} [Hz] | fetch [m] | MBS strength [%] | MB phase position | rate of MB [%] |
|---------------------------|--------------|---------------------|-------------------|-------------------|
| 7.5 | 2 | - | - | - |
| | 3 | - | - | - |
| | 4 | - | - | - |
| | 5 | - | - | - |
| | 6 | - | - | - |
| | 8 | - | - | - |
| | 10 | - | - | - |
| | 12 | 0.01 | -1.35 | - |
| | 16 | 0.13 | -1.47 | 7.3 |
| 21 | 0.25 | -1.49 | 8.3 | |
| 10.0 | 2 | - | - | - |
| | 3 | - | - | - |
| | 4 | 0.01 | -0.59 | - |
| | 5 | 0.01 | -1.43 | - |
| | 6 | 0.03 | -1.66 | 2.9 |
| | 8 | 0.30 | -1.69 | 25.6 |
| | 10 | 0.54 | -1.55 | 46.0 |
| | 12 | 0.76 | -1.47 | 55.1 |
| | 16 | 1.30 | -1.18 | 62.9 |
| 21 | 0.69 | -0.96 | 30.3 | |
| 12.5 | 2 | - | - | - |
| | 3 | 0.03 | -1.17 | 4.0 |
| | 4 | 0.08 | -1.59 | 11.9 |
| | 6 | 0.44 | -1.68 | 53.9 |
| | 8 | 0.88 | -1.54 | 76.9 |
| | 10 | 1.60 | -1.35 | 86.8 |
| | 12 | 1.64 | -1.22 | 83.8 |
| | 16 | 1.70 | -1.04 | 68.8 |
| | 21 | 0.84 | -0.78 | 32.9 |
| 15.0 | 2 | 0.15 | -1.08 | 32.2 |
| | 3 | 0.38 | -1.67 | 56.2 |
| | 4 | 0.85 | -1.71 | 67.7 |
| | 6 | 1.22 | -1.59 | 90.5 |
| | 8 | 2.08 | -1.28 | 83.3 |
| | 10 | 1.62 | -1.18 | 86.7 |
| | 12 | 1.27 | -1.09 | 70.0 |
| | 16 | 0.99 | -0.97 | 57.3 |
| | 21 | 0.73 | -0.94 | 38.0 |

TABLE A.6: Infinite fetch microscale breaking related variables of the FE.

| f_{wind} [Hz] | charge | MBS strength [%] | MB phase position | rate of MB [%] |
|---------------------------|--------|---------------------|-------------------|-------------------|
| 7.5 | 1 | 0.10 | -0.61 | 1.2 |
| 10.0 | 1 | 0.27 | -0.76 | 4.8 |
| 12.5 | 1 | 0.52 | -0.97 | 13.7 |
| 15.0 | 1 | 0.78 | -0.73 | 30.2 |
| 17.5 | 1 | 1.39 | -0.79 | 43.0 |
| 5.0 | 2-1 | - | - | - |
| 7.5 | 2-1 | 0.03 | -0.62 | - |
| 10.0 | 2-1 | 0.32 | -0.50 | 6.5 |
| 12.5 | 2-1 | 0.40 | -0.90 | 2.8 |
| 15.0 | 2-1 | 0.86 | -0.76 | 36.4 |
| 17.5 | 2-1 | 2.56 | -0.57 | 31.3 |
| 5.0 | 2-2 | 0.20 | -0.91 | - |
| 7.5 | 2-2 | 0.13 | -0.60 | 1.4 |
| 10.0 | 2-2 | 0.18 | -0.82 | 4.0 |
| 12.5 | 2-2 | 0.17 | -0.87 | 2.3 |
| 15.0 | 2-2 | 0.94 | -0.86 | 37.7 |
| 17.5 | 2-2 | 1.71 | -0.93 | 47.7 |

Appendix B

Additional image material

B.1 Visualization

This section is about the visualization implemented to present the given data in the thesis. For a qualitative visualization of the mass boundary layer via thermography and BLI, the scaling of the given data has been automatized and the dynamic range was adapted for a better visual representation.

B.1.1 ISG visualization

For the visualization in this thesis, especially the surface reconstruction of the wave elevation (see chapter 4.1.1), determined by integrating the slopes of the ISG measurement technique, are of importance.

The elevation can be plotted using the *surf* function of MATLAB. As a viewing angle an elevation of 50° and an azimuth of -10° was chosen. The resulting image looks like figure B.1.

To enhance the visualization of the parasitic capillary waves a lighting condition was added by changing the *facelighting* option of the plot as a *gouraud* lighting that is especially useful to highlight curved surfaces. With the additional lighting figure B.1 changes to figure B.2. The same lighting condition was also applied to the surface plots of the BLI and AT images. However, a compromise has to be found in visualizing the capillaries using a lighting source and not over illuminate the surface plot (see figure B.3), because that would cause a more difficult visualization of the overlaid BLI and AT structures discussed in the next subsection.

B.1.2 BLI visualization

For the visualization of the BLI images, the compressed intensities of the original compression was used to reduce the dynamic range. Additionally, the range of the visualized intensity values were chosen as the mean intensity of the image subtracted by the standard deviation of the intensities as minimum intensity and the mean added with twice the standard deviation of the intensities as maximum value. The comparison of the change of the dynamic range can be seen in figures B.4 and B.5.

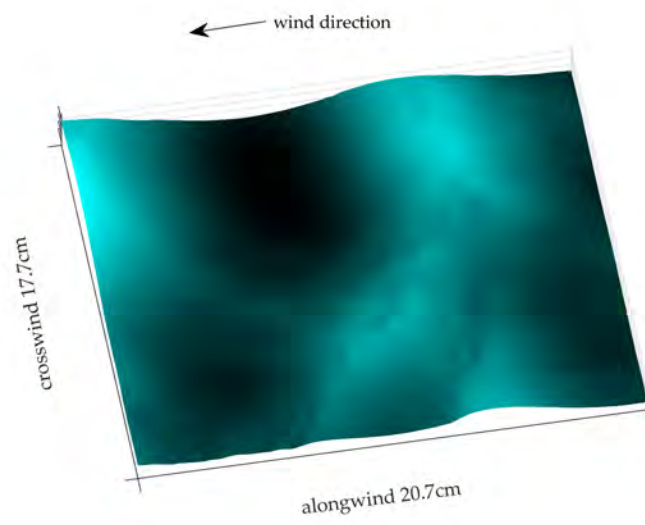


FIGURE B.1: Visualization of the water surface with no additional lighting.

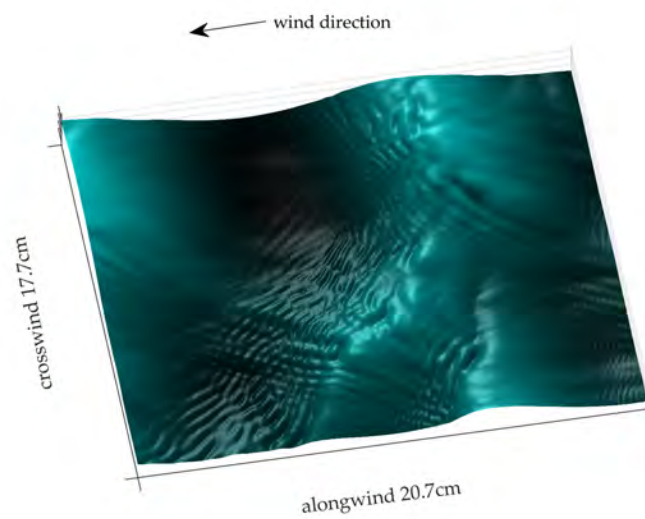


FIGURE B.2: Visualization of the water surface with the addition of a lighting source to emphasize the curvature of the parasitic capillary waves.

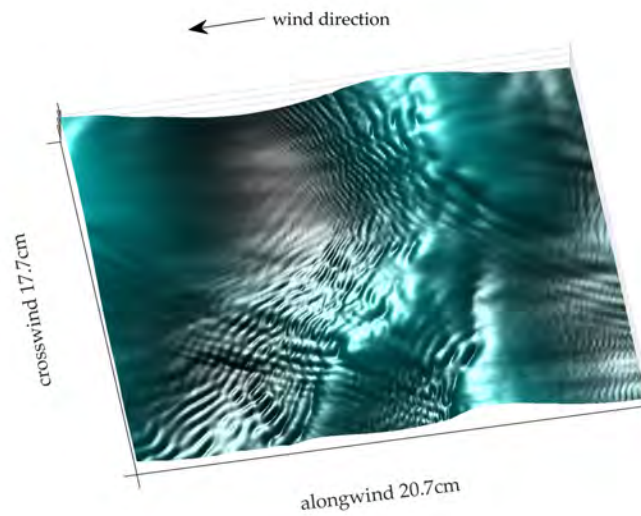


FIGURE B.3: Visualization of the water surface with the addition of a lighting source to emphasize the curvature of the parasitic capillary waves. Here the lighting was chosen too strong and from a different angle, which on the one hand visualized even more parasitic capillaries, but on the other hand would prevent the images to be overlaid with other structures.

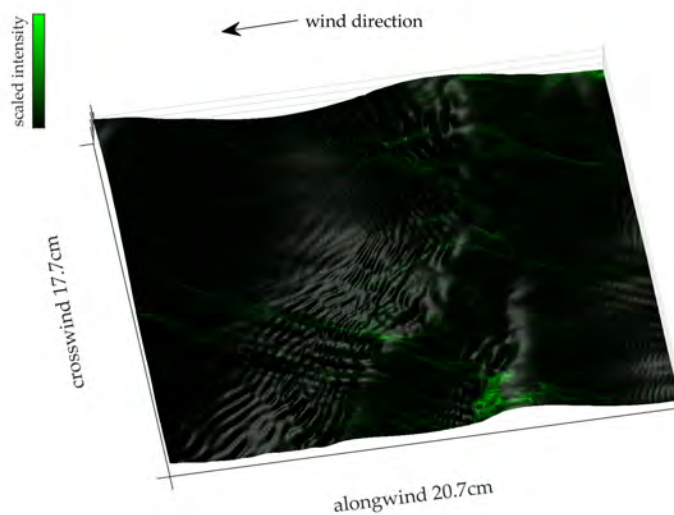


FIGURE B.4: Visualization of the mass boundary layer using the BLI images. With no adaption of the dynamic range for the visualization it is nearly impossible to see the streaky structure since the intensity of the image is dominated by a few bright areas.

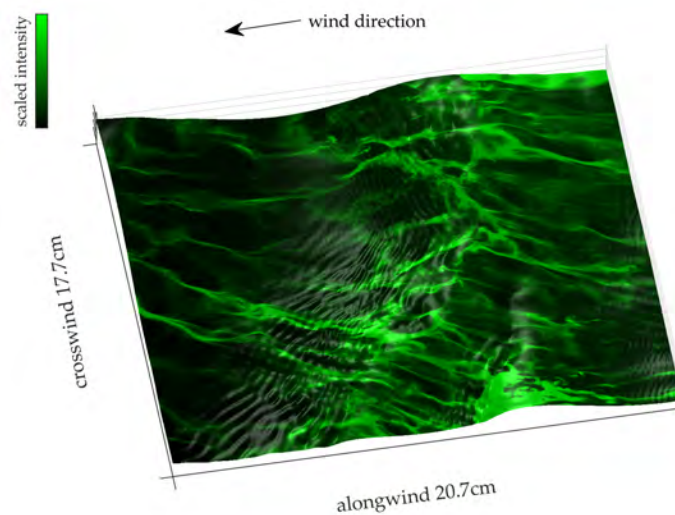


FIGURE B.5: The adapted dynamic range makes the structures visible in the visualization.

B.1.3 AT visualization

The IR-camera used in the AT setup showed several dead pixels which had to be filtered out prior to the image transformation onto the ISG grid. Additionally, the range of the visualized temperature also was adapted using an automated threshold via the mean and the standard deviation of the signal similar to the BLI images. The intensity values are given as the temperature times 10000, so that a temperature of 22° was captured as an internally calibrated intensity value of 22000. Therefore the intensity range adaption for the visualization was important, so that the scale does not start at zero (see figure B.6). Since the intensity variations in the streaky structures of the thermography images is not as large as in the BLI images, for minimum and maximum intensity just the single standard deviation was used instead of twice the standard deviation for the upper limit.

B.2 Development of MB along the fetch

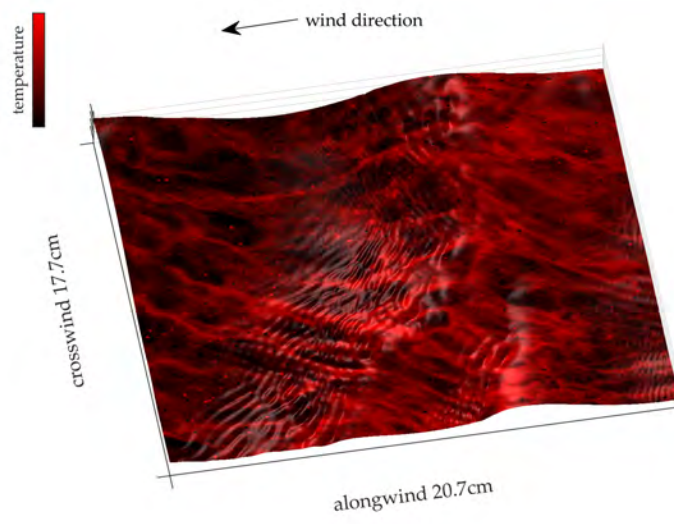


FIGURE B.6: The adapted dynamic range makes also the structures visible in the thermography visualization.

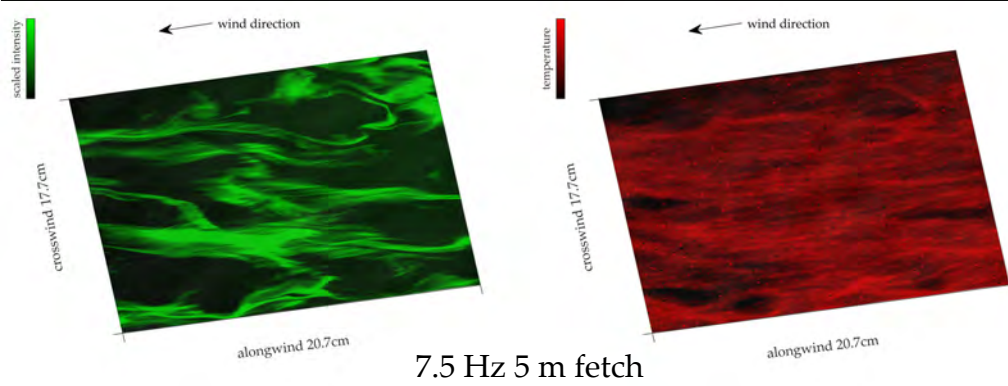
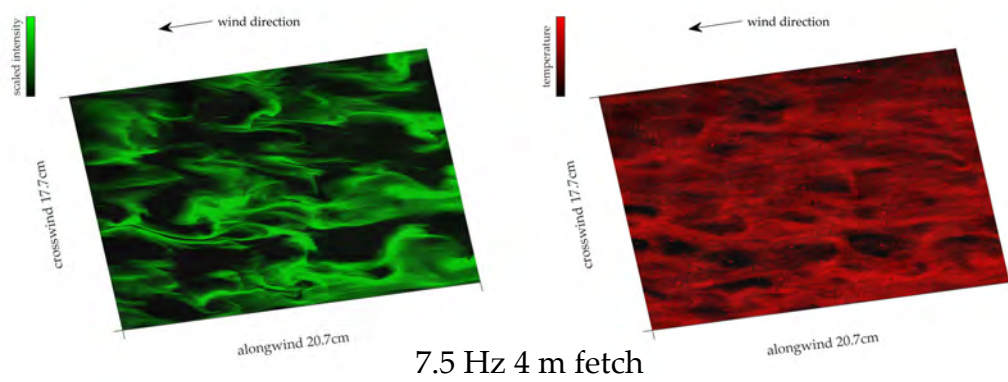
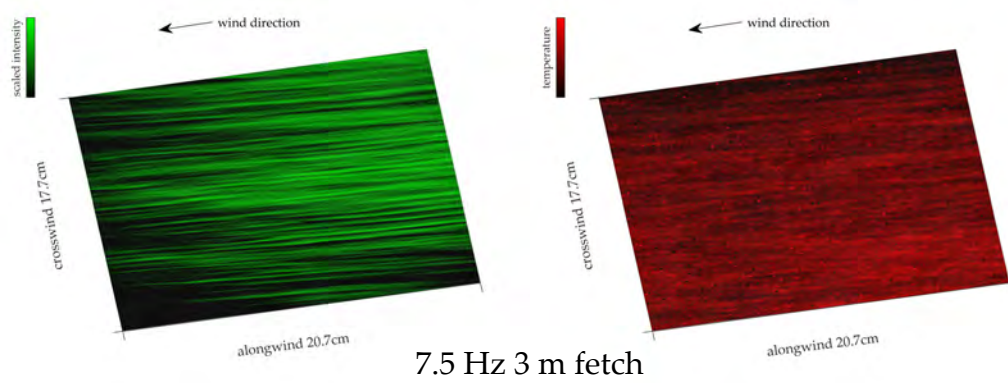
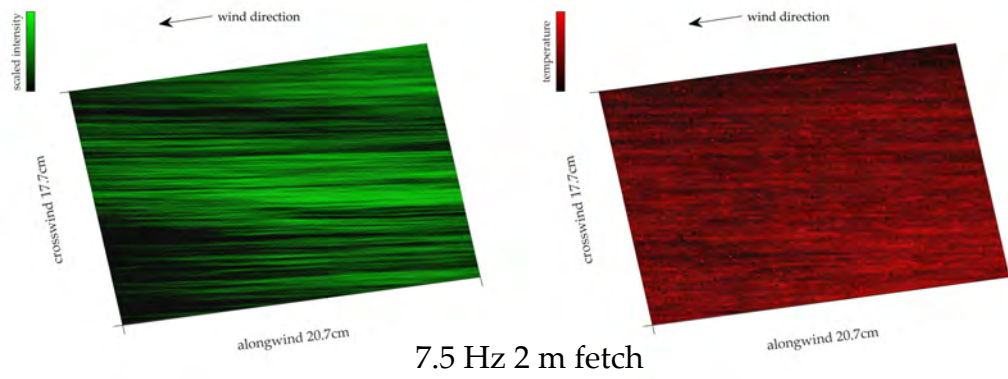


FIGURE B.7: Example images at same times of BLI (green) and AT (red) for $u_{10} = 3.7 \text{ m s}^{-1}$ - part 1.

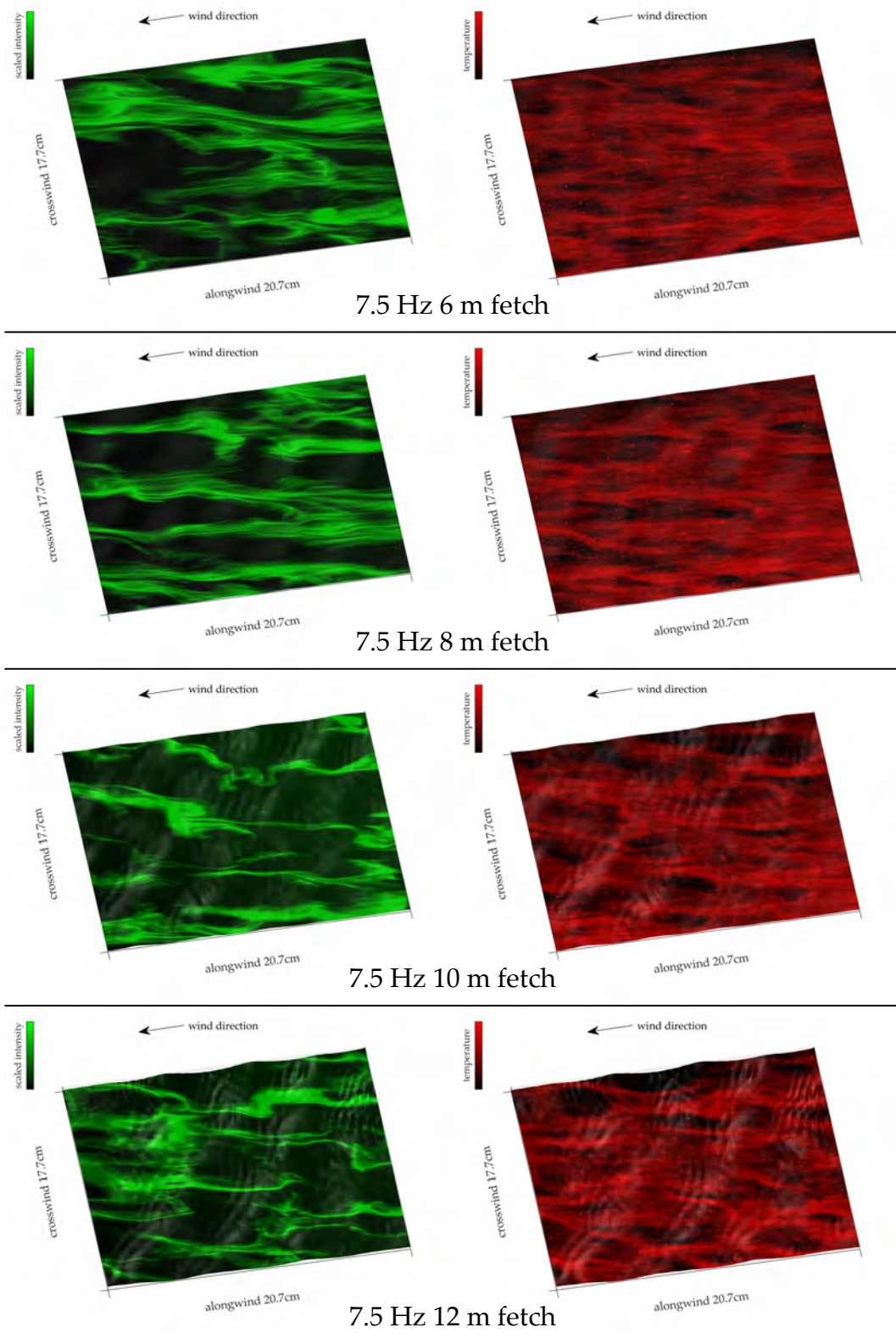


FIGURE B.8: Example images at same times of BLI (green) and AT (red) for $u_{10} = 3.7 \text{ m s}^{-1}$ - part 2.

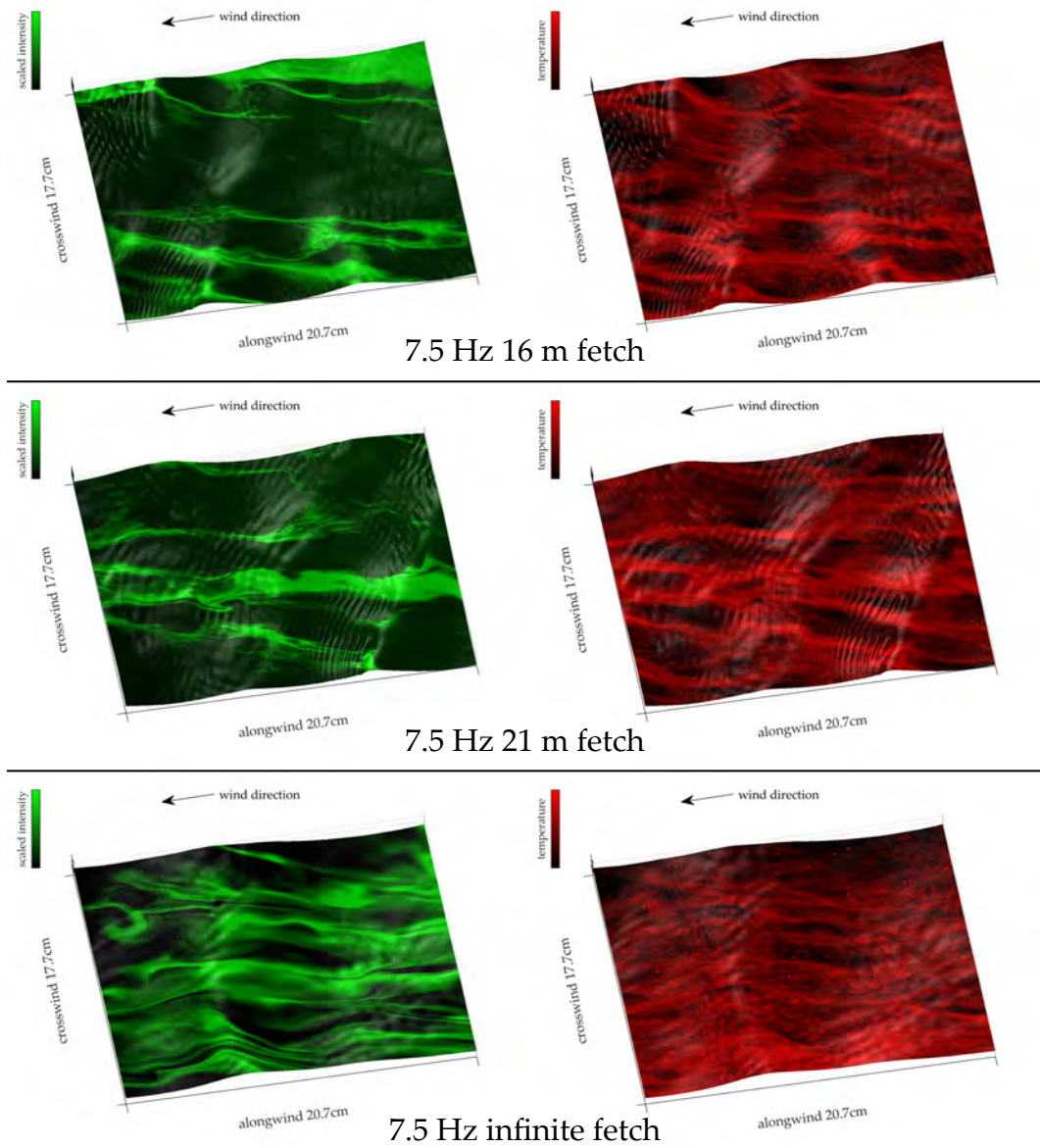


FIGURE B.9: Example images at same times of BLI (green) and AT (red) for $u_{10} = 3.7 \text{ m s}^{-1}$ - part 3.

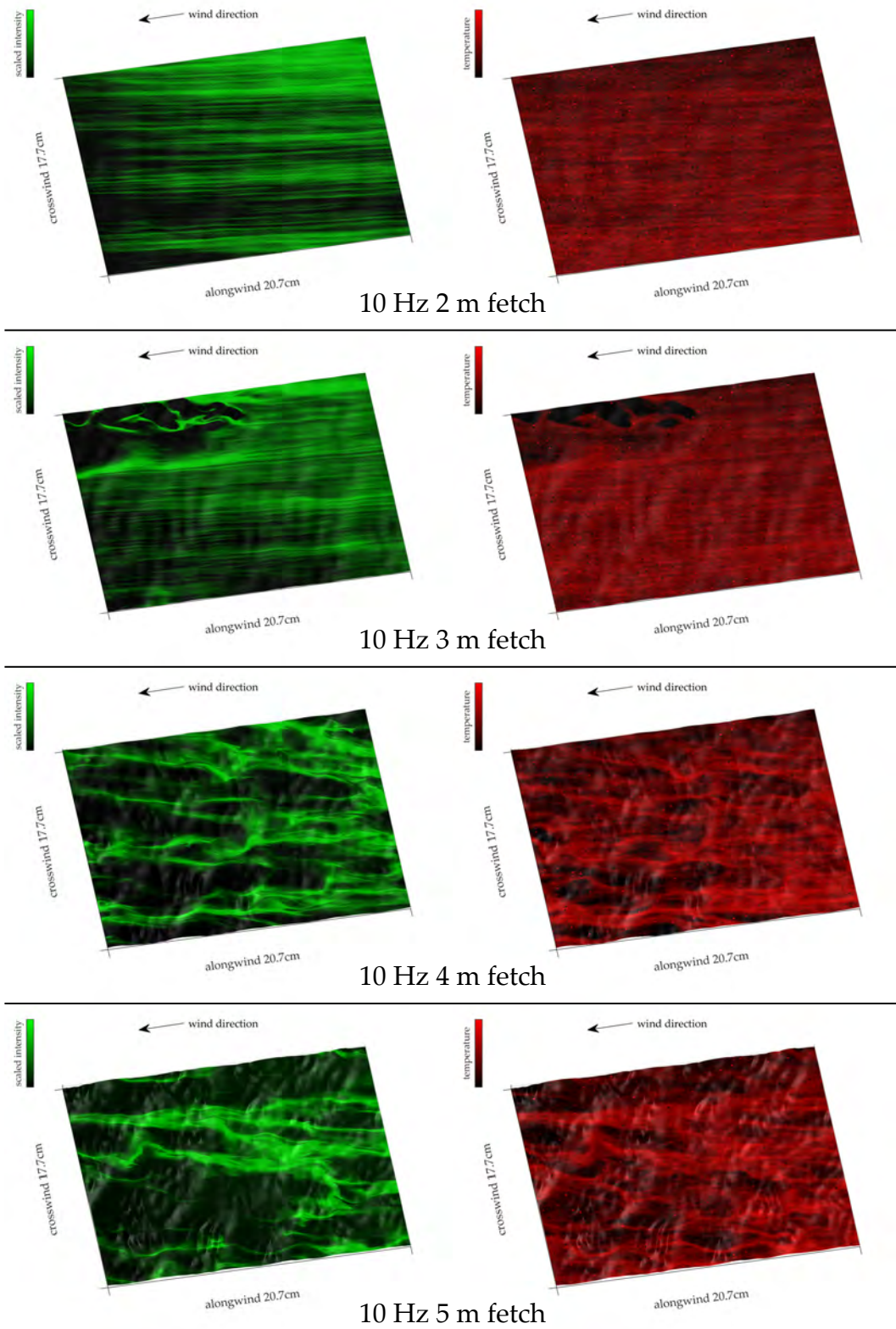


FIGURE B.10: Example images at same times of BLI (green) and AT (red) for $u_{10} = 4.8 \text{ m s}^{-1}$ - part 1.

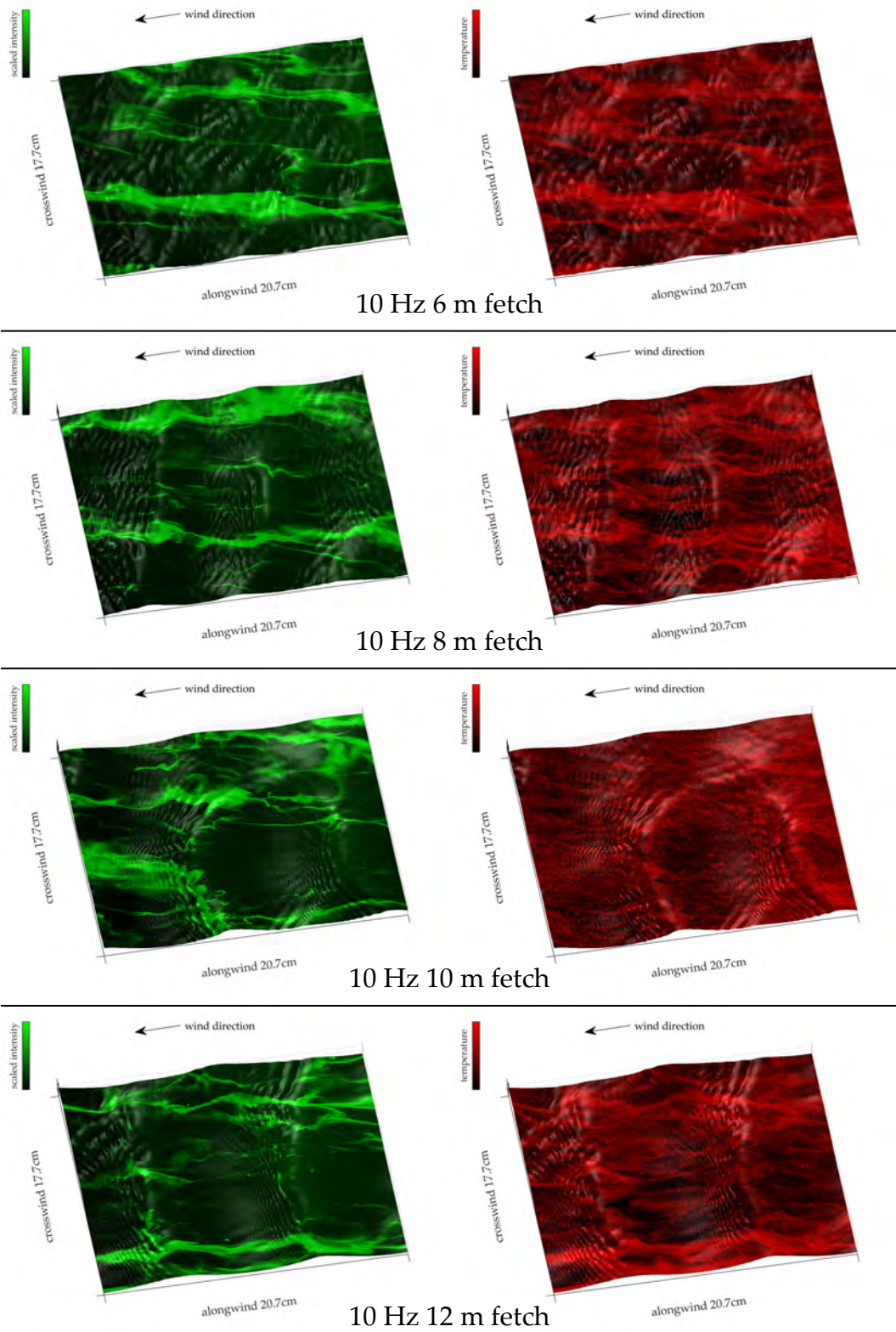


FIGURE B.11: Example images at same times of BLI (green) and AT (red) for $u_{10} = 4.8 \text{ m s}^{-1}$ - part 2.

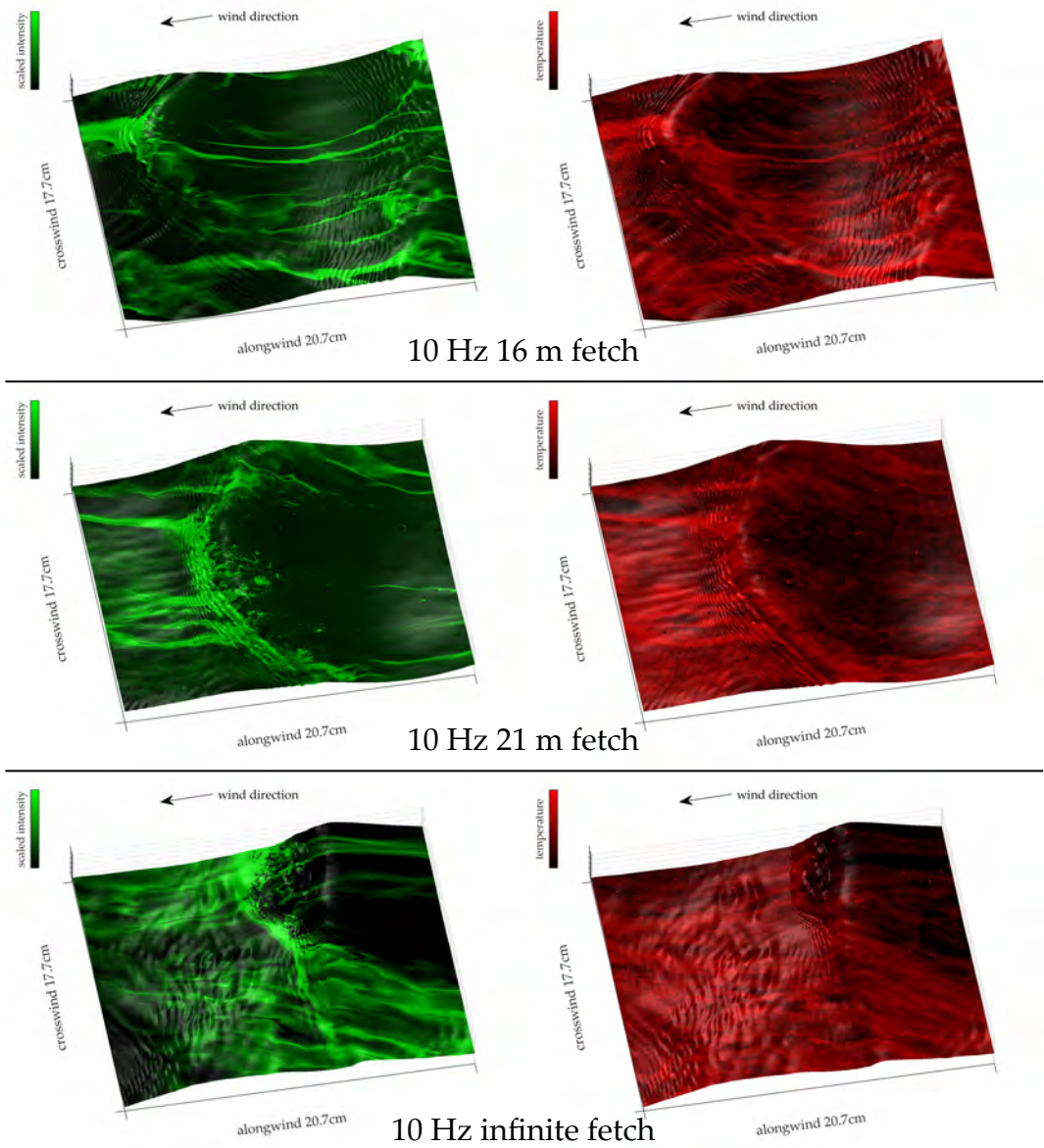


FIGURE B.12: Example images at same times of BLI (green) and AT (red) for $u_{10} = 4.8 \text{ m s}^{-1}$ - part 3.

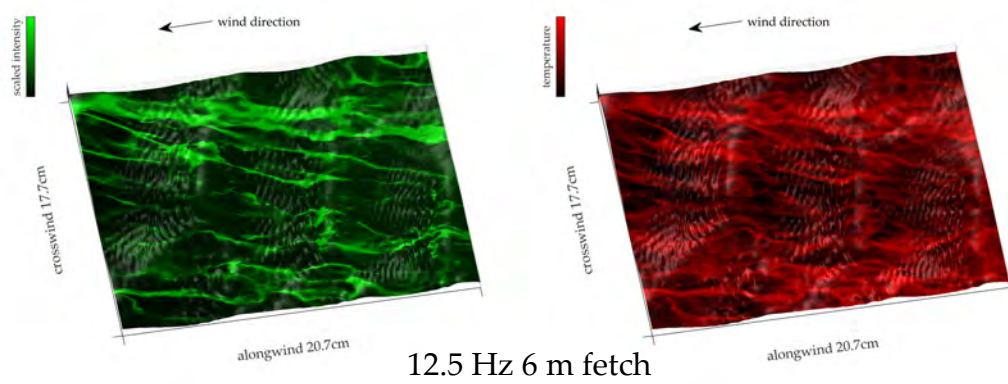
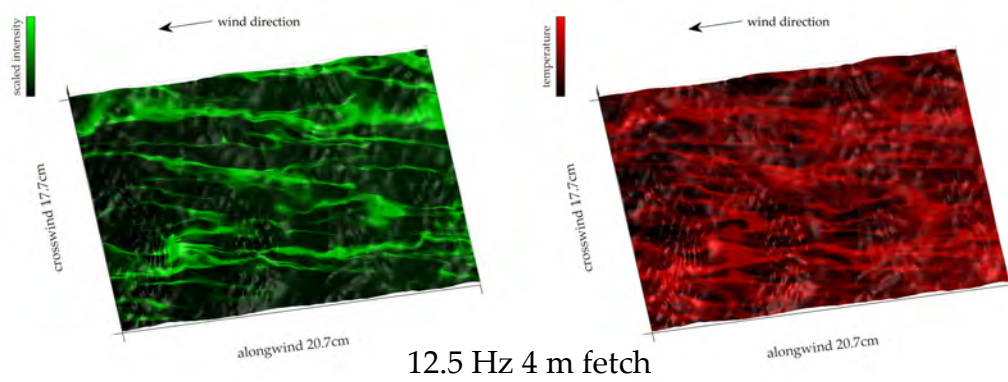
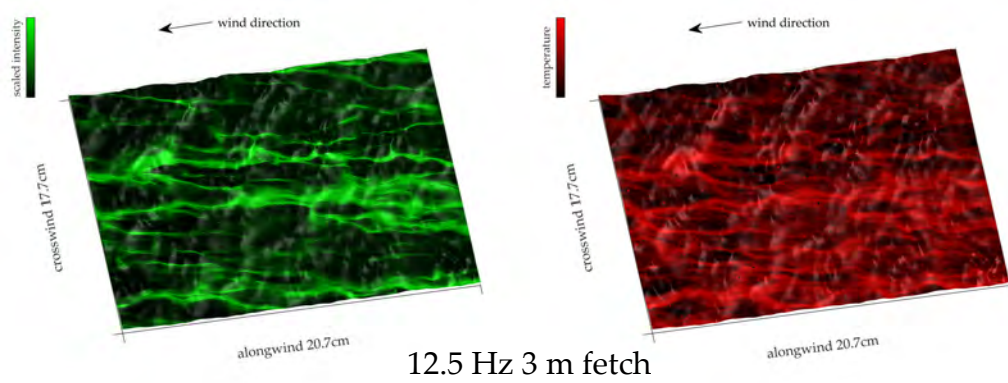
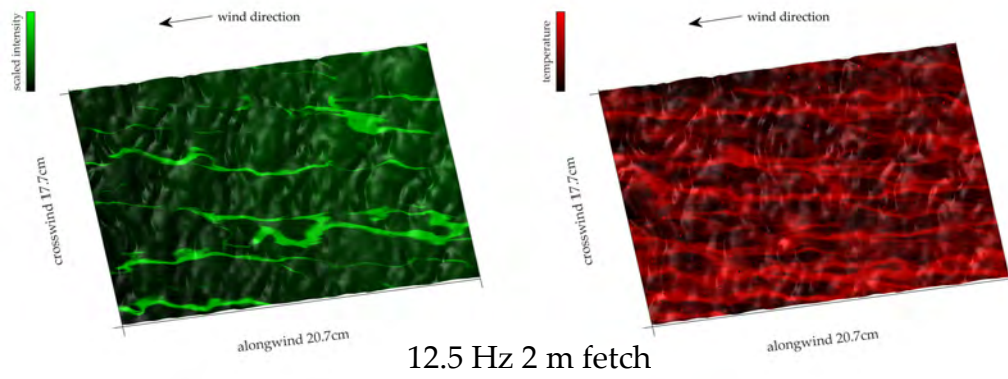


FIGURE B.13: Example images of BLI (green) and AT (red) for $u_{10} = 6.2 \text{ m s}^{-1}$ - part 1.

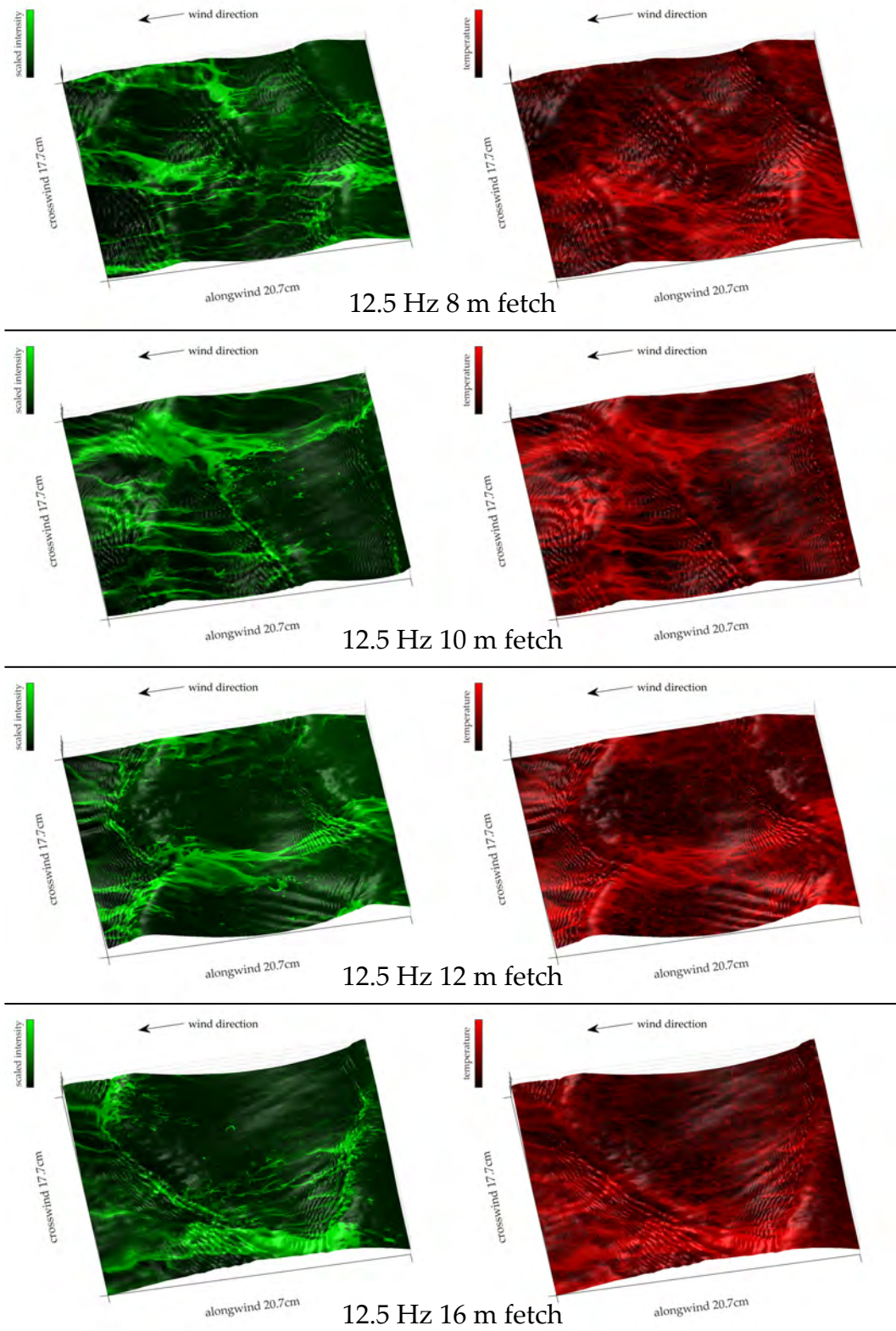


FIGURE B.14: Example images of BLI (green) and AT (red) for $u_{10} = 6.2 \text{ m s}^{-1}$ - part 2.

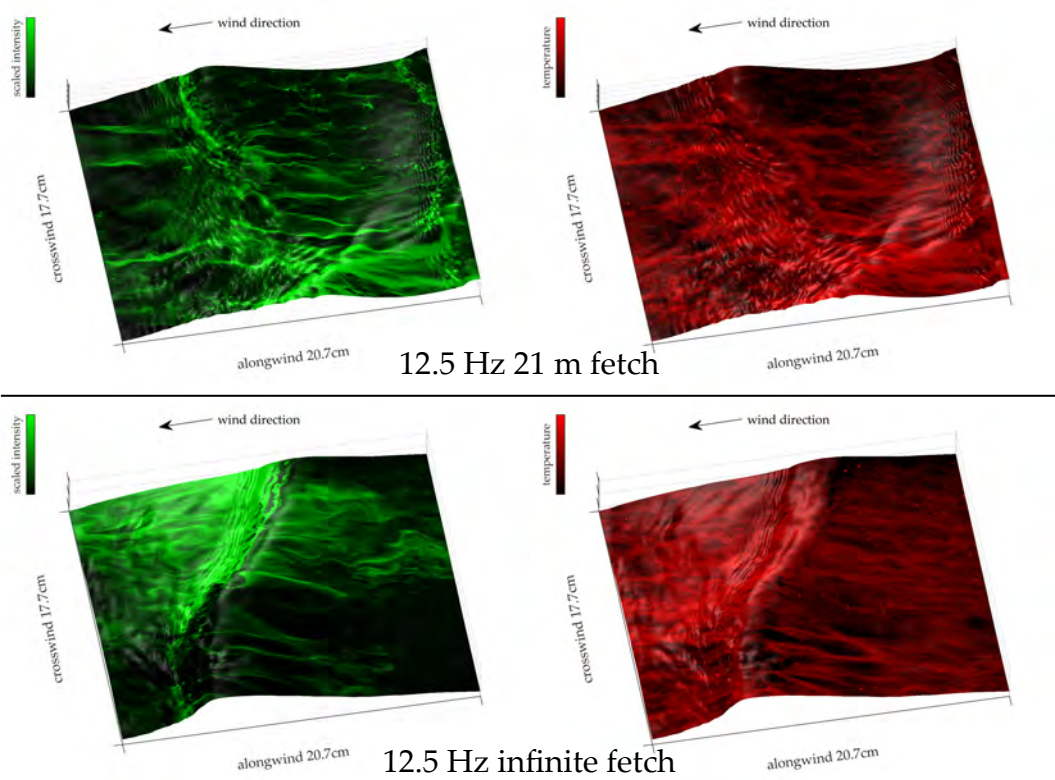


FIGURE B.15: Example images of BLI (green) and AT (red) for $u_{10} = 6.2 \text{ m s}^{-1}$ - part 3.

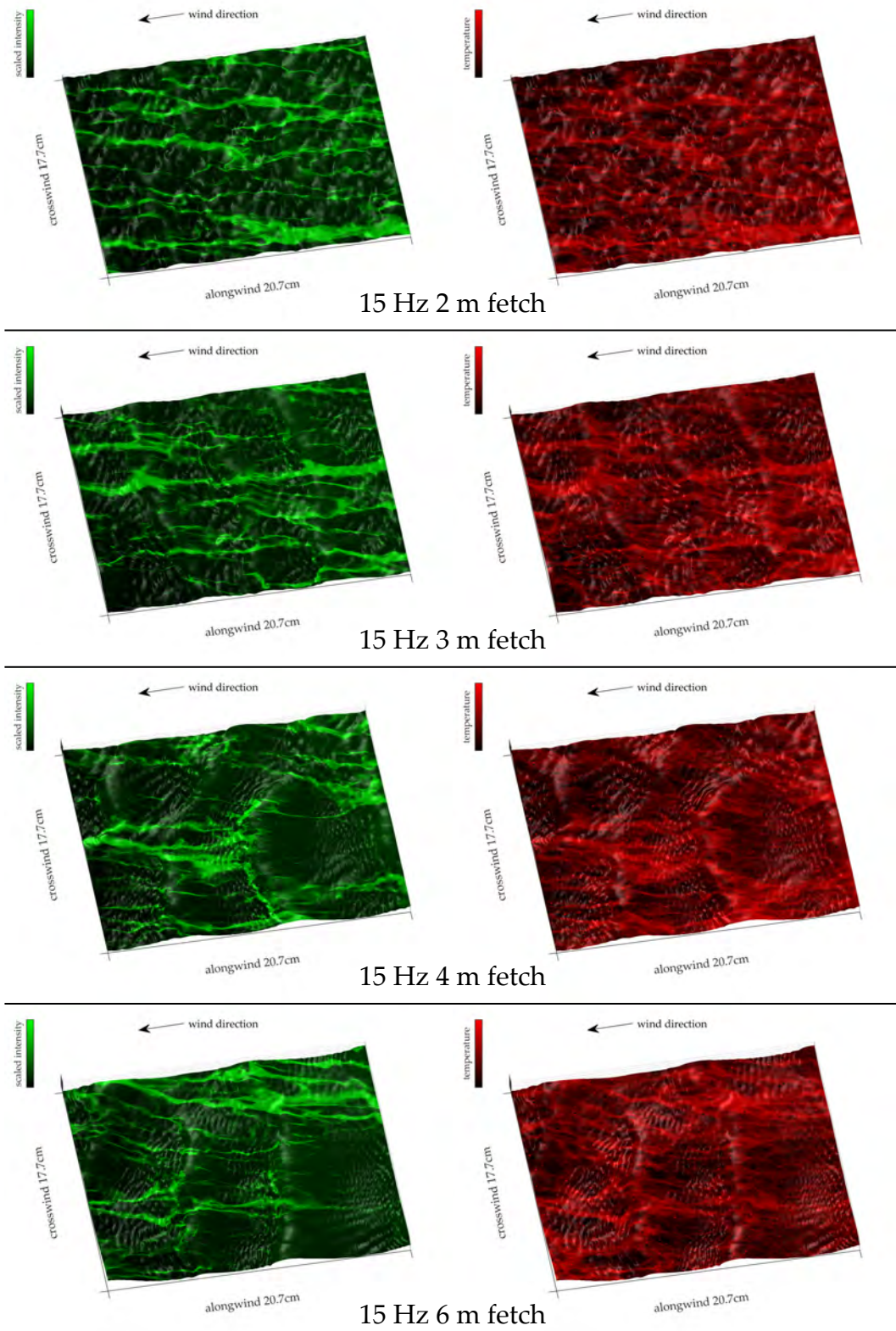


FIGURE B.16: Example images of BLI (green) and AT (red) for $u_{10} = 7.4 \text{ m s}^{-1}$ - part 1.

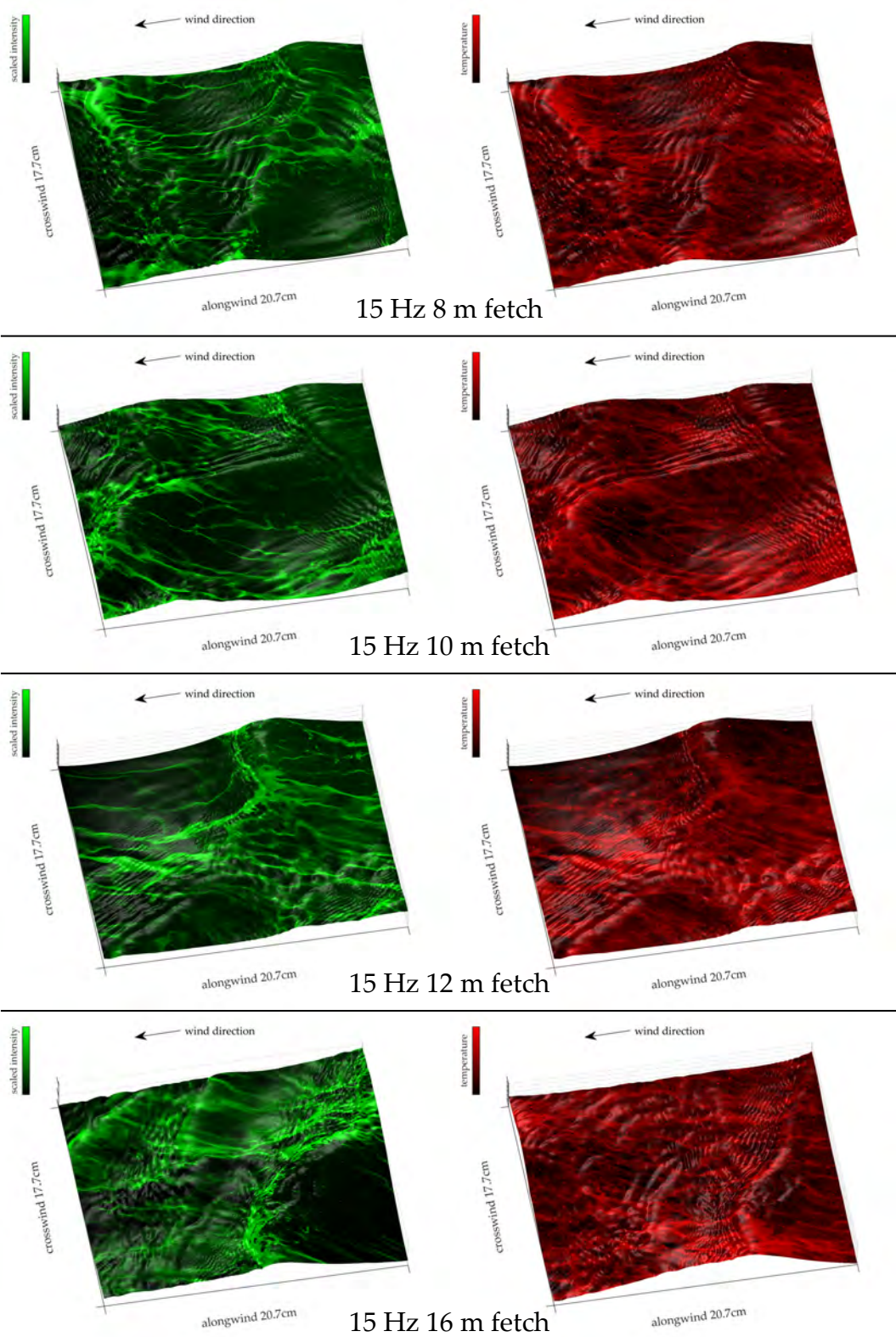


FIGURE B.17: Example images of BLI (green) and AT (red) for $u_{10} = 7.4 \text{ m s}^{-1}$ - part 2.

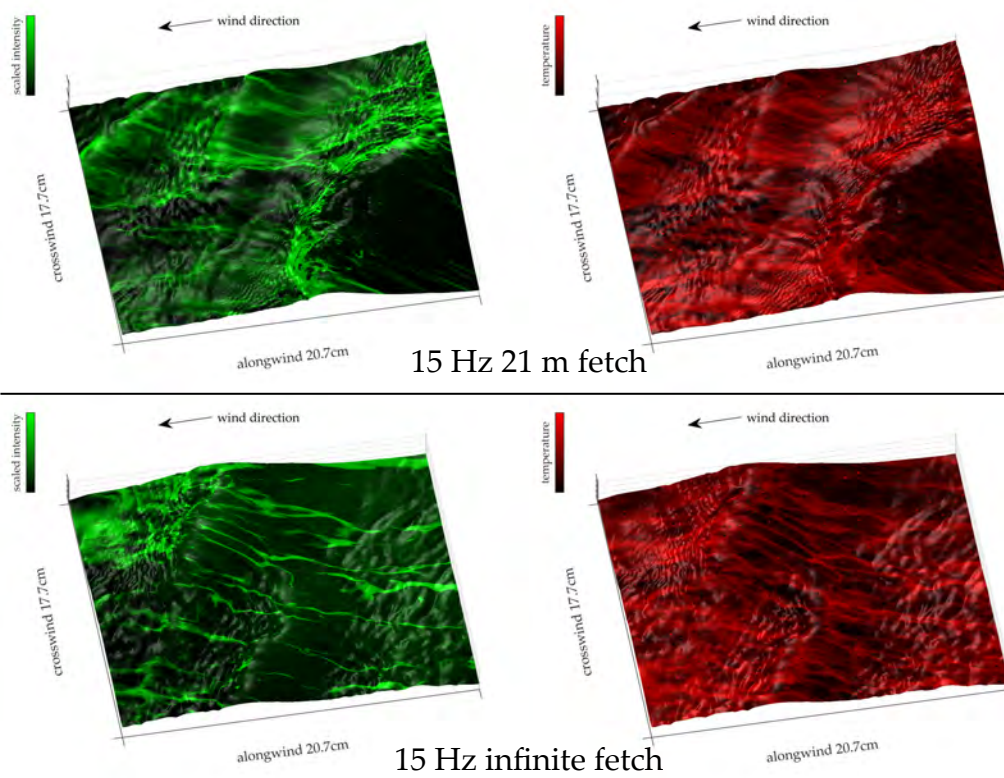


FIGURE B.18: Example images of BLI (green) and AT (red) for $u_{10} = 7.4 \text{ m s}^{-1}$ - part 3.

List of Figures

| | | |
|------|---|----|
| 1.1 | Streaks in the mass boundary layer snapshot | 2 |
| 1.2 | Microscale wave breaking | 3 |
| 2.1 | Air-sea interface | 7 |
| 2.2 | Gravity-capillary dispersion relation | 11 |
| 2.3 | Stokes waves | 14 |
| 2.4 | Crapper waves | 15 |
| 2.5 | MB sketch | 17 |
| 2.6 | Sketch of Langmuir circulation | 18 |
| 2.7 | Sketch of a horseshoe vortex | 19 |
| 2.8 | Fish-scales in thermal images | 20 |
| 3.1 | Aeolotron facility | 22 |
| 3.2 | Wave absorber in the Aeolotron facility | 22 |
| 3.3 | Measurement setup | 23 |
| 3.4 | ISG light refraction at water surface | 23 |
| 3.5 | Calibration scheme of ISG | 24 |
| 3.6 | Concentration profiles of the BLI principle | 25 |
| 3.7 | Image of the boundary layer fluorescence | 26 |
| 3.8 | Calibration scheme of the BLI | 26 |
| 3.9 | Refraction of the incident light | 27 |
| 3.10 | Thickness correction of the BLI | 28 |
| 3.11 | Further calibration steps of the BLI | 28 |
| 3.12 | AT heating sketch of the water surface | 29 |
| 3.13 | AT evaluation steps | 29 |
| 3.14 | Unmapped checkerboard patterns of ISG, BLI, and AT | 30 |
| 3.15 | Mapped checkerboard patterns of ISG, BLI, and AT | 31 |
| 3.16 | Finalized coordinate transformation of the visualization techniques | 32 |
| 4.1 | ISG slopes and surface elevation | 36 |
| 4.2 | Surface reconstruction with wave elevation | 37 |
| 4.3 | Gravity wave phase speed determination | 37 |
| 4.4 | Adapted gravity wave phase speed fit routine | 38 |
| 4.5 | Wave period determination | 38 |
| 4.6 | Empirical mode decomposition of the wave elevation | 39 |
| 4.7 | Capillary wavelength split up | 40 |

| | | |
|------|---|----|
| 4.8 | Capillary wavelength determination | 40 |
| 4.9 | Wave phase determination | 42 |
| 4.10 | MBS detection | 42 |
| 4.11 | Wave phase dependent MBS distribution | 43 |
| 4.12 | Curvature dependent thickness variation of the boundary layer | 44 |
| 5.1 | Regimes of the FE wind conditions against the fetch | 45 |
| 5.2 | Overview of the regime classification | 47 |
| 5.3 | Heat transfer velocities of the FE | 49 |
| 5.4 | Infinite fetch heat transfer velocities | 49 |
| 5.5 | Infinite fetch heat and gas transfer velocities | 50 |
| 5.6 | Schmidt number exponent for infinite fetch | 51 |
| 5.7 | Dimensionless scaling factor for infinite fetch | 51 |
| 5.8 | Wave height plotted against wavelength | 52 |
| 5.9 | Significant wave height parameterization | 53 |
| 5.10 | Fetch dependent wave period and heat transfer time constant | 54 |
| 5.11 | Wave phase velocity plotted against the dominant gravity wavelength | 55 |
| 5.12 | Wave age plotted against the fetch | 55 |
| 5.13 | Fetch dependent mean square slope | 56 |
| 5.14 | Parameterization of the local friction velocity for infinite fetch | 57 |
| 5.15 | Parameterization of the local friction velocity for finite fetch | 58 |
| 5.16 | Comparison of friction velocities to the duration limited case | 59 |
| 5.17 | Regime dependent dimensionless transfer velocity | 60 |
| 5.18 | Reynolds number plotted against the wavelength | 61 |
| 5.19 | Windsea Reynolds number | 62 |
| 5.20 | Roughness Reynolds number | 63 |
| 5.21 | Parasitic capillary wavelengths | 63 |
| 5.22 | Observed BLI intensity overshoot for low curvature radii. | 64 |
| 5.23 | MB accumulation visualization | 65 |
| 5.24 | Estimation of counteracting velocity components for an MBS event | 67 |
| 5.25 | Toe cascading | 68 |
| 5.26 | Percentage of breaking wave crests | 69 |
| 5.27 | Fetch dependent MB strength | 69 |
| 5.28 | Wave phase position of MBS plotted against the fetch | 70 |
| 5.29 | Wavelength dependent wave phase position of MBS | 71 |
| 5.30 | Wave phase position of MBS plotted against the MB strength | 71 |
| 5.31 | Strength of MB plotted against the wave steepness | 72 |
| 5.32 | Iribarren number plotted against the wave phase position of MB | 73 |
| 5.33 | Stokes waves | 73 |
| 5.34 | Heat transfer velocity for infinite fetch plotted against the MBS strength | 74 |
| 5.35 | Comparison of measured heat transfer velocity to MB surface renewal parameterization | 75 |

| | |
|--|-----|
| 5.36 MB events over time | 76 |
| 5.37 Boundary layer structures of streak regime A - example 1 | 78 |
| 5.38 Boundary layer structures of streak regime A - example 2 | 79 |
| 5.39 Boundary layer structures of streak regime A - example 3 | 80 |
| 5.40 Boundary layer structures of streak regime B - example 1 | 81 |
| 5.41 Boundary layer structures of streak regime B - example 2 | 82 |
| 5.42 Boundary layer structures of streak regime C - example 1 | 83 |
| 5.43 Boundary layer structures of streak regime C - example 2 | 84 |
| 5.44 Boundary layer structures of streak regime 1 | 86 |
| 5.45 Boundary layer structures of streak regime 2 | 87 |
| | |
| B.1 Wave elevation without additional lighting | 100 |
| B.2 Wave elevation with lighting as chosen for the visualization in this thesis | 100 |
| B.3 Wave elevation with too strong lighting | 101 |
| B.4 Visualization of the mass boundary layer | 101 |
| B.5 Scaled visualization of the mass boundary layer | 102 |
| B.6 Scaled visualization of the surface temperature | 103 |
| B.7 Examples of BLI (green) and AT (red) for $u_{10} = 3.7 \text{ m s}^{-1}$ - part 1 | 104 |
| B.8 Examples of BLI (green) and AT (red) for $u_{10} = 3.7 \text{ m s}^{-1}$ - part 2 | 105 |
| B.9 Examples of BLI (green) and AT (red) for $u_{10} = 3.7 \text{ m s}^{-1}$ - part 3 | 106 |
| B.10 Examples of BLI (green) and AT (red) for $u_{10} = 4.8 \text{ m s}^{-1}$ - part 1 | 107 |
| B.11 Examples of BLI (green) and AT (red) for $u_{10} = 4.8 \text{ m s}^{-1}$ - part 2 | 108 |
| B.12 Examples of BLI (green) and AT (red) for $u_{10} = 4.8 \text{ m s}^{-1}$ - part 3 | 109 |
| B.13 Examples of BLI (green) and AT (red) for $u_{10} = 6.2 \text{ m s}^{-1}$ - part 1 | 110 |
| B.14 Examples of BLI (green) and AT (red) for $u_{10} = 6.2 \text{ m s}^{-1}$ - part 2 | 111 |
| B.15 Examples of BLI (green) and AT (red) for $u_{10} = 6.2 \text{ m s}^{-1}$ - part 3 | 112 |
| B.16 Examples of BLI (green) and AT (red) for $u_{10} = 7.4 \text{ m s}^{-1}$ - part 1 | 113 |
| B.17 Examples of BLI (green) and AT (red) for $u_{10} = 7.4 \text{ m s}^{-1}$ - part 2 | 114 |
| B.18 Examples of BLI (green) and AT (red) for $u_{10} = 7.4 \text{ m s}^{-1}$ - part 3 | 115 |

List of Tables

| | | |
|-----|---|----|
| 2.1 | Occurrence of MB in other studies | 18 |
| 3.1 | Fetch conditions of the FE | 31 |
| 3.2 | Variable ammonia influx for infinite fetch | 33 |
| A.1 | Local heat transfer velocities, global gas transfer velocities, Schmidt number exponent, and dimensionless scaling factor for infinite fetch . | 93 |
| A.2 | Local heat transfer velocities for finite fetch | 94 |
| A.3 | Local wave parameters for finite fetch | 95 |
| A.4 | Local wave parameters for infinite fetch | 96 |
| A.5 | Local MB parameters for finite fetch | 97 |
| A.6 | Local MB parameters for infinite fetch | 98 |

Bibliography

- Badulin, S. I., A. V. Babanin, V. E. Zakharov, and D. Resio (2007). "Weakly turbulent laws of wind-wave growth". In: *Journal of Fluid Mechanics* 591. DOI: [10.1017/S0022112007008282](https://doi.org/10.1017/S0022112007008282).
- Banner, M. L. and W. L. Peirson (1998). "Tangential stress beneath wind-driven air-water interfaces". In: *Journal of Fluid Mechanics* 364, pp. 115–145. DOI: [10.1017/S0022112098001128](https://doi.org/10.1017/S0022112098001128).
- Banner, M. L. and O. M. Phillips (1974). "On the incipient breaking of small scale waves". In: *Journal of Fluid Mechanics* 65.4, pp. 647–656.
- Battjes, J. A. (1974). "Surf Similarity". In: *Coastal Engineering 1974*. American Society of Civil Engineers. DOI: [10.1061/9780872621138.029](https://doi.org/10.1061/9780872621138.029).
- Bender, M. L., S. Kinter, N. Cassar, and R. Wanninkhof (2011). "Evaluating gas transfer velocity parameterizations using upper ocean radon distributions". In: *Journal of Geophysical Research* 116.C2. DOI: [10.1029/2009jc005805](https://doi.org/10.1029/2009jc005805).
- Brandt, L. (2014). "The lift-up effect: The linear mechanism behind transition and turbulence in shear flows". In: *European Journal of Mechanics - B/Fluids* 47. Enok Palm Memorial Volume, pp. 80–96. ISSN: 0997-7546. DOI: <https://doi.org/10.1016/j.euromechflu.2014.03.005>.
- Chernyshenko, S. I. and M. F. Baig (2005). "The mechanism of streak formation in near-wall turbulence". In: *Journal of Fluid Mechanics* 544, 99–131. DOI: [10.1017/S0022112005006506](https://doi.org/10.1017/S0022112005006506).
- Danckwerts, P. V. (1951). "Significance of Liquid-Film Coefficients in Gas Absorption". In: *Industrial & Engineering Chemistry* 43.6, pp. 1460–1467. DOI: [10.1021/ie50498a055](https://doi.org/10.1021/ie50498a055).
- Deacon, E. L. (1977). "Gas transfer to and across an air-water interface". In: *Tellus* 29.4, pp. 363–374. DOI: [10.1111/j.2153-3490.1977.tb00746.x](https://doi.org/10.1111/j.2153-3490.1977.tb00746.x).
- Degreif, K. (2006). "Untersuchungen zum Gasaustausch - Entwicklung und Applikation eines zeitlich aufgelösten Massenbilanzverfahrens". In: DOI: [10.11588/heidok.00006120](https://doi.org/10.11588/heidok.00006120).
- Demtröder, W. (2008). *Experimentalphysik 1*. Springer Berlin Heidelberg. DOI: [10.1007/978-3-540-79295-6](https://doi.org/10.1007/978-3-540-79295-6).
- Deng, H., W. Zhang, E. Mortensen, T. Dietterich, and L. Shapiro (2007). "Principal Curvature-Based Region Detector for Object Recognition". In: *2007 IEEE Conference on Computer Vision and Pattern Recognition*. IEEE. DOI: [10.1109/cvpr.2007.382972](https://doi.org/10.1109/cvpr.2007.382972).

- Donelan, M., M. Skafel, H. Graber, P. Liu, D. Schwab, and S. Venkatesh (1992). "On the growth rate of wind-generated waves". In: *Atmosphere-Ocean* 30.3, pp. 457–478. DOI: [10.1080/07055900.1992.9649449](https://doi.org/10.1080/07055900.1992.9649449).
- Duncan, J. H., H. Qiao, V. Philomin, and A. Wenz (1999). "Gentle spilling breakers: crest profile evolution". In: *Journal of Fluid Mechanics* 379, 191–222. DOI: [10.1017/S0022112098003152](https://doi.org/10.1017/S0022112098003152).
- Fedorov, A. V., W. K. Melville, and A. Rozenberg (1998). "An experimental and numerical study of parasitic capillary waves". In: *Physics of Fluids* 10.6, pp. 1315–1323. DOI: [10.1063/1.869657](https://doi.org/10.1063/1.869657).
- Fontaine, E. (2013). "A Theoretical Explanation of the Fetch- and Duration-Limited Laws". In: *Journal of Physical Oceanography* 43.2, pp. 233–247. DOI: [10.1175/jpo-d-11-0190.1](https://doi.org/10.1175/jpo-d-11-0190.1).
- Frankot, R.T. and R. Chellappa (1988). "A method for enforcing integrability in shape from shading algorithms". In: *IEEE Transactions on Pattern Analysis and Machine Intelligence* 10.4, pp. 439–451. DOI: [10.1109/34.3909](https://doi.org/10.1109/34.3909).
- Gao, Z., Q. Wang, and M. Zhou (2009). "Wave-dependence of friction velocity, roughness length, and drag coefficient over coastal and open water surfaces by using three databases". In: *Advances in Atmospheric Sciences* 26.5, pp. 887–894. DOI: [10.1007/s00376-009-8130-7](https://doi.org/10.1007/s00376-009-8130-7).
- Handler, R. A., G. B. Smith, and R. I. Leighton (2001). "The thermal structure of an air–water interface at low wind speeds". In: *Tellus A* 53.2, pp. 233–244. DOI: [10.1034/j.1600-0870.2001.00158.x](https://doi.org/10.1034/j.1600-0870.2001.00158.x). eprint: <https://onlinelibrary.wiley.com/doi/pdf/10.1034/j.1600-0870.2001.00158.x>.
- Hiby, J. W., D. Braun, and K. H. Eickel (1967). "Eine Fluoreszenzmethode zur Untersuchung des Stoffübergangs bei der Gasabsorption im Rieselfilm". In: *Chemie Ingenieur Technik - CIT* 39.5-6, pp. 297–301. DOI: [10.1002/cite.330390517](https://doi.org/10.1002/cite.330390517).
- Higbie, R. (1935). "The rate of absorption of a pure gas into a still liquid during short periods of exposure". In: *Trans. Am. Inst. Chem. Eng.* 31, pp. 365–389.
- Hoffman, R. N., J. V. Ardizzone, S. M. Leidner, D. K. Smith, and R. Atlas (2013). "Error Estimates for Ocean Surface Winds: Applying Desroziers Diagnostics to the Cross-Calibrated, Multiplatform Analysis of Wind Speed". In: *Journal of Atmospheric and Oceanic Technology* 30.11, pp. 2596–2603. DOI: [10.1175/jtech-d-13-00018.1](https://doi.org/10.1175/jtech-d-13-00018.1).
- Hughes, S. A. (2004). "Wave momentum flux parameter: a descriptor for nearshore waves". In: *Coastal Engineering* 51.11-12, pp. 1067–1084. DOI: [10.1016/j.coastaleng.2004.07.025](https://doi.org/10.1016/j.coastaleng.2004.07.025).
- Hwang, P. A. (2006). "Duration- and fetch-limited growth functions of wind-generated waves parameterized with three different scaling wind velocities". In: *Journal of Geophysical Research* 111.C2. DOI: [10.1029/2005jc003180](https://doi.org/10.1029/2005jc003180).
- Iafrazi, A. and E. F. Campana (2005). "Free-surface fluctuations behind microbreakers: space–time behaviour and subsurface flow field". In: *Journal of Fluid Mechanics* 529, pp. 311–347. DOI: [10.1017/s0022112005003472](https://doi.org/10.1017/s0022112005003472).

- Jessup, A. T., C. J. Zappa, and H. Yeh (1997). "Defining and quantifying microscale wave breaking with infrared imagery". In: *Journal of Geophysical Research: Oceans* 102.C10, pp. 23145–23153.
- Jung, S. Y. and T. A. Zaki (2015). "The effect of a low-viscosity near-wall film on bypass transition in boundary layers". In: *Journal of Fluid Mechanics* 772, pp. 330–360. DOI: [10.1017/jfm.2015.214](https://doi.org/10.1017/jfm.2015.214).
- Jähne, B. (1980). "Zur Parametrisierung des Gasaustauschs mit Hilfe von Laborexperimenten". In: DOI: [10.11588/heidok.00016796](https://doi.org/10.11588/heidok.00016796).
- (1985). "Transfer Processes Across The Free Water Surface". In: DOI: [10.5281/zenodo.12202](https://doi.org/10.5281/zenodo.12202).
- (2013). "Compression by noise equalization". In: *Tech. rep., Heidelberg Collaboratory for Image Processing (HCI)*. DOI: <http://dx.doi.org/10.5072/zenodo.12761>.
- Jähne, B. and K. S. Riemer (1990). "Two-dimensional wave number spectra of small-scale water surface waves". In: *Journal of Geophysical Research* 95.C7, p. 11531. DOI: [10.1029/jc095ic07p11531](https://doi.org/10.1029/jc095ic07p11531).
- Jähne, B., K. O. Münnich, R. Böisinger, A. Dutzi, W. Huber, and P. Libner (1987). "On the parameters influencing air-water gas exchange". In: *Journal of Geophysical Research* 92.C2, p. 1937. DOI: [10.1029/jc092ic02p01937](https://doi.org/10.1029/jc092ic02p01937).
- Jähne, B., P. Libner, R. Fischer, T. Billen, and E. J. Plate (1989). "Investigating the transfer processes across the free aqueous viscous boundary layer by the controlled flux method". In: *Tellus B* 41B.2, pp. 177–195. DOI: [10.1111/j.1600-0889.1989.tb00135.x](https://doi.org/10.1111/j.1600-0889.1989.tb00135.x). eprint: <https://onlinelibrary.wiley.com/doi/pdf/10.1111/j.1600-0889.1989.tb00135.x>.
- Kiefhaber, D., S. Reith, R. Rocholz, and B. Jähne (2014). "High-speed imaging of short wind waves by shape from refraction". In: *Journal of the European Optical Society - Rapid publications* 9.0. ISSN: 1990-2573. DOI: [10.2971/jeos.2014.14015](https://doi.org/10.2971/jeos.2014.14015).
- Kinsman, B. (1965). *Wind waves: their generation and propagation on the ocean surface*. Courier Corporation.
- Komori, S., R. Nagaosa, Y. Murakami, S. Chiba, K. Ishii, and K. Kuwahara (1993). "Direct numerical simulation of three-dimensional open-channel flow with zero-shear gas-liquid interface". In: *Physics of Fluids A: Fluid Dynamics* 5.1, pp. 115–125.
- Krall, K. E. (2013). "Laboratory Investigations of Air-Sea Gas Transfer under a Wide Range of Water Surface Conditions". In: DOI: [10.11588/heidok.00014392](https://doi.org/10.11588/heidok.00014392).
- Kräuter, C. (2015). "Visualization of air-water gas exchange". PhD thesis. DOI: [10.11588/heidok.00018209](https://doi.org/10.11588/heidok.00018209).
- Kräuter, C., D. Trofimova, D. Kiefhaber, N. Krah, and B. Jähne (2014). "High resolution 2-D fluorescence imaging of the mass boundary layer thickness at free water surfaces". In: *Journal of the European Optical Society: Rapid Publications* 9. DOI: [10.2971/jeos.2014.14016](https://doi.org/10.2971/jeos.2014.14016).
- Kunz, J. (2017). "Active Thermography as a Tool for the Estimation of Air-Water Transfer Velocities". In: DOI: [10.11588/heidok.00022903](https://doi.org/10.11588/heidok.00022903).

- Kunz, J. and B. Jähne (2018). "Investigating Small-Scale Air–Sea Exchange Processes via Thermography". In: *Frontiers in Mechanical Engineering* 4, p. 4. DOI: [10.3389/fmech.2018.00004](https://doi.org/10.3389/fmech.2018.00004).
- Libner, P. (1987). "Die Konstantfluss-Methode: ein neuartiges, schnelles und lokales Messverfahren zur Untersuchung von Austauschvorgängen an einer Luft-Wasser-Phasengrenze". In: *Dissertation, University of Heidelberg*. URL: <http://d-nb.info/881465941>.
- Longuet-Higgins, M. S. (1992). "Capillary rollers and bores". In: *Journal of Fluid Mechanics* 240, pp. 659–679.
- (1994). "Shear Instability in Spilling Breakers". In: *Proceedings of the Royal Society A: Mathematical, Physical and Engineering Sciences* 446.1927, pp. 399–409. DOI: [10.1098/rspa.1994.0111](https://doi.org/10.1098/rspa.1994.0111).
- (1995). "Parasitic capillary waves: a direct calculation". In: *Journal of Fluid Mechanics* 301.-1, p. 79. DOI: [10.1017/s0022112095003818](https://doi.org/10.1017/s0022112095003818).
- Mandic, D. P., N. ur Rehman, Z. Wu, and N. E. Huang (2013). "Empirical Mode Decomposition-Based Time-Frequency Analysis of Multivariate Signals: The Power of Adaptive Data Analysis". In: *IEEE Signal Processing Magazine* 30.6, pp. 74–86. DOI: [10.1109/msp.2013.2267931](https://doi.org/10.1109/msp.2013.2267931).
- Marple, L. (1999). "Computing the discrete-time "analytic" signal via FFT". In: *IEEE Transactions on Signal Processing* 47.9, pp. 2600–2603. DOI: [10.1109/78.782222](https://doi.org/10.1109/78.782222).
- Massel, S. R (2013). *Ocean Surface Waves*. WORLD SCIENTIFIC. DOI: [10.1142/8682](https://doi.org/10.1142/8682).
- Murashige, S. and W. Choi (2017). "A numerical study on parasitic capillary waves using unsteady conformal mapping". In: *Journal of Computational Physics* 328, pp. 234–257. DOI: [10.1016/j.jcp.2016.10.015](https://doi.org/10.1016/j.jcp.2016.10.015).
- Nielsen, R. (2004). "Gasaustausch - Entwicklung und Ergebnis eines schnellen Massenbilanzverfahrens zur Messung der Austauschparameter". In: DOI: [10.11588/heidok.00005032](https://doi.org/10.11588/heidok.00005032).
- Nikuradse, J. (1933). "Strömungsgesetze in rauhen Röhren". In:
- Peirson, W. L. and M. L. Banner (2003). "Aqueous surface layer flows induced by microscale breaking wind waves". In: *Journal of Fluid Mechanics* 479, 1–38. DOI: [10.1017/S0022112002003336](https://doi.org/10.1017/S0022112002003336).
- Qiao, H. and J. H. Duncan (2001). "Gentle spilling breakers: crest flow-field evolution". In: *Journal of Fluid Mechanics* 439. DOI: [10.1017/s0022112001004207](https://doi.org/10.1017/s0022112001004207).
- Roedel, W. and T. Wagner (2017). *Physik unserer Umwelt: Die Atmosphäre*. Springer Berlin Heidelberg. DOI: [10.1007/978-3-662-54258-3](https://doi.org/10.1007/978-3-662-54258-3).
- Roth, N. (2018). "Visualization of Near-Surface Flow Patterns for Air-Water Gas Transfer". In: DOI: [10.11588/heidok.00024623](https://doi.org/10.11588/heidok.00024623).
- Sabine C. L., Feely R. A. Gruber N. Key R. M. Lee K. Bullister J. L. Wanninkhof R. Wong C. S. Wallace D. W. R. Tilbrook B. Millero F. J. Peng T. Kozyr A. Ono T. Rios A. F. (2004). "The Oceanic Sink for Anthropogenic CO₂". In: *Science* 305.5682, pp. 367–371. DOI: [10.1126/science.1097403](https://doi.org/10.1126/science.1097403).

- Scherr, T. (2017). "Gradient-Based Surface Reconstruction and the Application to Wind Waves". In: DOI: [10.11588/heidok.00023653](https://doi.org/10.11588/heidok.00023653).
- Schnieders, J, C. S. Garbe, W. L. Peirson, G. B. Smith, and Christopher J. Zappa (2013). "Analyzing the footprints of near-surface aqueous turbulence: An image processing-based approach". In: *Journal of Geophysical Research: Oceans* 118.3, pp. 1272–1286. DOI: [10.1002/jgrc.20102](https://doi.org/10.1002/jgrc.20102).
- Schwenk, C. (2019). "Messung der Schubspannungsgeschwindigkeit am Heidelberger Aeolotron unter instationären Bedingungen". In: *Bachelor Thesis*.
- Scott, N. V., R. A. Handler, and G. B. Smith (2008). "Wavelet analysis of the surface temperature field at an air–water interface subject to moderate wind stress". In: *International Journal of Heat and Fluid Flow* 29.4, pp. 1103–1112. DOI: [10.1016/j.ijheatfluidflow.2007.11.002](https://doi.org/10.1016/j.ijheatfluidflow.2007.11.002).
- Shuang, L. and S. Jinbao (2012). "The spacing of Langmuir circulation under modest wind". In: *Chinese Journal of Oceanology and Limnology* 30.4, pp. 690–696. DOI: [10.1007/s00343-012-1201-0](https://doi.org/10.1007/s00343-012-1201-0).
- Siddiqui, M. H. K. and M. R. Loewen (2007). "Characteristics of the wind drift layer and microscale breaking waves". In: *Journal of Fluid Mechanics* 573, 417–456. DOI: [10.1017/S0022112006003892](https://doi.org/10.1017/S0022112006003892).
- Siddiqui, M. H. K., M. R. Loewen, C. Richardson, W. E. Asher, and A. T. Jessup (2001). "Simultaneous particle image velocimetry and infrared imagery of microscale breaking waves". In: *Physics of Fluids* 13.7, pp. 1891–1903. DOI: [10.1063/1.1375144](https://doi.org/10.1063/1.1375144).
- Siddiqui, M. H. K., M. R. Loewen, W. E. Asher, and A. T. Jessup (2004). "Coherent structures beneath wind waves and their influence on air-water gas transfer". In: *Journal of Geophysical Research: Oceans* 109.C3. DOI: [10.1029/2002jc001559](https://doi.org/10.1029/2002jc001559).
- Steele, J. H., S. A. Thorpe, and K. K. Turekian (2009). "Elements of physical oceanography: a derivative of the encyclopedia of ocean sciences". In: *Academic Press*.
- Sunamura, T. and S. Okazaki (1996). "Breaker Types and Wave Reflection Coefficient: Laboratory Relationships". In: *Journal of Coastal Research* 12.1, pp. 240–245. ISSN: 07490208, 15515036. URL: <http://www.jstor.org/stable/4298478>.
- Sverdrup, H. U. and W. H. Munk (1947). "Wind, sea and swell. Theory of relations for forecasting. Pub". In: *Hydrog. Office, Wash* 601.
- Thorpe, S.A. (2004). "Langmuir Circulation". In: *Annual Review of Fluid Mechanics* 36.1, pp. 55–79. DOI: [10.1146/annurev.fluid.36.052203.071431](https://doi.org/10.1146/annurev.fluid.36.052203.071431).
- Toba, Y. (1997). "The 3/2-power law for ocean wind waves and its applications". In: *Advances in coastal and ocean engineering*.
- Toffoli, A, A Babanin, M Onorato, and T Waseda (2010). "Maximum steepness of oceanic waves: Field and laboratory experiments". In: *Geophysical Research Letters* 37.5. DOI: [10.1029/2009GL041771](https://doi.org/10.1029/2009GL041771).
- Trofimova, D. (2015). "Towards four dimensional visualization of air-water gas exchange". In: DOI: [10.11588/heidok.00019066](https://doi.org/10.11588/heidok.00019066).

- Tsai, W. (1998). "A numerical study of the evolution and structure of a turbulent shear layer under a free surface". In: *Journal of Fluid Mechanics* 354, pp. 239–276. DOI: [10.1017/s0022112097007623](https://doi.org/10.1017/s0022112097007623).
- Tsai, W. and L. Hung (2007). "Three-dimensional modeling of small-scale processes in the upper boundary layer bounded by a dynamic ocean surface". In: *Journal of Geophysical Research* 112.C2. DOI: [10.1029/2006jc003686](https://doi.org/10.1029/2006jc003686).
- Tsai, W., S. Chen, and C. Moeng (2005). "A numerical study on the evolution and structure of a stress-driven free-surface turbulent shear flow". In: *Journal of Fluid Mechanics* 545.-1, p. 163. DOI: [10.1017/s0022112005007044](https://doi.org/10.1017/s0022112005007044).
- Tsai, W., S. Chen, G. Lu, and C. S. Garbe (2013). "Characteristics of interfacial signatures on a wind-driven gravity-capillary wave". In: *Journal of Geophysical Research: Oceans* 118.4, pp. 1715–1735. DOI: [10.1002/jgrc.20145](https://doi.org/10.1002/jgrc.20145).
- Veron, F. and W. K. Melville (2001). "Experiments on the stability and transition of wind-driven water surfaces". In: *Journal of Fluid Mechanics* 446, 25–65.
- Wanninkhof, R. and J. Triñanes (2017). "The impact of changing wind speeds on gas transfer and its effect on global air-sea CO₂ fluxes". In: *Global Biogeochemical Cycles* 31.6, pp. 961–974. DOI: [10.1002/2016gb005592](https://doi.org/10.1002/2016gb005592).
- Whitman, W. G. (1962). "The two film theory of gas absorption". In: *International Journal of Heat and Mass Transfer* 5.5, pp. 429–433. DOI: [10.1016/0017-9310\(62\)90032-7](https://doi.org/10.1016/0017-9310(62)90032-7).
- Xiong, Y., A. Chakrabarti, R. Basri, S. J. Gortler, D. W. Jacobs, and T. Zickler (2015). "From Shading to Local Shape". In: *IEEE Transactions on Pattern Analysis and Machine Intelligence* 37.1, pp. 67–79. DOI: [10.1109/tpami.2014.2343211](https://doi.org/10.1109/tpami.2014.2343211).
- Zappa, C. J., W. E. Asher, and A. T. Jessup (2001). "Microscale wave breaking and air-water gas transfer". In: *Journal of Geophysical Research: Oceans* 106.C5, pp. 9385–9391. DOI: [10.1029/2000JC000262](https://doi.org/10.1029/2000JC000262).
- Zappa, C. J., W. E. Asher, A. T. Jessup, J. Klinke, and S. R. Long (2004). "Microbreaking and the enhancement of air-water transfer velocity". In: *Journal of Geophysical Research: Oceans* 109.C8, n/a–n/a. DOI: [10.1029/2003jc001897](https://doi.org/10.1029/2003jc001897).
- Zhang, X. (1995). "Capillary-gravity and capillary waves generated in a wind wave tank: observations and theories". In: *Journal of Fluid Mechanics* 289.-1, p. 51. DOI: [10.1017/s0022112095001236](https://doi.org/10.1017/s0022112095001236).
- Zhang, X. and C. S. Cox (1994). "Measuring the two-dimensional structure of a wavy water surface optically: A surface gradient detector". In: *Experiments in Fluids* 17.4, pp. 225–237. DOI: [10.1007/bf00203041](https://doi.org/10.1007/bf00203041).

Acknowledgements

First of all, I want to thank my thesis advisor **Prof. Dr. Bernd Jähne** for the opportunity to work on this interesting and unique research topic. It was a great pleasure to investigate the air-sea boundary layer utilizing the amazing measurement techniques available in this research group. Besides that, I am also very grateful for all the conferences and BV forums that I could attend throughout my PhD.

I also want to thank **Prof. Dr. Norbert Frank** for reviewing this thesis.

A special thanks goes to my family, which supported me my whole life and is always there for me when I need them. This includes my parents **Axel and Magdalena Klein**, my brother **Michael Klein**, his partner **Dilber Elmers**, my niece **Sibel Klein**, and my uncle **Walter Dörrenbächer**. I always enjoyed the small breaks during my thesis devoted to family events and I am glad that I can always count on them. My thanks also includes my late uncle **Klaus Dörrenbächer**, with his positive mood and cheeriness he will be dearly missed.

I am very grateful to my significant other **Zhongyi Feng** for our joint journey over the last ten years which we will continue in the future. While during Bachelor, Master, and PhD our scientific paths were always split between Environmental Physics and Atomic Physics, I hope that we will soon explore the combination of these two great research fields together.

Further, I want to thank **Dr. Kerstin Krall**, **Dr. Günther Balschbach**, **Sonja Friman** and **Dr. Zhongyi Feng** for their help in proofreading this thesis. Ten eyes see more than two.

A big thanks goes to **Dr. Daniel Kiefhaber**, **Dr. Christine Kräuter**, **Dr. Jakob Kunz**, **Dr. Kerstin Krall** and **Dr. Maximilian Bopp** that contributed a big part in the development of the measurement techniques utilized in this thesis. Without their work, the fetch experiment would not have been possible in this way. This includes, of course, all the previous work and colleagues of the research group on which their developments are based.

Tim Scherr investigated and compared a multitude of surface reconstruction algorithms. I therefore want to thank him that he determined the most effective surface reconstruction algorithm for the ISG data.

For the nice conversations about structures in the boundary layer, I want to thank **Nicolas Roth**. His alternative approach towards the visualization of the boundary layer led to interesting comparisons of our observations.

Another thanks goes to **Prof. Dr. Filip Sadlo**, who was my second supervisor associated with the HGS Math Comp.

I also want to thank the family of Zhongyi Feng **Prof. Dr. Yuanhua Feng**, **Katharina Feng**, and his late mother **Suju Ge** for their warm welcome into their family and for the nice family events.

Over the course of the last years many Bachelor and Master students were part of the research group. Hereby, I want to thank everyone I may have accidentally forgotten.